12-2006

Measurement of the $^{32}S(p,d)^{31}S$ Reaction and Its Astrophysical Implications

Zhanwen Ma
University of Tennessee - Knoxville

To the Graduate Council:

I am submitting herewith a dissertation written by Zhanwen Ma entitled "Measurement of the $^{32}S(p,d)^{31}S$ Reaction and Its Astrophysical Implications." I have examined the final electronic copy of this dissertation for form and content and recommend that it be accepted in partial fulfillment of the requirements for the degree of Doctor of Philosophy, with a major in Physics.

Mike W. Gudiry, Major Professor

We have read this dissertation and recommend its acceptance:

Michael Smith, Yuri Kamychkov, Carol Bingham, Lawrence Townsend

Accepted for the Council:
Carolyn R. Hodges

Vice Provost and Dean of the Graduate School

(Original signatures are on file with official student records.)

To the Graduate Council:

I am submitting herewith a dissertation written by Zhanwen Ma entitled "Measurement of the ^{32}S(p,d)^{31}S Reaction and Its Astrophysical Implications." I have examined the final electronic copy of this dissertation for form and content and recommend that it be accepted in partial fulfillment of the requirements for the degree of Doctor of Philosophy, with a major in Physics.

Mike W. Guidry
Major Professor

We have read this dissertation
and recommend its acceptance:

Michael Smith

Yuri Kamychkov

Carrol Bingham

Lawrence Townsend

Accepted for the Council:

Linda Painter
Interim Dean of Graduate Studies

(Original signatures are on file with official student records.)

Measurement of the ^{32}S(p,d)^{31}S Reaction and Its Astrophysical Implications

A Dissertation
Presented for the
Doctor of Philosophy
Degree
The University of Tennessee, Knoxville

Zhanwen Ma
December 2006

Acknowledgments

First and foremost, I would like to thank my advisors, Dr. Mike Guidry and Dr. Michael Smith for their guidance, encouragement, consideration, unconditional help and willingness to support my work throughout my studies. I deeply appreciate them for giving me the opportunity. I additionally would like to thank the other members of my committee: Dr. Yuri Kamyshkov, Dr. Carrol Bingham, and Dr. Lawrence Townsend for their help and guidance with the development of my thesis.

I want to give a very special thanks to Dr. Daniel Bardayan, Dr. Jeff Blackmon and Dr. Ray Kozub. I have learned so much from them. They are always willing to offer help with great patience.

I am also very grateful to my former advisors in China Institute of Atomic Energy, Prof. Xixiang Bai and Dr. Weiping Liu, for their invaluable help and guidance.

Thanks also to Dr. Raph Hix, Suzan Parete-koon, Ronald Livesay, Andy Chae, Eric Lingerfelt, Viktor Chupryna, Jason Scott, Dr. Kate Jones, Dr. Caroline Nesaraja, Dr. Steve Pain, Dr. Jeff Thomas, Dr. Micah Johnson, Dr. Dale Visser and Dr. Ryan Fitzgerald, for their generous help. Thanks goes as well to the HRIBF staff who have worked hard to provide beams.

Special thanks to my parents, my wife, my brother and sisters and other family members for all the support and encouragement that they have given me.

Abstract

The ^{30}P(p,γ)^{31}S reaction plays a crucial role in the synthesis of heavier nuclear species, from Si to Ca, in nova outbursts on ONe White Dwarfs [26, 28, 35]. However, its rate is very uncertain as a result of the lack of spectroscopic information on the levels above proton threshold in ^{31}S. The currently adopted rate of this reaction, based on statistical Hauser-Feshbach calculations [36], could have an uncertainty as much as a factor of 100 higher or lower under nova conditions [26].

To reduce these uncertainties, we have measured differential cross sections for the ^{32}S(p,d)^{31}S reaction and determined excitation energies for states in ^{31}S. A total of 26 states in ^{31}S were observed, including 17 above the proton threshold. Five new states were observed. Uncertainties in the excitation energies of states in the high energy region were significantly reduced. Spin and parity values were determined or constrained for 15 of the strongly populated levels through a distorted wave Born approximation (DWBA) analysis of the angular distributions, of which 6 were made for the first time.

A new ^{30}P(p,γ)^{31}S reaction rate was calculated utilizing the present experimental spectroscopic information. We confirmed the spin-parity assignment of $1/2^+$ for the state at 6263 keV which dominates the ^{30}P(p,γ)^{31}S reaction rate at lower temperatures in nova, while the state at 6544 keV dominates at temperatures above 0.2 GK (1 GK=1.0×10^9 Kelvin). Our results indicate that the ^{30}P(p,γ)^{31}S rate based on our resonance calculations is reduced by up to a factor of 10 at nova temperatures compared to the previous rate.

Nova element synthesis calculations using the new ^{30}P(p,γ)^{31}S reaction rate were performed, and predictions of isotopic abundance patterns were obtained. Production of elements in the Si-Ca mass region are found to be altered by as much as 40% using the new rate. Important isotopic ratios are found to agree well with observations on presolar grains thought to have a nova origin [34]. Of special interest are the close-to-solar ^{29}Si/^{28}Si ratio and large excess in ^{30}Si/^{28}Si found in our simulations, which are the most important features pointing to a nova origin of such grains.

Contents

List of Tables

List of Figures

Chapter 1

Introduction

1.1 General Overview

One of the most fundamental scientific questions is the origin of elements that form everything in the world including our bodies. The answer to this question begins with Eddington's landmark paper in 1920 [1], in which he proposed that nuclear reactions are the source that powers the stars. This was quantitatively illustrated by von Weizsäcker [2, 3], Bethe and Critchfield [4] and Bethe [5]. In their work the mechanism for converting hydrogen into helium was addressed. In 1957, Burbidge et al. [6] proposed that nuclear reactions are solely responsible for synthesis of all the elements heavier than hydrogen and helium in the stars.

The field of nuclear astrophysics was developed in the 20th century to understand the origin and evolution of the chemical elements. The generally accepted answer today is that hydrogen, helium and some lithium were produced in the Big Bang, and the rest of the elements were formed in a large variety of nuclear processes which occur in the interior or on the surfaces of stars. The evolution of stars begin with condensation of a cloud of gas and dust in the interstellar medium until temperature

and densities are high enough to ignite thermonuclear reactions. This hydrostatic hydrogen burning stage is maybe followed by a variety of additional burning stages depending on the total mass of the star. Low mass stars evolve into dwarfs, heavier stars into red giants, and even heavier stars will explode in supernovae.

Various numerical models have been developed to describe and track the evolution of these stellar environments. Nuclear reaction rates are crucial input for these models: the burning time scales, energy production, nucleosynthesis, and other critical features depend on the values of hundreds or thousands of reaction rates. The reaction rate formalism will be discussed in Chapter 2.

Of the various nuclear processes occurring in stars, hydrogen burning is the most important for both energy generation and nucleosynthesis. This is because hydrogen is the most abundant material and its Coulomb barrier is lowest among charged particles. Hydrogen burning can proceed quiescently or explosively depending on the stellar environments where it occurs.

1.2 Quiescent Hydrogen Burning

Stars are formed from interstellar medium by gravitational contraction. The interstellar medium consists of mostly hydrogen and may also contain heavier elements from previous generations of stars. During the contraction, the gravitational potential energy is converted into thermal energy, heating up the stellar interior. When the temperature reaches $\sim 10^7$ K, thermonuclear reactions become possible. Since hydrogen is the most abundant and its Coulomb barrier is the lowest, reactions involving these nuclei - "hydrogen burning" - start first. Here hydrogen is converted into helium and releases a large amount of energy. This released energy halts the gravitational

contraction temporarily. Hydrogen burning lasts several millions of years in massive stars and billions of years in stars of solar mass.

In first generation stars where only hydrogen is available, hydrogen burning proceeds predominately through the pp-chains. In second generation stars which contain heavier elements such as C, N, O, Ne, Na, Mg, and Al from previous stars, hydrogen burning can proceed through the catalytic CNO cycles, NeNa cycle and MgAl cycle.

pp-Chains. In stars with mass of our sun and core temperature $\sim 10^7$K, hydrogen burning is dominated by the pp-chains. The pp-chains consist of three nuclear reaction sequences as shown in figure 1.1:

pp-I: $p(p, e^+\nu_e)d(p, \gamma)^3He(^3He, 2p)^4He$.

pp-II: $p(p, e^+\nu_e)d(p, \gamma)^3He(\alpha, \gamma)^7Be(e^-, \nu_e)^7Li(p, \alpha)^4He$.

pp-III: $p(p, e^+\nu_e)d(p, \gamma)^3He(\alpha, \gamma)^7Be(p, \gamma)^8B(e^+\nu_e)^8Be^*(\alpha)^4He$.

The net result of the pp-chains is 4p $\rightarrow$ ^{4}He + 2e$^+$ + 2ν_e + 26.73 MeV.

CNO-Cycles. In more massive stars with mass M $>$ 2 M$_\odot$ (M$_\odot$ refers to the mass of the Sun) and core temperature $> 2\times10^7$, hydrogen burning is dominated by the CNO cycles (Fig. 1.2). Carbon and nitrogen nuclei serve as catalyst. The net result is same as that of the pp-chains but the energy released is much larger.

NeNa Cycle and MgAl Cycle. At a temperature of several 10^7K, additional cycles such as the NeNa Cycle and MgAl Cycle become possible to convert hydrogen into helium. Because of the high Coulomb barriers involved in these reactions, both cycles are unimportant for energy generation, but are important for the nucleosynthesis of elements in the Ne-Al mass region. The NeNa cycle reaction sequence is:

$^{20}Ne(p, \gamma)^{21}Na(e^+\nu)^{21}Ne(p, \gamma)^{22}Na(e^+\nu)^{22}Ne(p, \gamma)^{23}Na(p, \alpha)^{20}Ne$,

and the MgAl cycle is:

$^{24}Mg(p, \gamma)^{25}Al(e^+\nu)^{25}Mg(p, \gamma)^{26}Al(p, \gamma)^{27}Si(e^+\nu)^{27}Al(p, \alpha)^{24}Mg$,

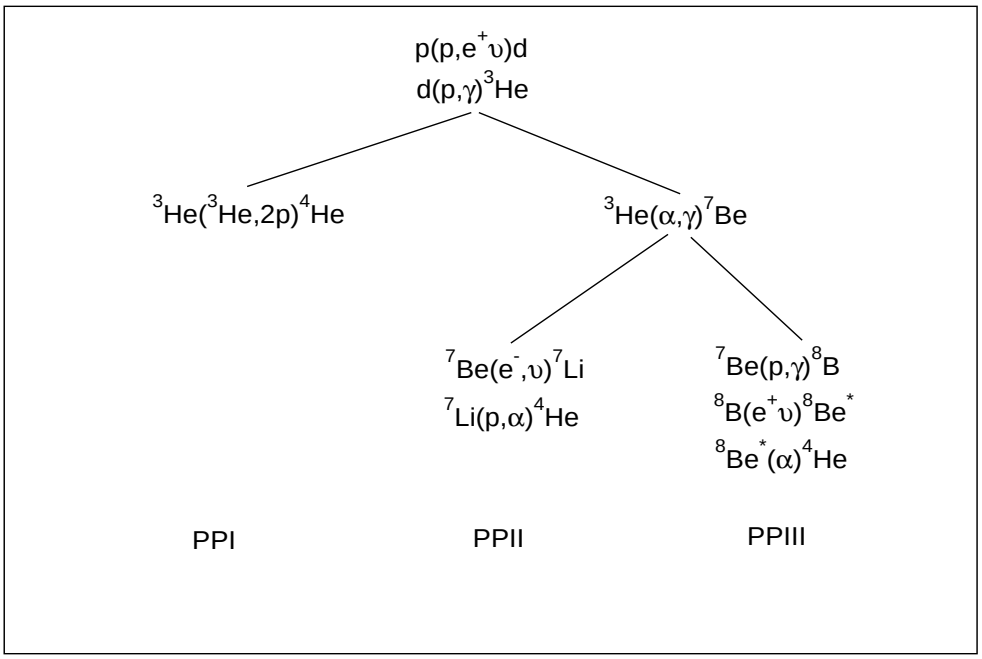

Figure 1.1: The pp-chains are shown.

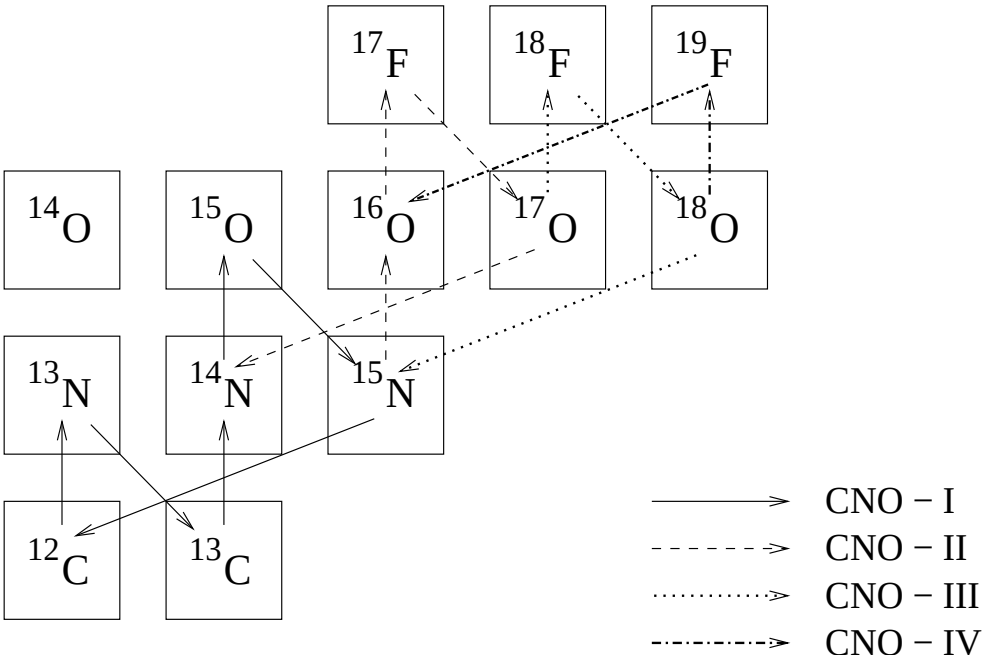

Figure 1.2: The CNO Cycles are shown.

or $^{24}Mg(p,\gamma)^{25}Al(e^{+}\nu)^{25}Mg(p,\gamma)^{26}Al^{*}(e^{+}\nu)^{26}Mg(p,\gamma)^{27}Al(p,\alpha)^{24}Mg$.
where $^{26}Al^{*}$ stands for the excited state of ^{26}Al.

1.3 Explosive Hydrogen Burning

In astrophysical environments with sufficiently high temperatures and densities, nuclear reactions become fast enough to bypass the β-decays in the CNO cycles and hydrogen burning can proceed explosively. Such burning occurs in nova explosions [7].

1.3.1 Novae

Classical novae occur in close binary star systems consisting of a white dwarf star and a companion giant star. When the companion star overflows its Roche lobe (the volume enclosed by the surface at which the gravitational potentials of the two stars are equal) [16] (Fig. 1.3), matter from the star flows through the inner Lagrangian point and forms an accretion disk before spiraling down onto the surface of the white dwarf [16] (Fig. 1.4). The accreted material forms a thin but very dense envelope on the surface of the white dwarf.

Because of its high density, the white dwarf has a very strong gravitational field. Gas accreted onto its surface has very high velocity, resulting in extremely high temperature upon impact [17]. When the temperature reaches ~20 million K, nuclear fusion reactions are ignited. The energy generation in this early accretion stage is dominated by the pp-chains and the CNO-cycles. The energy released from the nuclear reactions further heat up the envelope and causes the temperature continue to rise. Because of the degeneracy of the matter, the pressure is independent of the temperature. As a result, the degenerate gas can not cool down by expansion as in the case of normal gas. This causes the nuclear reactions to go even faster as reaction

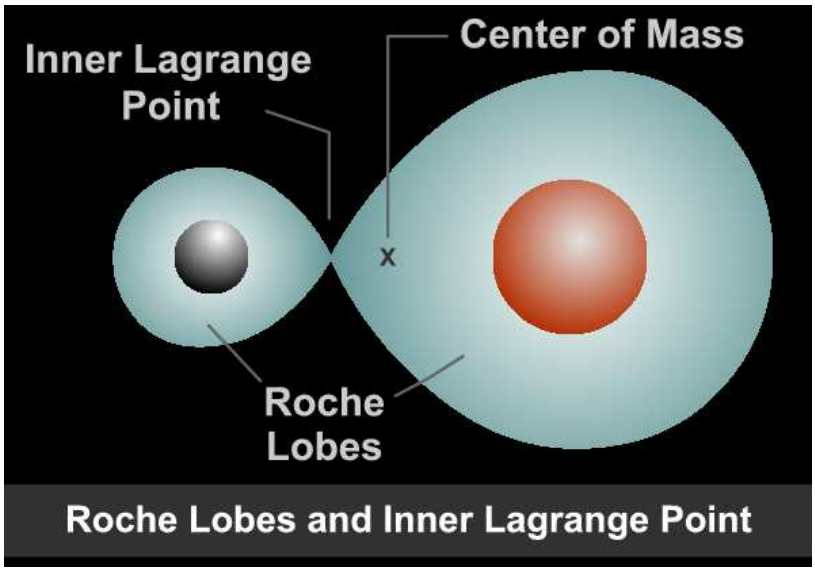

Figure 1.3: Roche Lobes and Inner Lagrange Point are shown for a close binary system. (http://www.onlineastronomy.com).

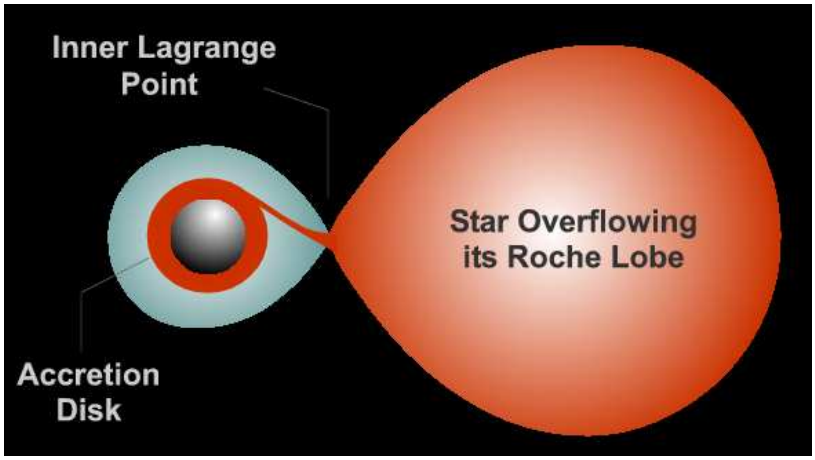

Figure 1.4: A close binary system overflowing its Roche Lobe

rates depend on temperature exponentially, and to release an enormous amount of energy. Finally a thermonuclear runaway (TNR) is triggered, ejecting most of the accreted material.

The composition of the accreted material from the companion star is solar-like and therefore abundant in hydrogen. However spectroscopic study of some novae shows that their ejecta are significantly enhanced with respect to solar composition in oxygen, neon, magnesium, silicon, sulphur, and other heavier elements up to calcium (see, e.g., Ref. [8, 9, 32]). This implies that there is a mixing between the accreted solar-like material and the underlying white dwarf material some time during the evolution. Carbon-oxygen white dwarfs are rich in carbon and oxygen, while in the oxygen-neon white dwarfs, not only the CNO group nuclei, heavier elements like neon and magnesium, are also present. CO white dwarfs result from the evolution of stars with an initial mass ∼1-8 $M_\odot$, and ONe white dwarfs are thought to result from the evolution of stars with an initial mass of 8-10 $M_\odot$. The mixing mechanism, however, is still uncertain.

1.3.2 Nova Nucleosynthesis

Typical nova outbursts occur at peak temperatures between T_9=0.1 to 0.4 (where T_9 is temperature in units of 10^9K) and densities $\rho \simeq 10^3$g/cm^3. Under these conditions, the β-decay of ^{13}N can be bypassed by the ^{13}N(p,γ)^{14}O reaction and the CNO cycle, which is the dominant reaction sequences prior to TNR, is converted to the Hot CNO (HCNO) cycle (see Fig. 1.5 [29]). The reaction sequence in the HCNO cycle is:
$^{12}C(p,\gamma)^{13}N(p,\gamma)^{14}O(e^+\nu_e)^{14}N(p,\gamma)^{15}O(e^+\nu_e)^{15}N(p,\alpha)^{12}C$.
There are several additional reaction sequences in the HCNO cycle [17]. The HCNO cycle is expected to dominate energy production in nova explosions. From the point

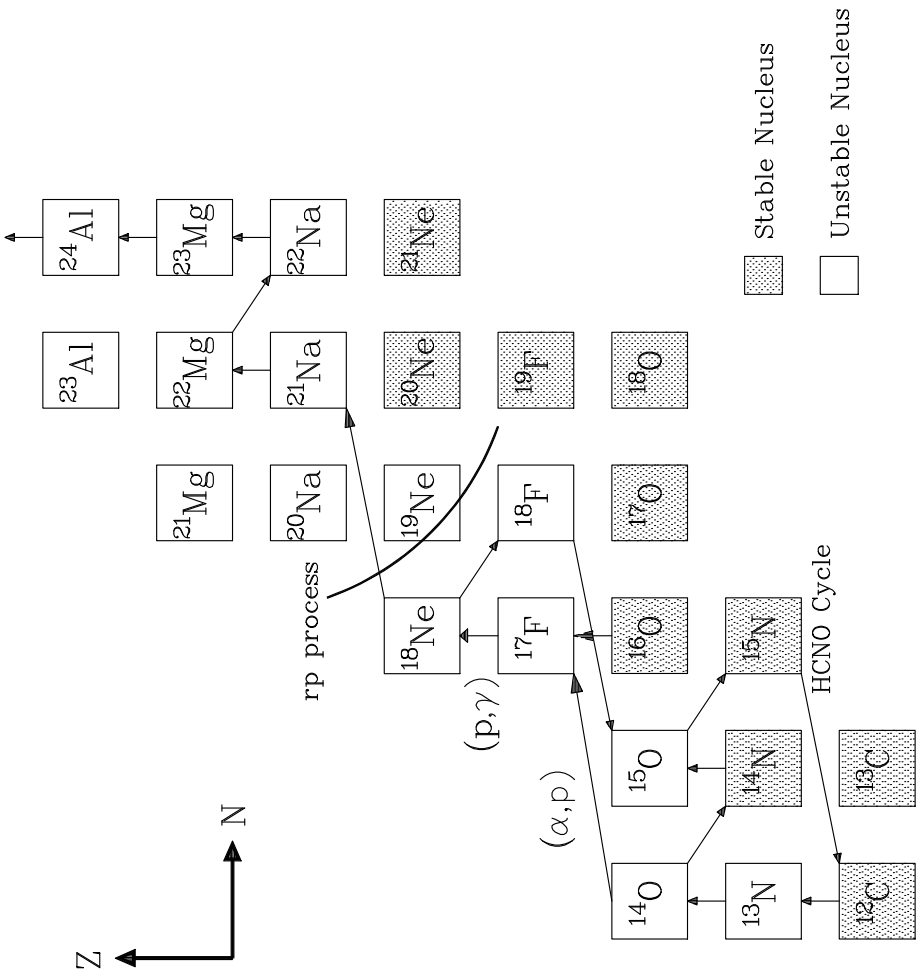

Figure 1.5: The hot CNO-cycle is shown. (D. W. Bardayan, Thesis, Yale University, 1999).

of view of nucleosynthesis, the operation of the HCNO cycle is responsible for the enrichment of CNO group nuclei.

On the other hand, as stated previously, nova explosions may also occur on oxygen-neon white dwarfs (hereafter, ONe novae). ONe white dwarfs, more massive than CO white dwarfs, contain not only CNO-group nuclei, but also neon, sodium, aluminum, and other intermediate-mass nuclei [10, 11, 31]. Proton captures on these seed nuclei in the NeNa-MgAl region drive the nuclear activity up to the Si-Ca mass region (see Fig. 1.6) [28,52]. These reactions are not important for energy production, due to the high Coulomb barriers involved, but are important for the nucleosynthesis of elements in the heavier Si-Ca mass region.

Study of nova nucleosynthesis is of considerable importance for several reasons. First, novae synthesize numerous isotopes (^{13}C, ^{15}N, ^{17}O) difficult to make in other astrophysical environments. Heavier elements in the Si-Ca mass region are also synthesized in nova explosions on ONe white dwarfs. Abundance determinations from some observed novae have shown the presence of enhanced Si-Ca nuclei in the ejecta [32,33]. Secondly, γ-ray emitting species are synthesized in nova outbursts and therefore are important for observational study of novae (Ref. [28] and references therein). Observations of γ rays have been attempted with current satellites such as the International γ-Ray Astrophysics Laboratory (INTEGRAL) [12] and will be made in the future with more sensitive instruments [e.g., the Gamma-ray Large Area Space Telescope (GLAST) [13]]. These emissions include a 478 keV line from ^{7}Li, a 1275 keV line from ^{22}Na, and a 511 keV line from ^{18}F. In the Si-Ca region γ-ray emission of 511 keV [14] and 2128 keV [15] lines from β^{+}-decay of the medium lived ^{34m}Cl has been suggested. Particularly important is the observation of the 1809 keV line, signature of ^{26}Al decay which provided direct proof that nucleosynthesis is "recently" active (in the last million years) in the Galaxy. Third, the discovery of several presolar

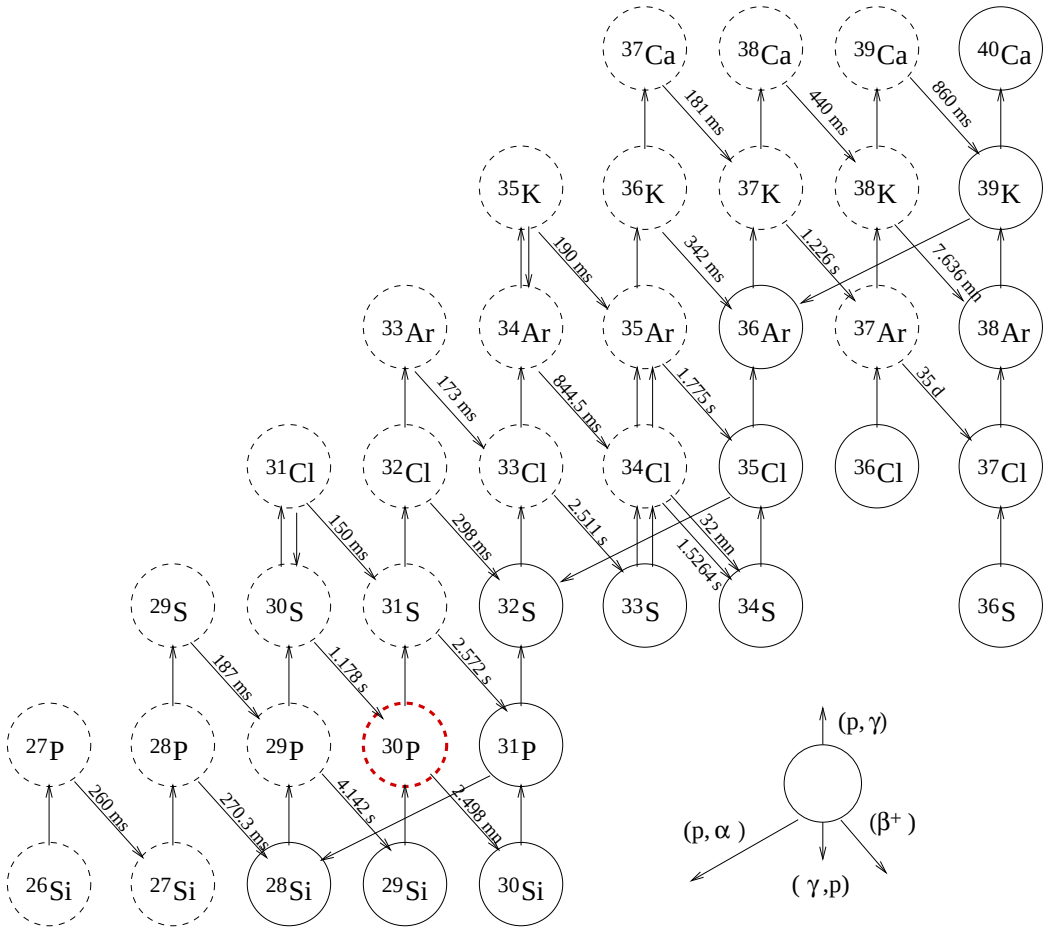

Figure 1.6: Main nuclear reaction paths in the Si-Ca mass region in ONe novae. ^{30}P is a mandatory passing point towards ^{32}S and heavier elements. (J. Jose, Astrophys. J., **560**, 897, 2001.)

grains thought to have a nova origin characterized by low $^{12}C/^{13}C$ and $^{14}N/^{15}N$ ratios, high $^{26}Al/^{27}Al$ ratio, close-to-solar $^{29}Si/^{28}Si$, and large excesses in $^{30}Si/^{28}Si$ [34], points out the importance of good determination of the abundance pattern and nova nucleosynthesis, in particular in the Si-Ca mass region.

1.3.3 The Importance of the $^{30}P(p,\gamma)^{31}S$ Reaction Rate in Nova Nucleosynthesis

The previous section demonstrates the necessity of a better understanding of nova nucleosynthesis in the Si-Ca mass region. There have been a number of previous studies of this [26, 28, 35]. In their study, José *et al.* [28] found that the $^{30}P(p,\gamma)^{31}S$ reaction rate plays a crucial role in the synthesis of heavier nuclear species – from Si to Ca – in nova outbursts on ONe White Dwarfs. Species beyond sulphur are produced via two paths, either $^{30}P(p,\gamma)^{31}S(p,\gamma)^{32}Cl(\beta^+)^{32}S$ or $^{30}P(p,\gamma)^{31}S(\beta^+)^{31}P(p,\gamma)^{32}S$. The path through $^{29}P(p,\gamma)^{30}S(p,\gamma)^{31}Cl$ is inhibited by the instant inverse photodisintegration reaction $^{31}Cl(\gamma,p)^{30}S$, followed rapidly by a β^+-decay leading back to ^{30}P. The path through $^{30}P(\beta^+)^{30}Si(p,\gamma)^{31}P(p,\gamma)^{32}S$ is also strongly inhibited by the slow ^{30}P β^+-decay. Thus ^{30}P is a predominant passing point towards heavier isotopes beyond sulphur. José *et al.* varied the $^{30}P(p,\gamma)^{31}S$ reaction rate within its uncertainty [28] to explore its effects on nova nucleosynthesis. The increase by a factor of 100 affects only the ^{30}Si yield significantly, and since the path toward ^{31}S is favored, much less ^{30}Si is left in the envelope. The impact on the other nuclear species is very limited. On the contrary, a reduction by a factor of 100 of the $^{30}P(p,\gamma)^{31}S$ rate changes the expected yields dramatically. Since ^{30}P β^+-decays compete favorably with proton captures, an important enhancement of ^{30}Si is obtained. However, the synthesis of elements above Si is hindered significantly by a factor of 10 with respect to values found with the

nominal rate. Iliadis *et al.* [26] have also performed one-zone nucleosynthesis calculations to investigate the effects of thermonuclear reaction rate uncertainties on nova nucleosynthesis. They found qualitative and quantitative agreement with José *et al.* We have performed nova nucleosynthesis simulations based on a multiple spatial zones model [20, 35]. The influence of the ^{30}P(p,γ)^{31}S rate on nova nucleosynthesis found in our calculations agrees well with previous studies (see Chapter 3 for details).

Direct measurement of the ^{30}P(p,γ)^{31}S reaction rate has not been possible due to difficulties in developing radioactive ^{30}P beams and ^{30}P is too short lived to be a target. The currently adopted rate is based on a statistical Hauser-Feshbach calculation [36] and has an uncertainty that could be as high as a factor of 100 higher or lower [26]. This is because such rates assume capture through nuclear levels where there is a high level density in the compound nucleus. While this assumption is valid for higher mass nuclei (A>40) at high temperatures, it is not generally true for novae. Thus, to obtain a realistic reaction rate, one must consider contributions from each of the individual resonances, especially those that lie within the Gamow window (see Chapter 2). The information needed for the calculation of the individual resonance contribution includes the excitation energy, spin and parity, total width, partial width, etc.

1.4 Previous Work on ^{31}S

At temperatures of nova importance where $T_9 < 0.5$ GK, the most effective energies for thermonuclear reactions as given by Eq. (2.12) is $\sim$ 450 keV with a width, $\Delta \sim$ 350 keV. Therefore, states in ^{31}S within $\sim$1 MeV above the ^{30}P+p threshold (6.13 MeV – 7.15 MeV) are the most important for the ^{30}P(p,γ)^{31}S stellar reaction rate.

Ajzenberg-Selove and Wiza [42] determined the excitation energies of many of the resonances in ^{31}S using the ^{32}S(^{3}He,α)^{31}S reaction. 39 levels were observed in their measurement, including 16 above the ^{30}P+p threshold. However, their measurement did not have the capability for spin and parity determination.

Moss [45] studied the properties of the ^{31}S states using the ^{32}S(^{3}He,α)^{31}S and ^{32}S(^{3}He,$\alpha\gamma$)^{31}S reactions. He was able to locate 42 levels in ^{31}S. For 11 of the first 17 levels, ℓ_α values have been determined. The ^{32}S(^{3}He,$\alpha\gamma$)^{31}S reaction has been studied by applying the particle - γ correlation method of Litherland and Ferguson. Spins and parities were obtained for the first 6 excited states but none of these is above the ^{30}P+p threshold.

Davidson et al. [44] investigated the level structure of ^{31}S using the reaction ^{29}Si(^{3}He,n)^{31}S, and neutron-γ coincidence measurements of ^{29}Si(^{3}He,nγ)^{31}S and ^{29}Si(^{3}He,n$\gamma\gamma$)^{31}S. They were able to identify in neutron time-of-flight (TOF) spectra some high energy states up to 8.5 MeV. They also identified for the first time the two isospin T = 3/2 states in ^{31}S at 6277 keV and 7006 keV, respectively.

Vernotte et al. [46] investigated the ^{32}S(^{3}He,α)^{31}S reaction at incident energy $E_{^3He}$ = 25 MeV. Spectroscopic factors were obtained for 22 levels of ^{31}S through the DWBA analysis of the experimental angular distributions. Twenty pairs of levels were identified as mirror states in the ^{31}S and ^{31}P nuclei, 3 pairs of them above the single nucleon separation threshold.

In a recent study [47], excited states in ^{31}S and ^{31}P were populated using the ^{12}C(^{20}Ne,nγ)^{31}S and ^{12}C(^{20}Ne,pγ)^{31}P reactions, respectively. High spin states of positive and negative parity were observed in ^{31}S for the first time. An extensive new γ-decay scheme was developed. The mirror energy differences (MEDs) were studied.

At present, there are 17 levels known within 1 MeV above the ^{30}P+p threshold in ^{31}S that may contribute to the ^{30}P(p,γ)^{31}S reaction rate at nova temperatures. The

excitation energies of these levels are known to within uncertainties ∼10 keV, but the spins and parities (for all but two) are not. This lack of spectroscopic information makes it impossible to calculate a realistic ^{30}P(p,γ)^{31}S reaction rate. Moreover, as can be seen in Chapter 2, Eq. (2.4), the reaction rate depends very sensitively on the resonance energy, and thus improvement on the uncertainties of the excitation energies are important. It is the purpose of the present ^{32}S(p,d)^{31}S measurement to clarify the level structure of ^{31}S above the ^{30}P+p threshold.

Chapter 2

Reaction Rate Formalism

2.1 Stellar Reaction Rate

For reactions of the type: $a + X \rightarrow C^* \rightarrow b + Y$, the thermonuclear reaction rate is given by Rolfs et al. [17] as

$$r = N_a N_X \sigma(v) v \tag{2.1}$$

where N_a and N_X are the number densities of the two nuclei in the entrance channel, v is the relative velocity of particles a and $\sigma(v)$ is the velocity-dependent cross section.

In normal stellar matter the stellar gas is non-degenerate and the nuclei can be assumed to be in thermodynamic equilibrium. The distribution of relative velocities for particle pairs can be described by a Maxwell-Boltzmann distribution :

$$\phi(v) \;=\; 4\pi v^2 \left(\frac{\mu}{2\pi kT}\right)^{\frac{3}{2}} exp\left(-\frac{\mu^2}{2kT}\right) \tag{2.2}$$

where μ is the reduced mass and T is the temperature. Thus the reaction rate averaged over the velocity distribution becomes :

$$r = N_a N_X \int_0^\infty \sigma(v) v \phi(v) dv = N_a N_X < \sigma v > \tag{2.3}$$

where $< \sigma v >= \int_0^\infty \phi(v)\sigma(v)v dv$, the averaged value of the product of the relative velocity and cross section, is referred to as the reaction rate per particle pair.

Using the formula of center of mass energy $E = \frac{1}{2}\mu v^2$, the reaction rate per particle pair can be written as [17]:

$$< \sigma v > \;=\; \left(\frac{8}{\pi\mu}\right)^{1/2} \left(\frac{1}{kT}\right)^{3/2} \int_0^\infty \sigma(E) E \exp\left(-\frac{E}{kT}\right) dE \tag{2.4}$$

For two positively charged particles, they must overcome the repulsive Coulomb barrier. The probability for two particles with relative velocity v to tunnel through the Coulomb barrier is proportional to the penetration factor :

$$P = exp(-2\pi\eta) \tag{2.5}$$

where η is the Sommerfeld parameter :

$$\eta = \frac{Z_a Z_X e^2}{\hbar v} \tag{2.6}$$

and Z_a and Z_X represent the integral charges of the particles a and X. The cross section is thus proportional to the penetration factor :

$$\sigma(E) \propto exp(-2\pi\eta) \tag{2.7}$$

It is therefore convenient to factor out this term and express the nuclear cross section in terms of the astrophysical S-factor, $S(E)$ as follows :

$$\sigma(E) = \frac{1}{E}\exp(-2\pi\eta)S(E), \tag{2.8}$$

where the factor of $1/E$ is due to the fact that the nuclear reaction cross section is always proportional to a geometrical factor $\pi\lambda^2$, where λ is the de Broglie wavelength:

$$\pi\lambda\!\!\!^{-2} \propto \frac{1}{E}. \tag{2.9}$$

The benefit of expressing the cross section in this way is that two of the strongly energy-dependent factors in the nuclear cross sections are factored out explicitly, leaving mostly only nuclear intrinsic information in the residual function of energy, $S(E)$, which usually varies very slowly with energy. Because of this weak energy dependence, the S-factor is much more useful in extrapolating measured cross sections to astrophysical energies.

Inserting Eq. (2.8) into Eq. (2.4), one obtains the reaction rate per particle pair ,$< \sigma v >$ as follows [17]:

$$< \sigma v >= \left(\frac{8}{\pi\mu}\right)^{1/2}\left(\frac{1}{kT}\right)^{3/2}\int_0^\infty S(E)\exp\left(-\frac{E_G^{1/2}}{E^{1/2}} - \frac{E}{kT}\right)dE, \tag{2.10}$$

where the quantity E_G, which arises from the barrier penetrability, is called the Gamow energy and is given by

$$E_G = 2\mu(\pi e^2 Z_a Z_X/\hbar)^2 \tag{2.11}$$

The energy dependence of the integrand in equation (2.10) is governed primarily by the exponential term. The term $exp[-(E_G/E)^{1/2}]$ is from the penetration through the Coulomb barrier and the term, $exp(-E/kT)$ is from the high-energy tail of the Maxwell-Boltzmann distribution. The product of these two terms leads to a peak of the integrand around the effective energy E_0. The peak is referred to as the Gamow peak (Fig. 2.1).

Non-resonant nuclear reactions take place in a relatively narrow energy window around the effective energy E_0 at a given stellar temperature T, and the $S(E)$ factor frequently varies very slowly with energy. By assuming that $S(E)$ is constant and taking the first derivative of the integrand in equation (2.10), one can find the most effective energy, E_0 for thermonuclear reactions at a given temperature T [17]:

$$E_o = \left(\frac{E_G^{1/2} kT}{2} \right)^{2/3} = 1.22 (Z_a^2 Z_X^2 A T_6^2)^{1/3} \text{ keV}. \tag{2.12}$$

The effective width of the Gamow window, Δ, is defined as the $1/e$ width of the peak:

$$\Delta = \frac{4}{3^{1/2}} (E_o kT)^{1/2} \tag{2.13}$$

The integrand in equation (2.10) decreases exponentially for energies outside of the Gamow window, therefore the thermonuclear reaction rate is very sensitive to the properties of resonances which lie in or near the Gamow window. For the ^{30}P+p system the Gamow window is shown in Figure 2.1 for a typical nova peak temperature of $T_9 = 0.4$.

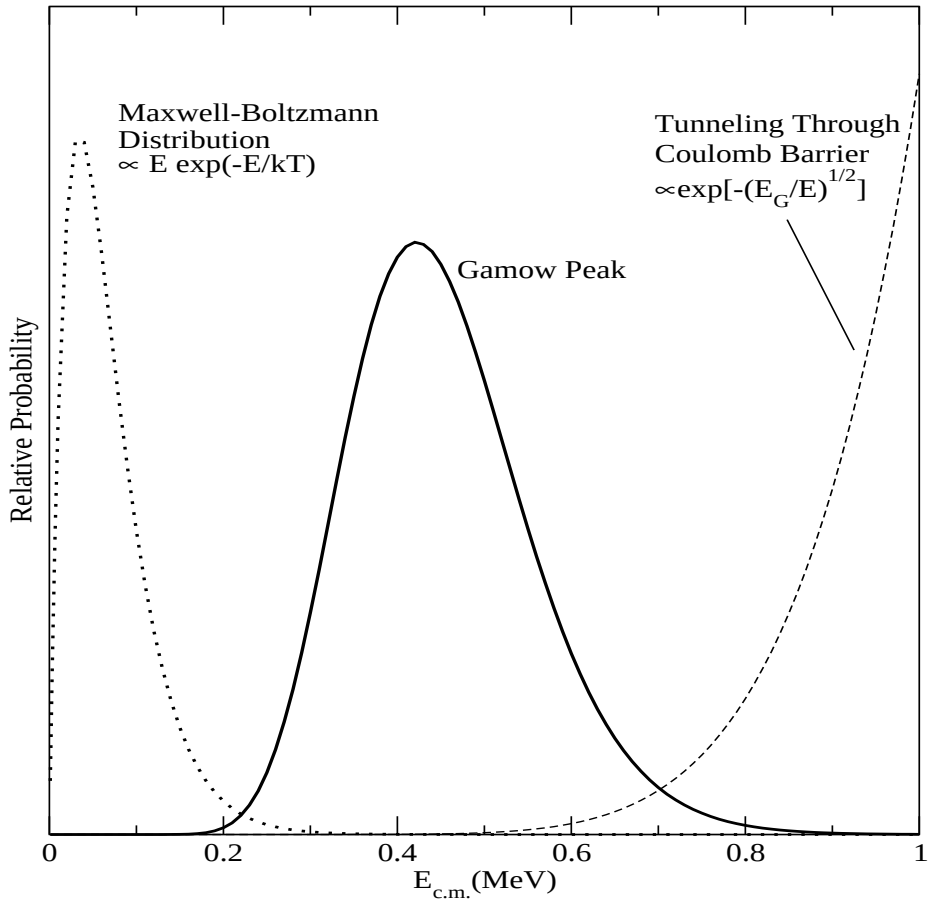

Figure 2.1: The Maxwell-Boltzmann distribution, penetrability function, and Gamow peak are shown for the ^{30}P+p system at $T_9 = 0.4$. The most effective energy for this nuclear reaction, E_o, is at 398 keV for these conditions.

2.2 Resonant Reaction Rate

For a nuclear reaction that proceeds through the compound nucleus reaction mechanism, $a + X \rightarrow C^* \rightarrow b + Y$, the cross section can be dominated by the properties of just a few resonances. The nuclear cross section for a single level is expressed by the Breit-Wigner formula:

$$\sigma_{BW}(E) = \pi\lambda\!\!\!^{-2} \frac{2J+1}{(2J_a+1)(2J_X+1)} \frac{\Gamma_a(E)\Gamma_b(E)}{(E-E_R)^2 + (\Gamma(E)/2)^2} \tag{2.14}$$

where J, J_a, and J_X are the spins of the resonance and the two incident nuclei a and X, respectively. E_R is the energy of the resonance; Γ_a, Γ_b, and Γ are the partial widths in the entrance and exit channels and the total width, respectively.

Inserting equation (2.14) into equation (2.10), the stellar reaction rate per particle pair is given by:

$$< \sigma v >= \left(\frac{8}{\pi\mu}\right)^{1/2} \frac{1}{(kT)^{3/2}} \int_0^\infty \sigma_{BW}(E) E exp\left(-\frac{E}{kT}\right) dE \tag{2.15}$$

If the resonance is narrow and isolated, the energy-dependent terms in the integrand in equation (2.15) changes very little over the resonance region, this expression can be reduced to [17]:

$$< \sigma v >= \left(\frac{2\pi}{\mu kT}\right)^{3/2} \hbar^2 (\omega\gamma)_R \exp\left(-\frac{E_R}{kT}\right) \tag{2.16}$$

where $\omega = \frac{2J+1}{(2J_a+1)(2J_X+1)}$ is the statistical factor. $\gamma = \Gamma_a\Gamma_b/\Gamma$. The product of $\omega\gamma$ is referred to as the resonance strength:

$$\omega\gamma = \frac{2J+1}{(2J_a+1)(2J_X+1)} \frac{\Gamma_a\Gamma_b}{\Gamma} \tag{2.17}$$

If several well-separated resonances contribute to the reaction cross section, their summed contribution to $< \sigma v >$ is given by:

$$< \sigma v >= \left(\frac{2\pi}{\mu kT}\right)^{3/2} \hbar^2 \sum_i (\omega\gamma)_i \exp\left(-\frac{E_i}{kT}\right). \tag{2.18}$$

If, on the other hand, the resonances are broad, then the evaluation of the stellar reaction rate $< \sigma v >$ must explicitly take into account the energy dependence of the widths [18]:

$$\Gamma_\ell(E) = \frac{2\hbar}{R_n}\left(\frac{2E}{\mu}\right)^{1/2} P_\ell(E, R_n)\theta_\ell^2 \tag{2.19}$$

where Γ_ℓ is the partial width for the ℓ^{th} partial wave, R_n is the radius of the reaction channel, θ_ℓ^2 is called the reduced width, and P_ℓ is the penetrability:

$$P_\ell = \frac{1}{F_\ell^2(E, R_n) + G_\ell^2(E, R_n)} \tag{2.20}$$

where the functions $F_\ell(E, R_n)$ and $G_\ell(E, R_n)$ are the regular and irregular Coulomb wave functions, which are solutions to the Schrödinger equation with a Coulomb potential.

The dimensionless quantity θ_ℓ^2 is generally determined experimentally and contains the nuclear structure information. It is the square of the overlap amplitude of the compound nuclear state with the reacting particles in the entrance channel with relative angular momentum ℓ. The penetrability P_ℓ decreases very rapidly with increasing relative orbital angular momentum. Because of this, in calculations of reaction rates, usually only the minimum possible ℓ-value is used.

2.3 Non-Resonant Reaction Rate

There are cases where nuclear reactions do not proceed through the compound nucleus but instead through non-resonant mechanisms. There are two mechanisms contribute to the non-resonant nuclear reaction rate [17]: the direct capture process, and reactions on the tails of higher energy resonances. The direct capture process is a one-step process in which the two reacting particles interact through the Coulomb and nuclear potentials, resulting in a capture into a bound state. It can occur at any energy since no resonant levels in the compound nucleus are involved.

The non-resonant S-factor usually varies slowly over the energies in the Gamow window. As an approximation it can be regarded as constant and taken out of the integrand of equation (2.10). The nuclear reaction rate becomes [17]:

$$< \sigma v > = \left(\frac{2}{\mu}\right)^{1/2} \frac{\Delta}{(kT)^{3/2}} S(E_o) F(\tau) \exp(-\tau) \tag{2.21}$$

$$F(\tau) = 1 + \frac{5}{12}\frac{1}{\tau} - \frac{35}{288}\frac{1}{\tau^2} + \ldots \tag{2.22}$$

where $\tau = \frac{3E_o}{kT}$ and Δ is the $1/e$ width of the Gamow window given in equation (2.13).

If only the first term of $F(\tau)$ is kept, the following expression is obtained for the reaction rate:

$$< \sigma v >= \left(\frac{2}{\mu}\right)^{1/2} \frac{\Delta}{(kT)^{3/2}} S(E_o) \exp\left(-\frac{3E_o}{kT}\right). \tag{2.23}$$

2.4 Reverse Reaction Rate

In astrophysical sites where the stellar temperature is low, nuclear reactions occur predominantly for those reactions with positive Q-values. As the temperature rises, there are more and more particles with energies $E \geq Q$, the reverse reactions become more and more significant. This is particularly true for violent environments such as nova outbursts where temperatures can reach as high as ~ 0.4 GK. Thus both forward and reverse reactions must be taken into account.

For a reaction $a + X \rightarrow C^* \rightarrow b + Y$, the cross section for its reverse reaction, $b+Y \rightarrow C^* \rightarrow a+X$, is given as follows according to the principle of detailed balance:

$$\frac{\sigma_{bY}}{\sigma_{aX}} = \frac{m_a m_X E_{aX}(2J_a+1)(2J_X+1)}{m_b m_Y E_{bY}(2J_b+1)(2J_Y+1)}, \tag{2.24}$$

where m_i is the mass, E the center-of-mass energy, and J the angular momentum. Insert equation (2.24) into equation (2.4) and using the relation $E_{bY} = E_{aX} + Q$, the ratio of reaction rate per particle pair can be written as [17]:

$$\frac{< \sigma v >_{bY}}{< \sigma v >_{aX}} = \frac{(2J_a+1)(2J_X+1)}{(2J_b+1)(2J_Y+1)} \left(\frac{\mu_{aX}}{\mu_{bY}}\right) exp\left(-\frac{Q}{kT}\right) \tag{2.25}$$

Specifically, for a radiative capture where particle b is a photon, forward and reverse rates are related by [25]:

$$\frac{\lambda_{\gamma Y}}{N_A < \sigma v >_{aX}} = 9.8685 \times 10^9 T_9^{3/2} \frac{(2J_a+1)(2J_X+1)}{2J_Y+1} \left(\frac{A_a A_X}{A_Y}\right)^{3/2} e^{-11.605 Q/T_9}, \tag{2.26}$$

where λ is the photodisintegration rate per second, Q is in MeV, and T_9 is temperature in GK.

Chapter 3

Multi-Zone Simulations of Nova Nucleosynthesis

In Chapter 1, we have demonstrated the crucial role played by the ^{30}P(p,γ)^{31}S reaction rate in nova nucleosynthesis in the intermediate-mass region, from Si to Ca. We have also addressed the importance of a more accurate determination of the nova nucleosynthesis mechanism. There have been a number of attempts for this purpose. (see, e.g., Ref. [22, 26–28]). Many of these studies only follow the evolution of one zone, i.e., the hottest zone. This will bring substantial uncertainties since the hydrodynamical environment in the cooler, less dense outer layers is quite different from that of the hotter, denser inner zones, and nuclear reaction rates depend sensitively on temperature (exponentially) and density linearly. It is therefore the purpose that we performed simulations based on a multi-zone post-processing model at ORNL to explore the effect of the ^{30}P$(p,\gamma)^{31}$S reaction rate variation on nova nucleosynthesis. In contrast with the models used in previous studies, this multi-zone model divides the accreted envelope into smaller zones (see Fig. 3.1), the nuclear reaction network calculations are performed on each zone and the final composite abundance pattern

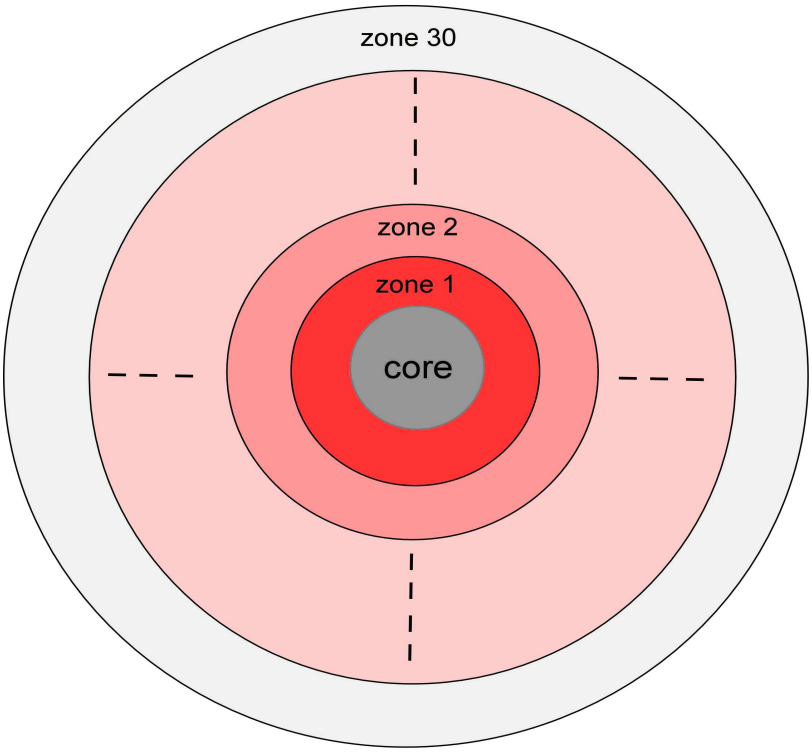

Figure 3.1: A schematic drawing of the multi-zone model (core and zone size not to the actual values). The entire envelope is divided into $\sim$ 30 zones. Each zone is described by a hydrodynamic trajectory which gives the temperature and density of the nova as a function of time. Zone masses are used to determine the weighing factors when calculating composite abundances.

is obtained by an addition of the abundances of all zones weighted by the mass of the zone. The network calculation begins with a set of initial abundances for all isotopes involved in the reaction network, and evolves them over time to the conclusion of the nucleosynthesis event when the temperature drops too low for further nuclear burning to occur. Hydrodynamic evolution is assumed to be performed externally, in our case, using a set of pre-prepared hydrodynamic histories called hydrodynamic trajectories. Each zone is assigned a hydrodynamic trajectory which is closely coupled with the network.

The nuclear reaction network used in our multi-zone simulations is developed by Hix and Thielemann [20]. My colleague S. Parete-Koon and I wrote a number of programs to present and analyze the output data. In the following sections I will first give a brief description of the nuclear reaction network used in our calculation. Then I will give an introduction of the input data files required by the network calculations and how to prepare them. Finally, to explore the effect of the $^{30}\mathrm{P}(p,\gamma)^{31}\mathrm{S}$ rate variation on nova nucleosynthesis, we have varied the $^{30}\mathrm{P}(p,\gamma)^{31}\mathrm{S}$ rate by a factor of 100 and 10 up and down within currently known uncertainties [26], and performed network calculations on a 1.25 $\mathrm{M}_{\odot}$ ONe white dwarf (WD) nova, a 1.35 $\mathrm{M}_{\odot}$ ONe WD nova and a 1.00 $\mathrm{M}_{\odot}$ CO WD nova. Results and discussion are presented.

3.1 Nuclear Reaction Network

As addressed in Chapter 1, it is the nuclear reactions that power the stars and synthesize the elements that make up our universe. The evolution of stars is closely connected with these reactions on the nuclear species inside its interior. The abundance, Y, for a specific species is dependent on the reactions that create and/or

destroy it during the star's evolution. All of these reaction rates are sensitively dependent on the temperature, which is in turn greatly affected by the energy released or absorbed by the reactions themselves. The set of differential equations which ties the physics of interacting nuclei to an abundance pattern is a reaction network [19].

Many types of nuclear reactions are of astrophysical importance. These include the emission or absorption of nuclei and nucleons, photons and leptons (electrons, neutrinos, etc.). As a result, nuclear reactions involve three of the four fundamental forces, the nuclear strong, weak and electromagnetic forces.

This large number of reaction types can be divided into three categories based on the number of nuclei involved in the reactions [20]. These are, (1), reactions involving a single nucleus such as decays, electron and positron captures, photodisintegrations, and neutrino induced reactions, (2), reactions involving two nuclei like proton, neutron and alpha capture reactions, and (3), reactions involving three reactant nuclei such as the triple alpha process.

The time derivatives of the number densities of each nuclear species in an astrophysical environment can be written in terms of the reaction rate, r, as [20]:

$$\frac{\partial n_i}{\partial t}|_{\rho=const} = \sum_j N^i_j r_j + \sum_{j,k} N^i_{j,k} r_{j,k} + \sum_{j,k,l} N^i_{j,k,l} r_{j,k,l}, \tag{3.1}$$

where the three sums are over reactions which produce or destroy nuclear species i with 1, 2 and 3 reactant nuclei, respectively. The N's represent the number of the nuclei and given by

$N^i_j = N_i$, $N^i_{j,k} = N_i / \prod_{m=1}^{n_m} \mid N_{j_m} \mid !$, and $N^i_{j,k,l} = N_i / \prod_{m=1}^{n_m} \mid N_{j_m} \mid !$.

They can be positive if the nuclear species I is created and negative if it is destroyed.

In addition to nuclear reactions, the number densities can also change with the expansion or contraction of the stellar medium. To separate the nuclear changes from

the hydrodynamics changes, we use the nuclear abundance instead of the number density n_i

$$Y_i = \frac{n_i}{\rho N_A}, \tag{3.2}$$

where ρ is the density and N_A is the Avagadro's constant.

If equation (3.2) is inserted in equation (3.1), we obtain [20]:

$$\begin{aligned} \frac{\partial Y_i}{\partial t} &= \sum_j N_j^i \lambda_j Y_j \\ &+ \sum_{j,k} N_{j,k}^i \rho N_A < \sigma v >_{j,k} Y_j Y_k \\ &+ \sum_{j,k,l} N_{j,k,l}^i \rho^2 N_A^2 < \sigma v >_{j,k,l} Y_j Y_k Y_l \end{aligned} \tag{3.3}$$

where λ is the reaction rate on a single nucleus and $N_A < \sigma v >$ is the reaction rate per particle pair or trio which is discussed in Chapter 2.

The rate of the energy released which is uniquely determined by the abundance changes, is given by

$$\dot{\varepsilon}_{nuc} = -\sum_i N_A M_i c^2 \dot{Y}_i (\text{MeV/g s}) \tag{3.4}$$

Although in principle, the initial value problem presented by the set of nuclear network equations (3.3) can be solved by any method. However the physical nature of the quantities λ's and $< \sigma v >$'s greatly limits the feasible choices of the methods. The large number of different types of reactions reflected in the λ's and $< \sigma v >$'s. in equation (3.3) exhibit a wide range of reaction timescales. The mean lifetime of particle j against destruction by particle k is given by:

$$\tau_k(j) = 1/(< \sigma v >_{j,k} n_k) \tag{3.5}$$

Systems whose solutions depend on a wide range of timescales are termed ***stiff***. Because of the wide range in timescales between strong, electromagnetic and weak reactions, the nuclear networks described by equation (3.3) are extraordinarily stiff [20]. For example, the first reaction of the PPI chain in the solar interior, $^1\mathrm{H}(p, e^+\nu)^2\mathrm{H}$, is a weak reaction. As a result, the reaction timescale is as long as billions of years. However, for the second reaction of the PPI chain, $^2\mathrm{H}(p, \gamma)^3\mathrm{He}$, the characteristic timescale is only a few seconds. Thus the timescales for two of the most important reactions for hydrogen burning in the Sun differ by more than 17 orders of magnitude. This extreme stiff nature of the nuclear reaction network has severely limited the usefulness of most techniques developed to solve the initial value problem and requires special treatment in solving the nuclear reaction network equations.

For a full set of nuclear abundances $\vec{Y}$, the time derivatives of the abundances, $\dot{\vec{Y}}$ can be calculated using equation (3.3). The result is the abundance at a future time, $\vec{Y}(t + \Delta t)$, where Δt is the network timestep [20].

$$\vec{Y}(t + \Delta t) = \vec{Y}(t) + \dot{\vec{Y}}(t + \Delta t) * \Delta t \tag{3.6}$$

Solving these fully implicit equations is equivalent to finding the zeros of the set of equations

$$\vec{Z}(t + \Delta t) \equiv \frac{\vec{Y}(t + \Delta t) - \vec{Y}(t)}{\Delta t} - \dot{\vec{Y}}(t + \Delta t) = 0 \tag{3.7}$$

Using the Newton-Raphson method which is based on the Taylor series expansion of $\vec{Z}(t + \Delta t)$ with trial change in abundances given by

$$\Delta\vec{Y} = \left(\frac{\partial\vec{Z}(t+\Delta t)}{\partial\vec{Y}(t+\Delta t)}\right)^{-1}\vec{Z}, \tag{3.8}$$

where $\partial\vec{Z}/\partial\vec{Y}$ is the Jacobian of $\vec{Z}$. Iteration continues until $\vec{Y}(t+\Delta t)$ converges.

Theoretically, every species in the network is connected with every other species through reactions. This leads to a large and dense Jacobian matrix which is computationally expensive to solve. In practice, however, the correlation between nuclear species in the network is significantly limited. For example, because of the repulsive Coulomb barrier, the capture of free neutrons or light charged particles by heavy nuclei occurs much faster than reactions between heavy nuclei. In most cases, there are no more than twelve reactions linking a nucleus with its nuclear neighbors which need to be considered [20]. These reactions are captures of protons, neutrons, alphas or γ's and release of these particles.

Fig. 3.2 demonstrates the sparseness of the Jacobian matrix for a 300 nuclei network for silicon burning [20]. Of the 90000 matrix elements less than 5000 are nonzero. It is doubly bordered, band diagonal, with a border width, ΔB, of 45 and a band diagonal width, ΔD, of 54. But even this sparse form includes about 50000 elements. With solutions of the matrix equations consuming more than 90% of the computational time, it is clearly desirable to develop more efficient methods for solution of a large, sparse and stiff matrix.

As in many disciplines, equilibrium expressions are frequently used to simplify nuclear abundance calculations [20]. Generally when this is the case in nuclear astrophysics, the fast strong and electromagnetic reactions reach equilibrium while weak reactions do not and thus require special caution. Even with this limitation, this so called Nuclear Statistical Equilibrium (NSE) still offers many advantages [20]. First

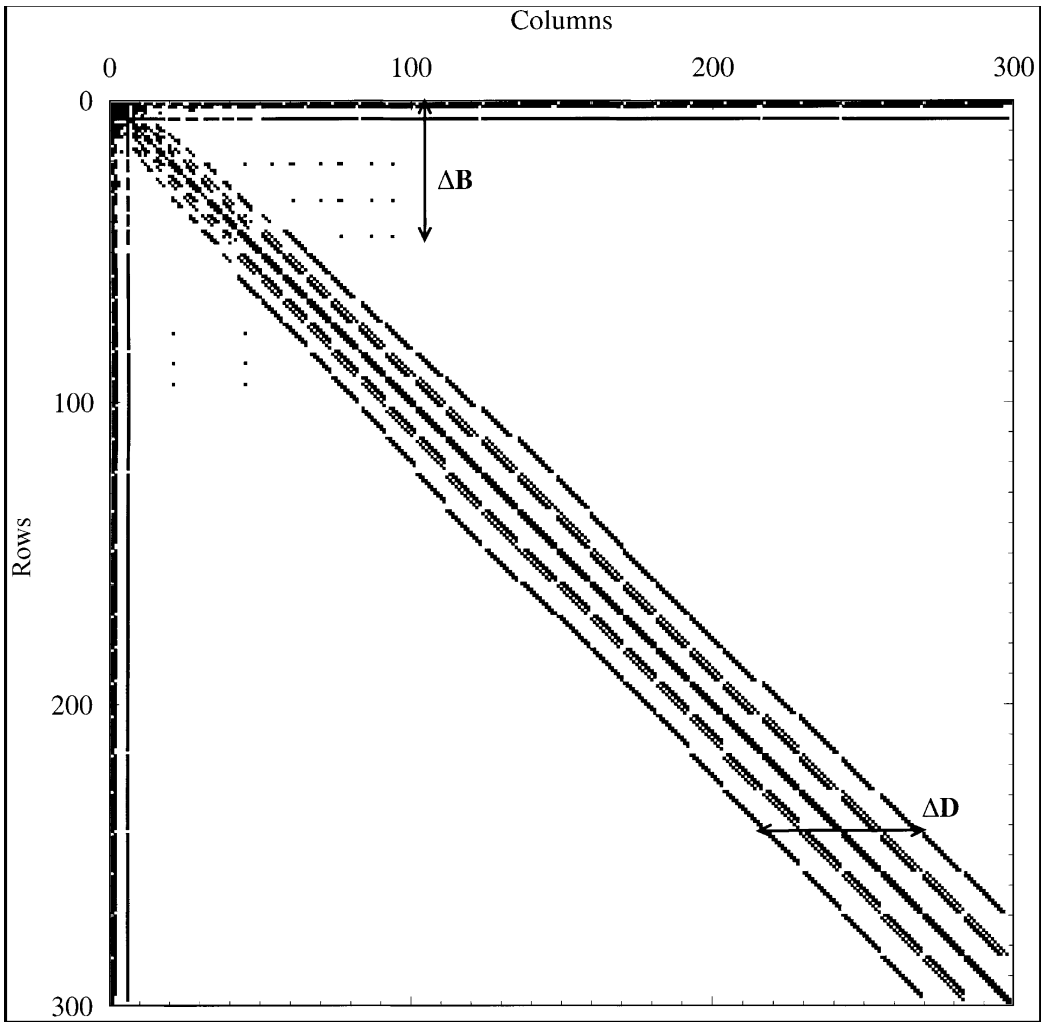

Figure 3.2: Graphic demonstration of the sparseness of the Jacobian matrix. (Hix and Thielemann, J. Comp. and Appl. Math., 109, 321, 1999)

it reduces the number of independent variables and thus greatly reduces the computing cost of nuclear abundance evolution. Secondly it also reduces the memory usage. Finally, the equilibrium abundance calculations depend on binding energies and partition functions, which are better known than many reaction rates, especially in the cases where unstable nuclei are involved, as is generally true in nuclear astrophysics.

Unfortunately there are many serious limitations on the applicability of NSE. It requires a fairly high temperature. Even if the temperature is high enough, it is still problematic when dealing with rapid thermodynamic variations.

Despite the limitations on the applicability of NSE, it is still very attractive because of the reduced computational cost it provides. Techniques are being developed to take advantage of the benefit of NSE [20]. One of such techniques is to use local equilibria to reduce the size of the system where global equilibrium is not achieved but local equilibrium (quasi-equilibrium, or QSE) groups exist. This approach has been demonstrated by Hix and Thielemann [20] where the use of hybrid equilibrium networks was shown to provide sufficient accuracy and considerable reduction in the computational cost.

3.2 Inputs for the Network Calculations

3.2.1 Reaction Rate Library

The reaction library contains all the reaction rate parameters for all the reactions in the network. The REACLIB format reaction rate library was obtained from Thielemann and collaborators [21]. The rate for each reaction is comprised of one or several exponentials. Each exponential contains 7 parameters:

$$
\begin{aligned}
N_A\langle\sigma v\rangle &= exp[a1 + a2/T_9 + a3/T_9^{1/3} + a4 * T_9^{1/3} \\
&\quad + a5 * T_9 + a6 * T_9^{5/3} + a7 * \ln(T_9)] \\
&+ exp[\ldots] + \ldots
\end{aligned} \tag{3.9}
$$

where $N_A\langle\sigma v\rangle$ is the reaction rate discussed in Chapter 2. T_9 is the temperature in 10^9 K. a1, a2 ... a7 are the parameters.

To explore the effect on nucleosynthesis for one specific reaction rate variation, one needs to increase or decrease the rate by some factor, say η, then the rate must be changed as follows:

$$
\begin{aligned}
\eta * N_A\langle\sigma v\rangle &= \eta \cdot exp[a1 + a2/T_9 + a3/T_9^{1/3} + a4 * T_9^{1/3} \\
&\quad + a5 * T_9 + a6 * T_9^{5/3} + a7 * \ln(T_9)] \\
&= exp[(a1 + \ln(\eta)) + a2/T_9 + \ldots]
\end{aligned} \tag{3.10}
$$

So the rate variation only affects the parameter $a1$ by $a1 \rightarrow a1 + \ln(\eta)$.

Using Eq. (2.25) and Eq. (2.26), it is straightforward that the reverse reaction rate should undergo a similar transform.

3.2.2 Hydrodynamic Trajectories

Hydrodynamic trajectories give the temperature and density within each zone of the nova envelope as a function of time. These hydrodynamic trajectories are coupled with the nuclear reaction network during the evolution of the star. The interval between time steps is based on the size of changes in abundances in the previous

step. The time step size becomes smaller as the nova progresses toward the peak intensity of outburst. To compare with observations, we chose to stop the calculation at 1 hour after the outburst.

Fig. 3.3, 3.4 and 3.5 show plots of the hydrodynamic trajectories for the 1.00 $M_\odot$ CO white dwarf nova, 1.25 $M_\odot$ ONe WD nova and the 1.35 $M_\odot$ ONe WD nova. The highest temperatures and densities are achieved in the 1.35 $M_\odot$ WD nova, followed by the 1.25 $M_\odot$ and the 1.00 $M_\odot$ novae. However the 1.35 $M_\odot$ WD nova also cools off faster than the 1.25 $M_\odot$ and the 1.00 $M_\odot$ novae because the nova outburst on 1.35 $M_\odot$ WD is much faster and more violent than on the 1.25 $M_\odot$ and the 1.00 $M_\odot$ white dwarfs.

3.2.3 Initial Abundances

The initial abundances for the network calculations were adopted from Politano et al. [22] for the 1.25 $M_\odot$ and the 1.35 $M_\odot$ ONe white dwarf nova. They assumed mixing of the accreted material with matter from the underlying white dwarf occurs, such that the composition of the accreted material is enriched in oxygen, neon, and magnesium nuclei to approximately 50% by mass. For the 1.00 $M_\odot$ CO WD nova, The initial composition was 50% solar [23] by mass and 50% products of He burning, which is an equal mix of ^{12}C and ^{16}O with a trace of ^{22}Ne. The initial abundances used in our calculations are listed in Table 3.1.

3.2.4 Zone Masses

As stated previously, our multi-zone simulation runs on each zone separately. To achieve a composite abundance pattern for all the ejected zones in a nova outburst,

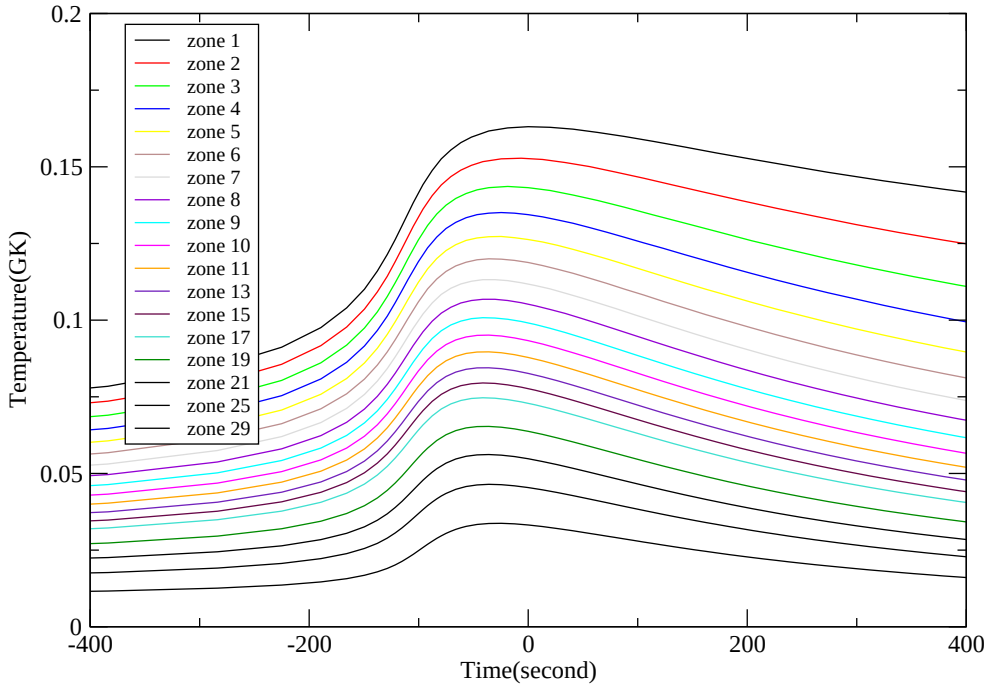

(a)

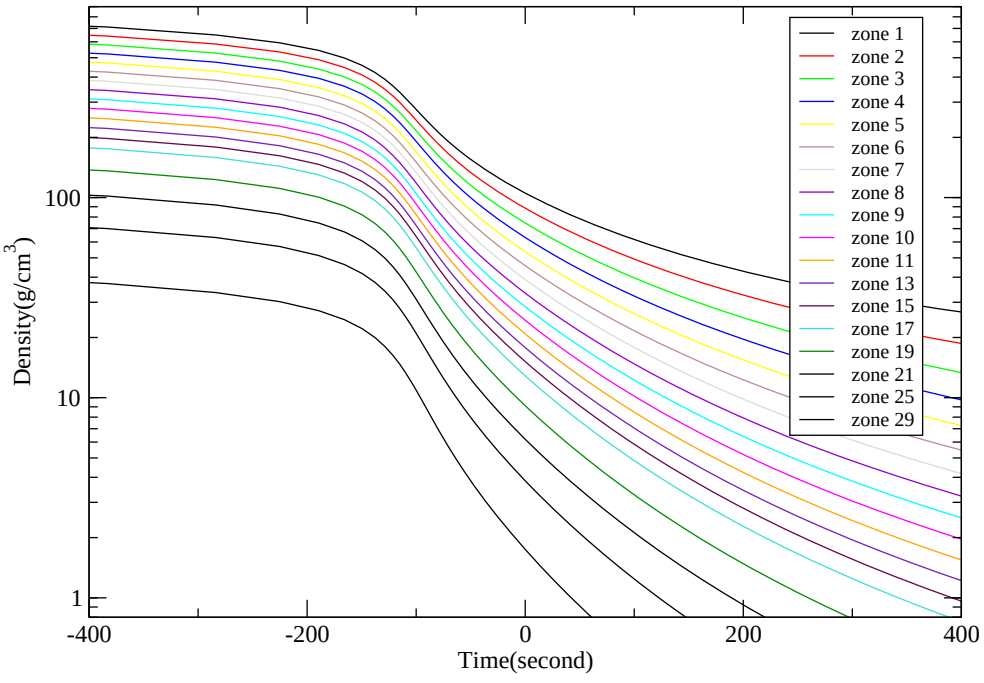

(b)

Figure 3.3: Thermodynamic Trajectory for 1.00 $M_{\odot}$ CO WD nova.

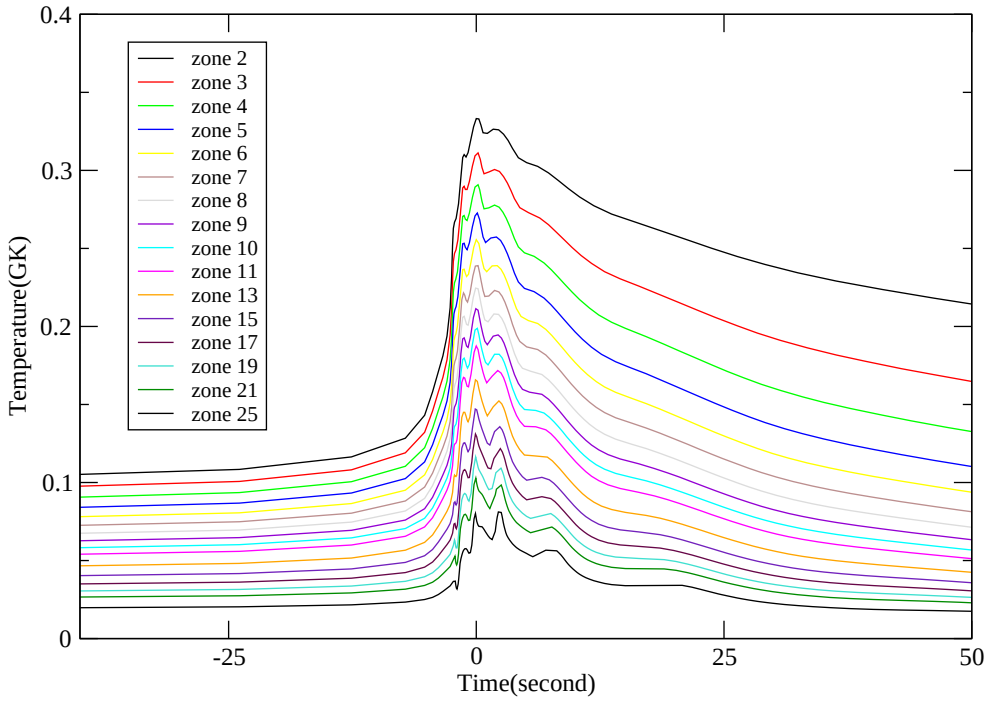

(a)

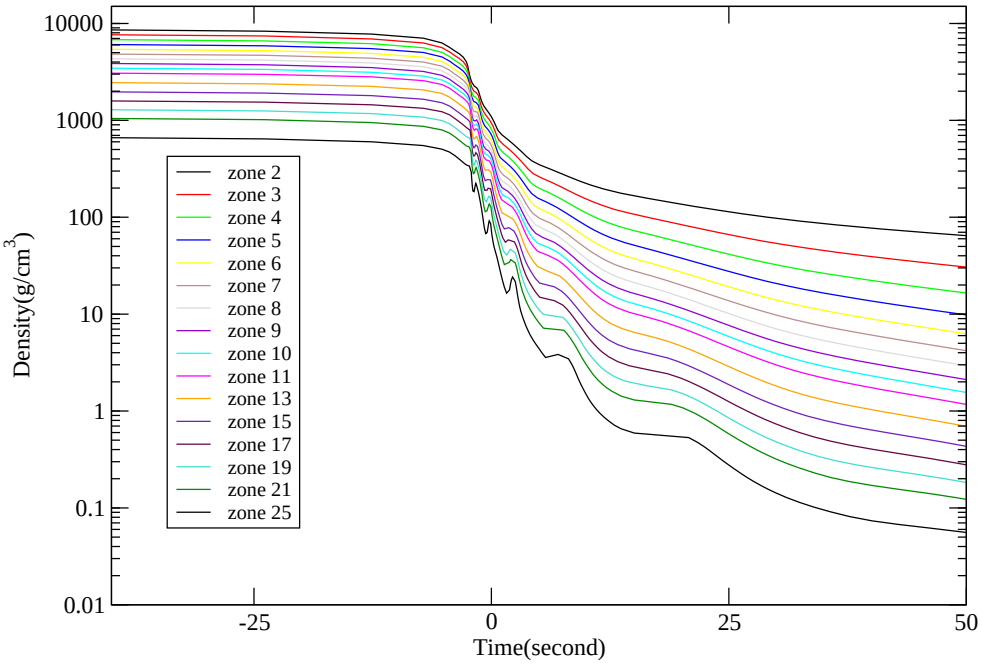

(b)

Figure 3.4: Thermodynamic Trajectory for 1.25 $M_{\odot}$ ONe WD nova.

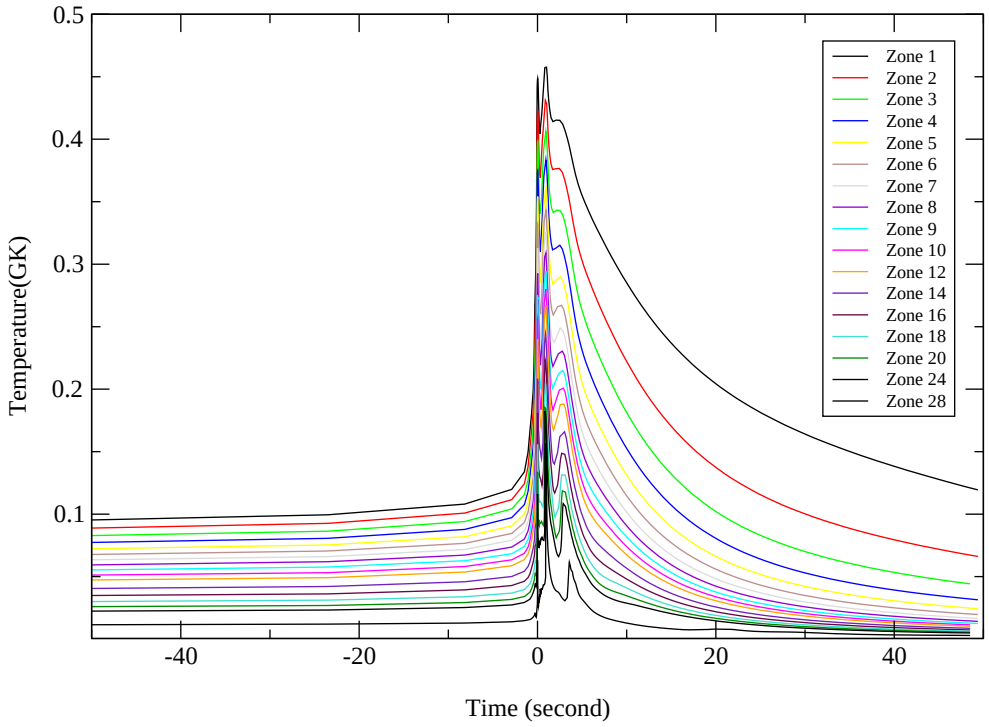

(a)

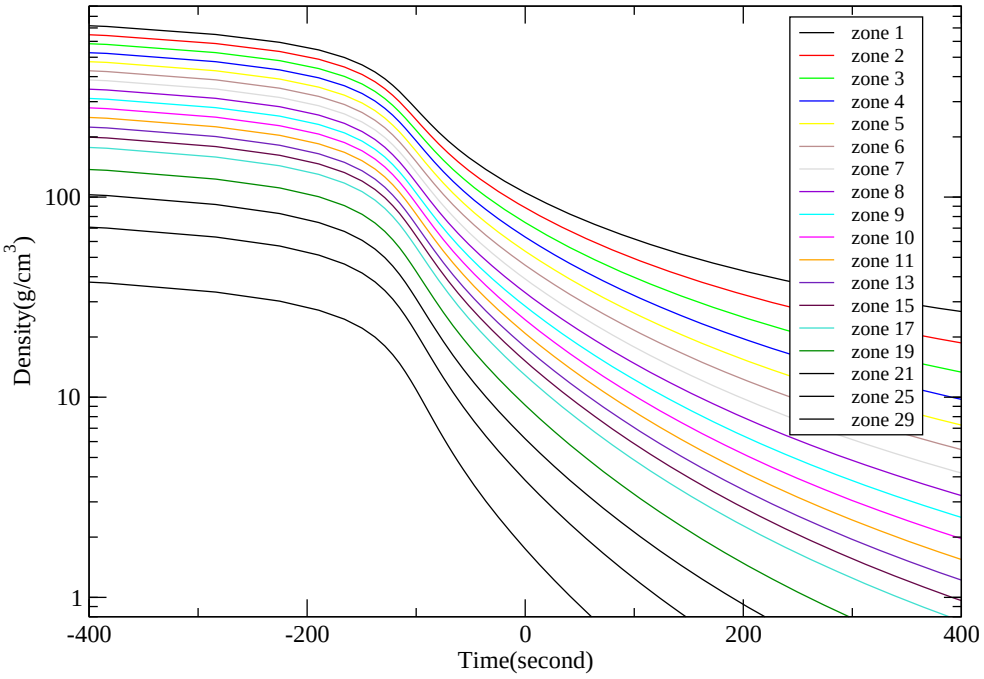

(b)

Figure 3.5: Thermodynamic Trajectory for 1.35 $M_{\odot}$ ONe WD nova.

Table 3.1: Initial abundances (taken from model [22]. in units of mole/gram) for 1.00, 1.25 and 1.35 $M_\odot$ WD nova. Isotopes not listed have zero initial abundances.

Nucleus	1.25 & 1.35 $M_\odot$ ONe WD nova	1.00 $M_\odot$ CO WD nova
p	3.6500E-01	3.5346E-01
d	0	1.2015E-05
He3	1.9317E-06	4.8897E-06
He4	3.3250E-02	3.4420E-02
Li6	0	5.4237E-11
Li7	0	6.6873E-10
Be9	0	9.2343E-12
B10	0	5.3570E-11
B11	0	2.1528E-10
C12	7.8673E-05	2.0501E-02
C13	8.8507E-07	1.4056E-06
N14	1.6577E-07	3.9337E-05
N15	6.0832E-08	1.4552E-07
O16	9.3975E-03	1.5581E-02
O17	5.0154E-08	1.1456E-07
O18	2.6973E-07	6.0356E-07
F19	5.9215E-09	1.0671E-08
Ne20	1.2441E-02	4.0553E-05
Ne21	4.2849E-08	9.8462E-08
Ne22	1.2854E-06	5.0295E-04
Na23	4.0039E-07	7.2703E-07
Mg24	4.1708E-03	1.0743E-05
Mg25	7.5163E-07	1.3557E-06
Mg26	8.2888E-07	1.4942E-06
Al27	5.9637E-07	1.0754E-06
Si28	6.4764E-06	1.1676E-05
Si29	3.2804E-07	5.9215E-07
Si30	2.1775E-07	3.9218E-07
P31	7.3054E-08	1.3178E-07

Continued on Next Page...

Table 3.1 – Continued

Nucleus	1.25 & 1.35 $M_\odot$ ONe WD nova	1.00 $M_\odot$ CO WD nova
S32	3.4350E-06	6.1956E-06
S33	2.7114E-08	4.8851E-08
S34	1.5243E-07	2.7536E-07
S36	0	1.3044E-09
Cl35	2.7887E-08	3.6190E-08
Cl37	8.9210E-09	1.1555E-08
Ar36	5.3244E-07	1.0764E-06
Ar38	9.9750E-08	2.0289E-07
Ar40	0	3.1666E-10
K39	2.4698E-08	4.4545E-08
K40	0	6.9340E-11
K41	0	3.2115E-09
Ca40	4.1585E-07	7.4973E-07
Ca42	0	5.0065E-09
Ca43	0	1.0443E-09
Ca44	0	1.6157E-08
Ca46	0	3.0365E-11
Ca48	0	1.4393E-09
Sc45	0	4.3278E-10
Ti46	0	2.4270E-09
Ti47	0	2.2156E-09
Ti48	0	2.2425E-08
Ti49	0	1.6756E-09
Ti50	0	1.6421E-09
V50	0	9.2721E-12
V51	0	3.7009E-09
Cr50	0	7.4297E-09
Cr52	0	1.4345E-07
Cr53	0	1.6247E-08
Cr54	0	4.0423E-09

we need to do a weighted addition of the abundances produced by each zone for each isotope. Starrfield et al. [24] had calculated the mass for each zone. The weighting factor for each zone then is given by $W_i = m_i / \sum m_i$, where m_i is the mass for the i-th zone. Table 3.2 lists the masses for each ejected zone of the nova envelope.

3.3 Effects of the ^{30}P(p,γ)^{31}S rate variation on nova nucleosynthesis

To demonstrate the importance of the ^{30}P(p,γ)^{31}S reaction rate and explore the effects of the ^{30}P(p,γ)^{31}S rate variation on nova nucleosynthesis, we have varied the adopted rate which is based on a Hauser-Feshbach calculation [36] by factors 100 and 10 up and down following the procedure described in Chapter 2, and performed multi-zone network calculations using these rates on a 1.35 and a 1.25 $M_\odot$ ONe WD nova, and a 1.00 $M_\odot$ CO WD nova, respectively.

We begin with the 1.35 $M_\odot$ ONe WD nova. As discussed in Chapter 1, nova outbursts on more massive white dwarfs result in more violent explosions. Thus the 1.35 $M_\odot$ WD nova reaches higher temperature ($\sim$0.44 GK), about 0.1 GK higher than a 1.25 $M_\odot$ WD nova's peak temperature, and the envelope expands faster and cools faster than a less massive nova.

Fig. 3.6 are plots of the ratios of mass fractions produced by the network calculations with varied ^{30}P(p,γ)^{31}S rates reduced by a factor of 100 and 10, respectively, to the mass fractions produced with the nominal rate. In the upper plot of Fig. 3.6 where the ^{30}P(p,γ)^{31}S rate is reduced by a factor of 100, significant changes in the abundances of isotopes in the Si-Ca mass region occur. The production of heavier elements are dramatically hindered. The mass fractions of isotopes like ^{31,32}P, $^{32-35}$S,

Table 3.2: Zone masses for the nova envelope [22, 24].

zone #	1.00 $M_\odot$ CO WD nova	1.25 $M_\odot$ ONe WD nova	1.35 $M_\odot$ ONe WD nova
1	1.13544E+28	1.82374E+28	1.05625E+28
2	9.78826E+27	1.53255E+28	8.87605E+27
3	8.43815E+27	1.28786E+28	7.45887E+27
4	7.27427E+27	1.08223E+28	6.26796E+27
5	6.93274E+27	9.09440E+27	5.26719E+27
6	5.97650E+27	7.64236E+27	4.42621E+27
7	5.15215E+27	6.42215E+27	3.71950E+27
8	4.44151E+27	5.39676E+27	3.12563E+27
9	3.82889E+27	4.53510E+27	2.62658E+27
10	3.30077E+27	3.81101E+27	2.20721E+27
11	2.84549E+27	3.20252E+27	1.85480E+27
12	2.45301E+27	2.69120E+27	1.55866E+27
13	2.11466E+27	2.26151E+27	1.30980E+27
14	1.82298E+27	1.90043E+27	1.10067E+27
15	1.57154E+27	1.59700E+27	9.24931E+26
16	1.35477E+27	1.34202E+27	7.77253E+26
17	1.16791E+27	1.12774E+27	6.53154E+26
18	1.00682E+27	9.47685E+26	5.48869E+26
19	8.67946E+26	7.96374E+26	4.61234E+26
20	7.48229E+26	6.69221E+26	3.87592E+26
21	6.45025E+26	5.62371E+26	3.25707E+26
22	5.56056E+26	4.72581E+26	2.73704E+26
23	4.79359E+26	3.97127E+26	2.30003E+26
24	4.13240E+26	3.33720E+26	1.93280E+26
25	3.56242E+26	2.80437E+26	1.62420E+26
26	3.07105E+26	2.35661E+26	1.36487E+26
27	2.64746E+26	1.98035E+26	1.14695E+26
28	2.64746E+26	1.66416E+26	9.63827E+25

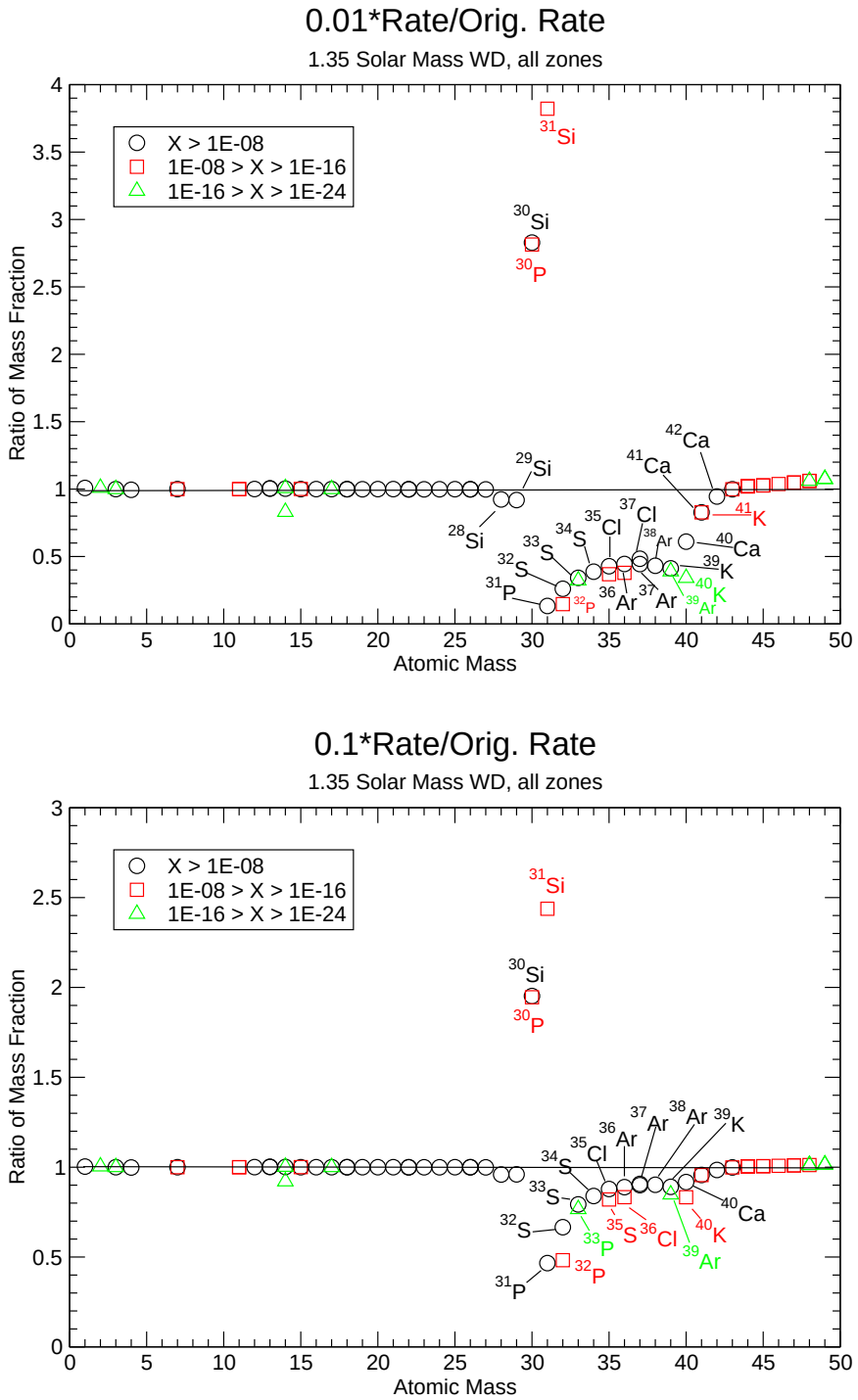

Figure 3.6: The ratio of abundances (mass fraction) from varied ^{30}P(p,γ)^{31}S rates to those obtained with the nominal rate for a 1.35 M$_\odot$ WD nova. The upper figure is for the case that the ^{30}P(p,γ)^{31}S is reduced by a factor of 100, the lower figure is for the case that the ^{30}P(p,γ)^{31}S rate is reduced by a factor of 10.

$^{35-37}$Cl, $^{36-39}$Ar, $^{39-40}$K and ^{40}Ca are reduced by a factor as much as 10. Abundances of isotopes like ^{30,31}Si and ^{30}P are increased by a factor of ~ 3. The important enhancement of ^{30}Si, coming from the ^{30}P β^+ decay, is due to the fact that at this ^{30}P(p,γ)^{31}S rate, the β^+ decay competes favorably with proton captures.

The reduction of the ^{30}P(p,γ)^{31}S rate by a factor of 10 results in abundance pattern changes that are qualitatively similar to those in the factor of 100 reduction case (see lower panel of Fig. 3.6), but reduced in magnitude.

Fig. 3.7 shows the resulting abundance patterns where the ^{30}P(p,γ)^{31}S rate are increased by 100 and 10, respectively. This increase affects only the ^{30}Si yield significantly, since the path from ^{30}P to ^{31}S is favored (which in turn, accounts for the moderate increase of ^{31}P in the ejecta) over the decay to ^{30}Si. However, the impact on other nuclear species is very limited.

Fig. 3.8 and 3.9 contains plots similar to Fig. 3.6 and 3.7 for a 1.25 $M_\odot$ ONe WD nova. The reduction of the ^{30}P(p,γ)^{31}S rate yields similar results as for the 1.35 $M_\odot$ WD nova case with even larger decreases in the abundances of isotopes in the Si-Ca mass region (see Fig. 3.8). When the ^{30}P(p,γ)^{31}S rate is increased (Fig. 3.9), more than 10 isotopes in the Si-Ca mass region exhibit a noticeably moderate abundance enhancement ($\sim 20\%$).

Fig. 3.10 and 3.11 give the results for a 1.00 $M_\odot$ CO WD nova. As expected, since this CO white dwarf nova lacks the seed nuclei of Ne and Mg isotopes, there is little nuclear processing to the heavier Si-Ca mass region. Therefore the effect of the ^{30}P(p,γ)^{31}S rate variation on a CO white dwarf nova nucleosynthesis is negligible.

Our network calculations confirm previous studies by other groups ([26,28]) showing the crucial role of the ^{30}P(p,γ)^{31}S reaction rate on nucleosynthesis in nova outbursts on ONe white dwarfs, especially the synthesis of heavier elements in the Si-Ca mass region.

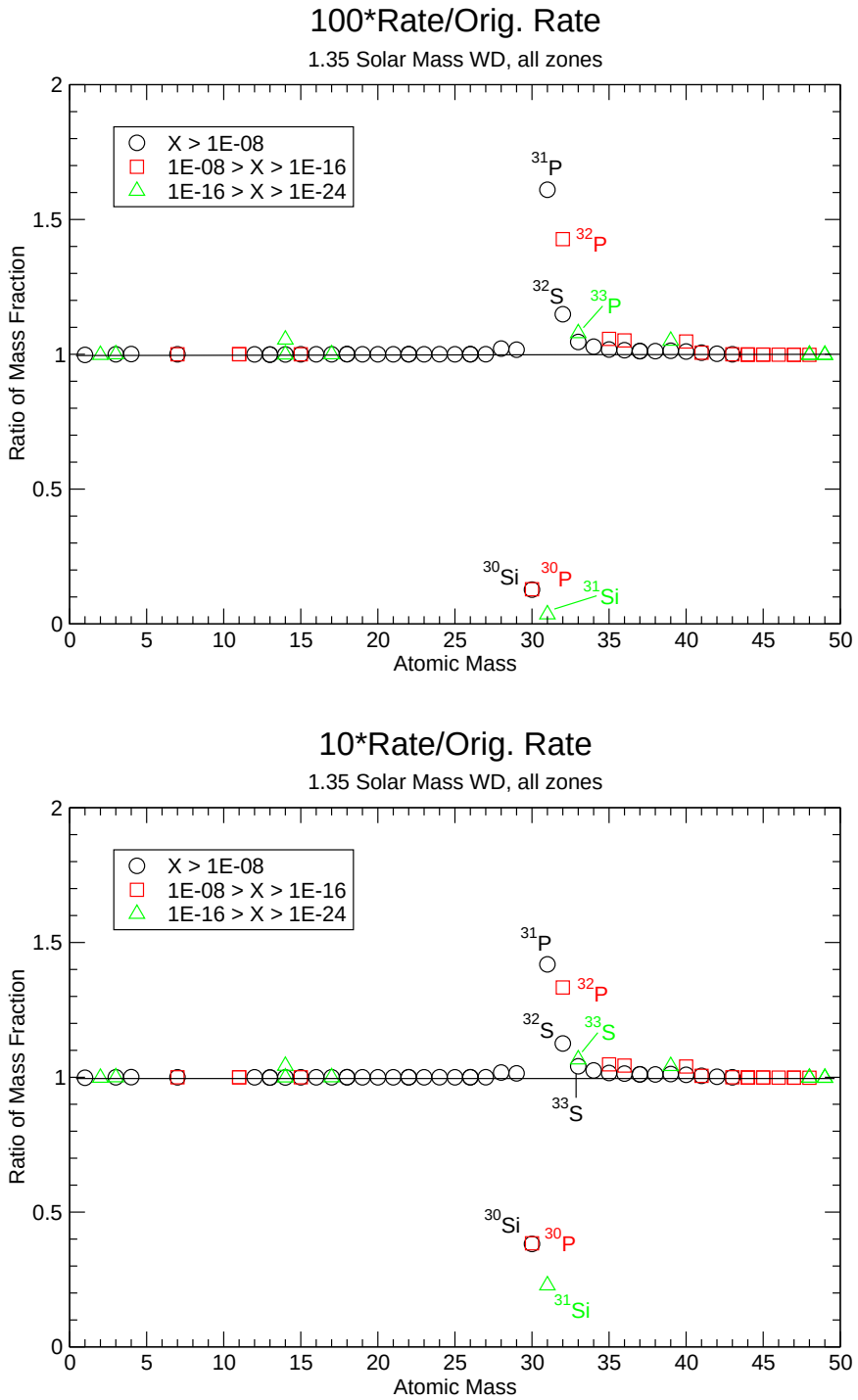

Figure 3.7: The ratio of abundances (mass fraction) from varied ^{30}P(p,γ)^{31}S rates to those obtained with the nominal rate for a 1.35 M$_\odot$ WD nova. The upper figure is for the case that the ^{30}P(p,γ)^{31}S is increased by a factor of 100, the lower figure is for the case that the ^{30}P(p,γ)^{31}S rate is increased by a factor of 10.

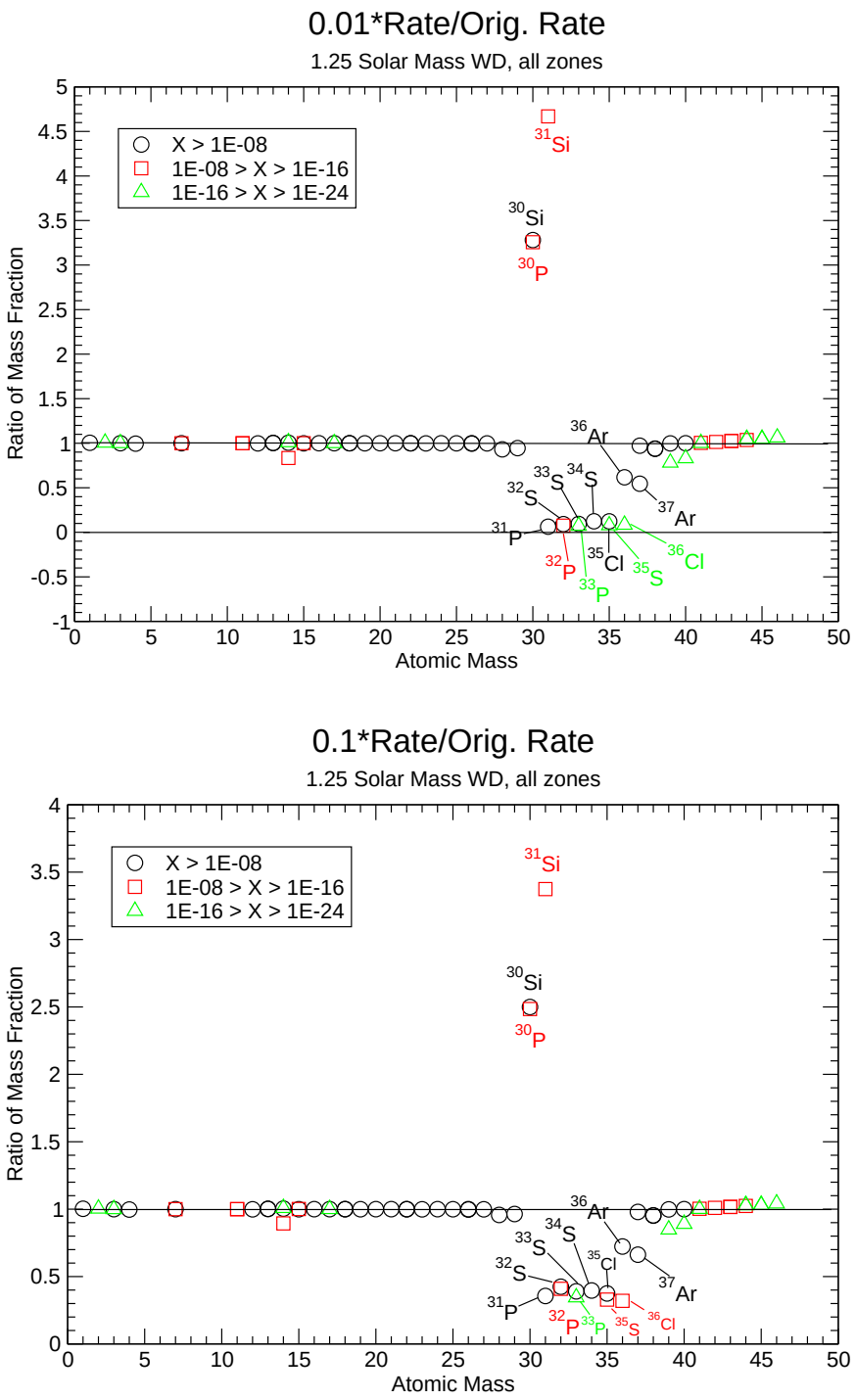

Figure 3.8: The ratio of abundances (mass fraction) from varied ^{30}P(p,γ)^{31}S rates to those obtained with the nominal rate for a 1.25 M$_\odot$ WD nova. The upper figure is for the case that the ^{30}P(p,γ)^{31}S is reduced by a factor of 100, the lower figure is for the case that the ^{30}P(p,γ)^{31}S rate is reduced by a factor of 10.

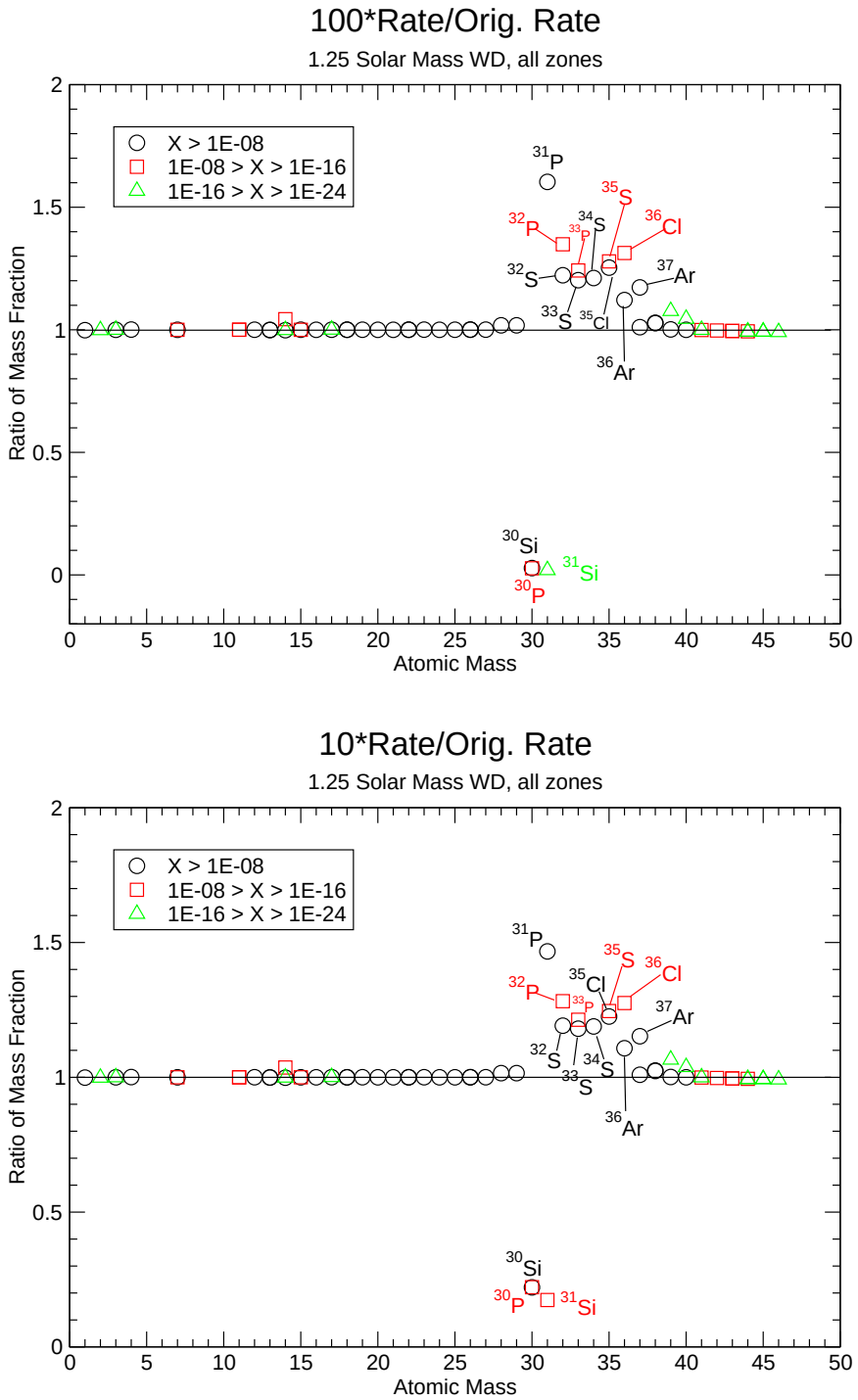

Figure 3.9: The ratio of abundances (mass fraction) from varied ^{30}P(p,γ)^{31}S rates to those obtained with the nominal rate for a 1.25 M$_\odot$ WD nova. The upper figure is for the case that the ^{30}P(p,γ)^{31}S is increased by a factor of 100, the lower figure is for the case that the ^{30}P(p,γ)^{31}S rate is increased by a factor of 10.

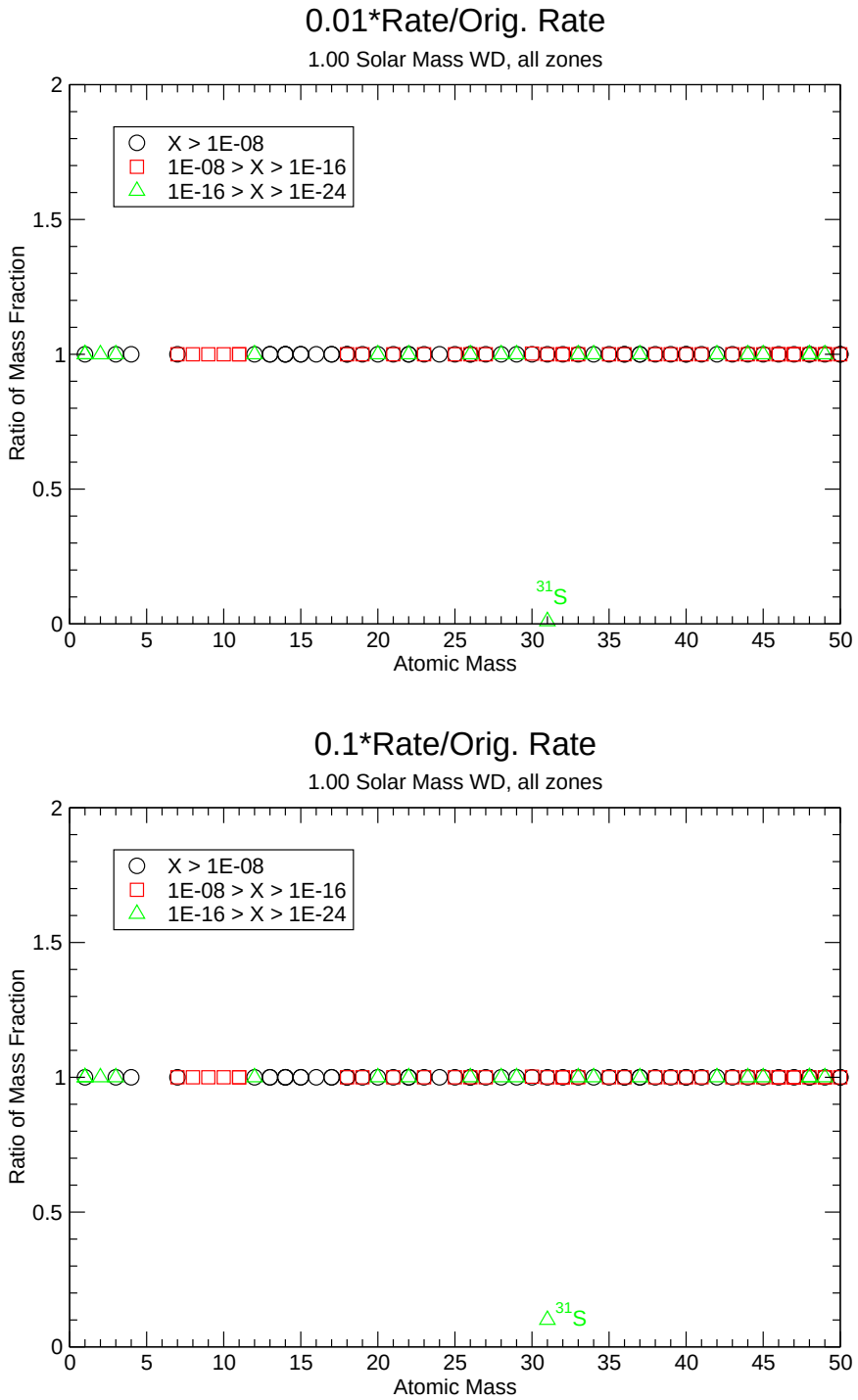

Figure 3.10: The ratio of abundances (mass fraction) from varied ^{30}P(p,γ)^{31}S rates to those obtained with the nominal rate for a 1.00 M$_\odot$ WD nova. The upper figure is for the case that the ^{30}P(p,γ)^{31}S is reduced by a factor of 100, the lower figure is for the case that the ^{30}P(p,γ)^{31}S rate is reduced by a factor of 10.

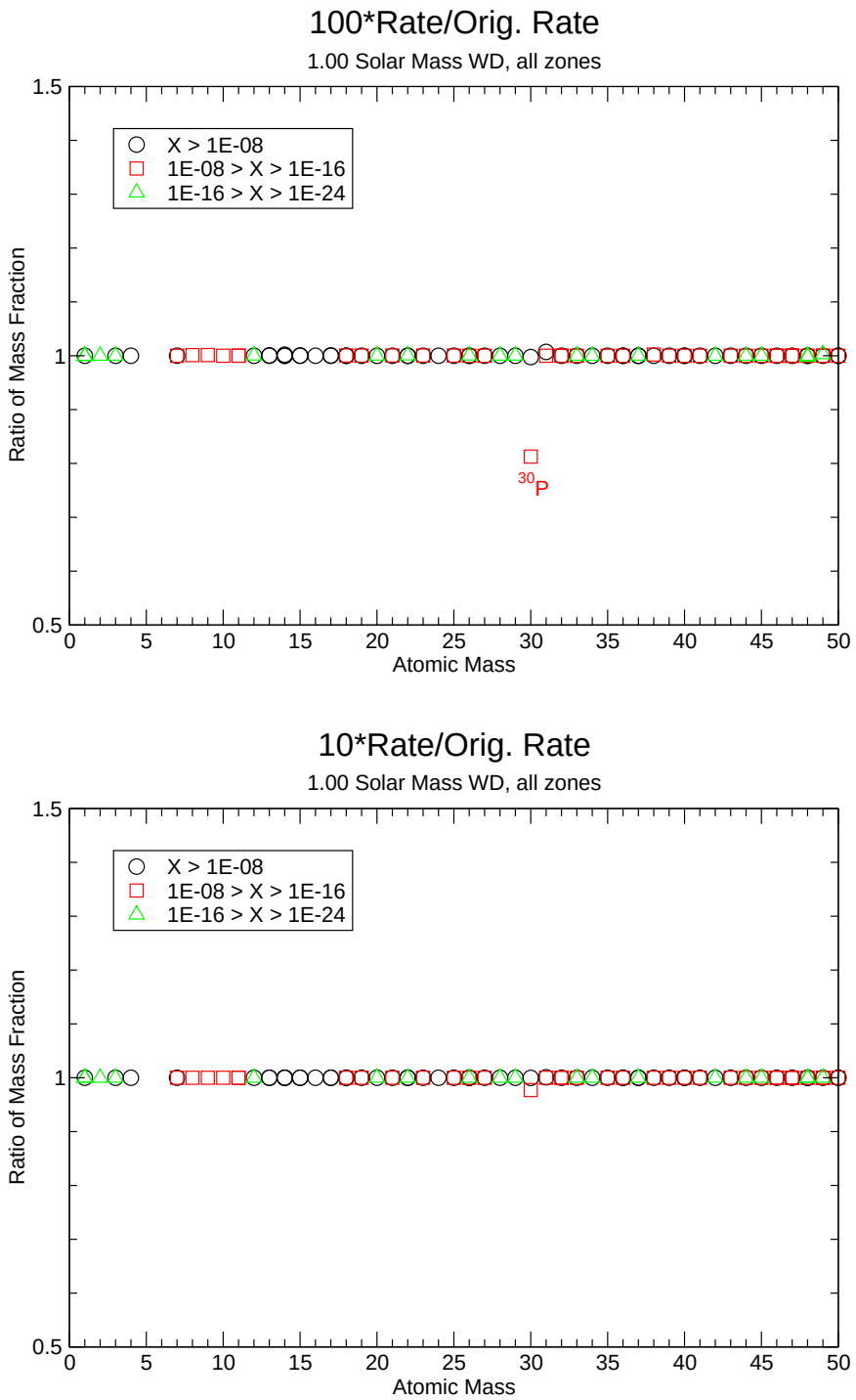

Figure 3.11: The ratio of abundances (mass fraction) from varied ^{30}P(p,γ)^{31}S rates to those obtained with the nominal rate for a 1.35 $M_{\odot}$ WD nova. The upper figure is for the case that the ^{30}P(p,γ)^{31}S is increased by a factor of 100, the lower figure is for the case that the ^{30}P(p,γ)^{31}S rate is increased by a factor of 10.

Chapter 4

The ^{32}S(p,d)^{31}S Measurement

4.1 Beam Production – The HRIBF

The proton beam used in the present experiment is provided by the tandem accelerator at the ORNL Holifield Radioactive Ion Beam Facility [30] (HRIBF, Fig. 4.1). The tandem accelerator [30] (see Fig. 4.2 and 4.3) consists of 27 conducting units, a 180 degree bending magnet, high and low energy acceleration tubes, three sets of steerers, two charge strippers, and three quadrupole magnets. The acceleration column is placed in a 100 ft high, 33 ft wide vessel filled with SF_6 gas to prevent sparking of the tandem with the steel walls of the vessel during operation. Each of the conducting units can withstand one million volts, the total voltage the high voltage terminal can reach is 25 million volts, the highest among electrostatic accelerators in the world.

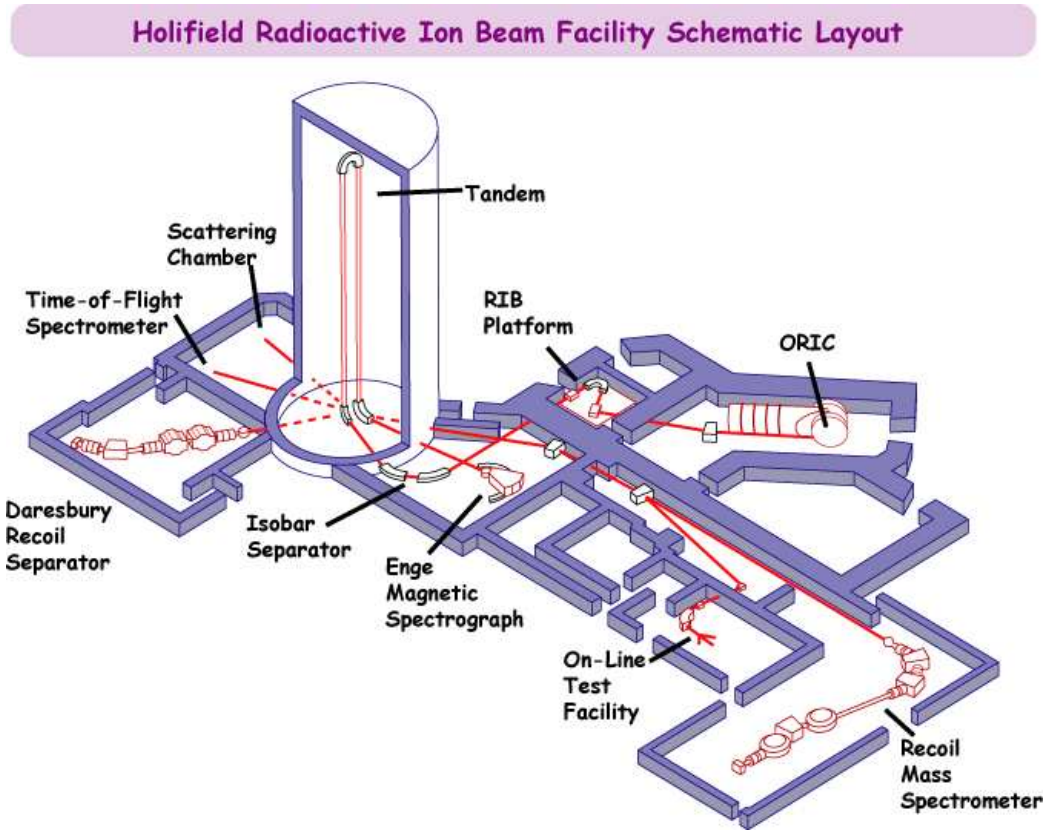

Figure 4.1: A schematic layout of the Holifield Radioactive Ion Beam Facility at Oak Ridge National Laboratory (http://www.phy.ornl.gov/hribf).

Figure 4.2: A bottom view of the 25 MV tandem electrostatic accelerator.

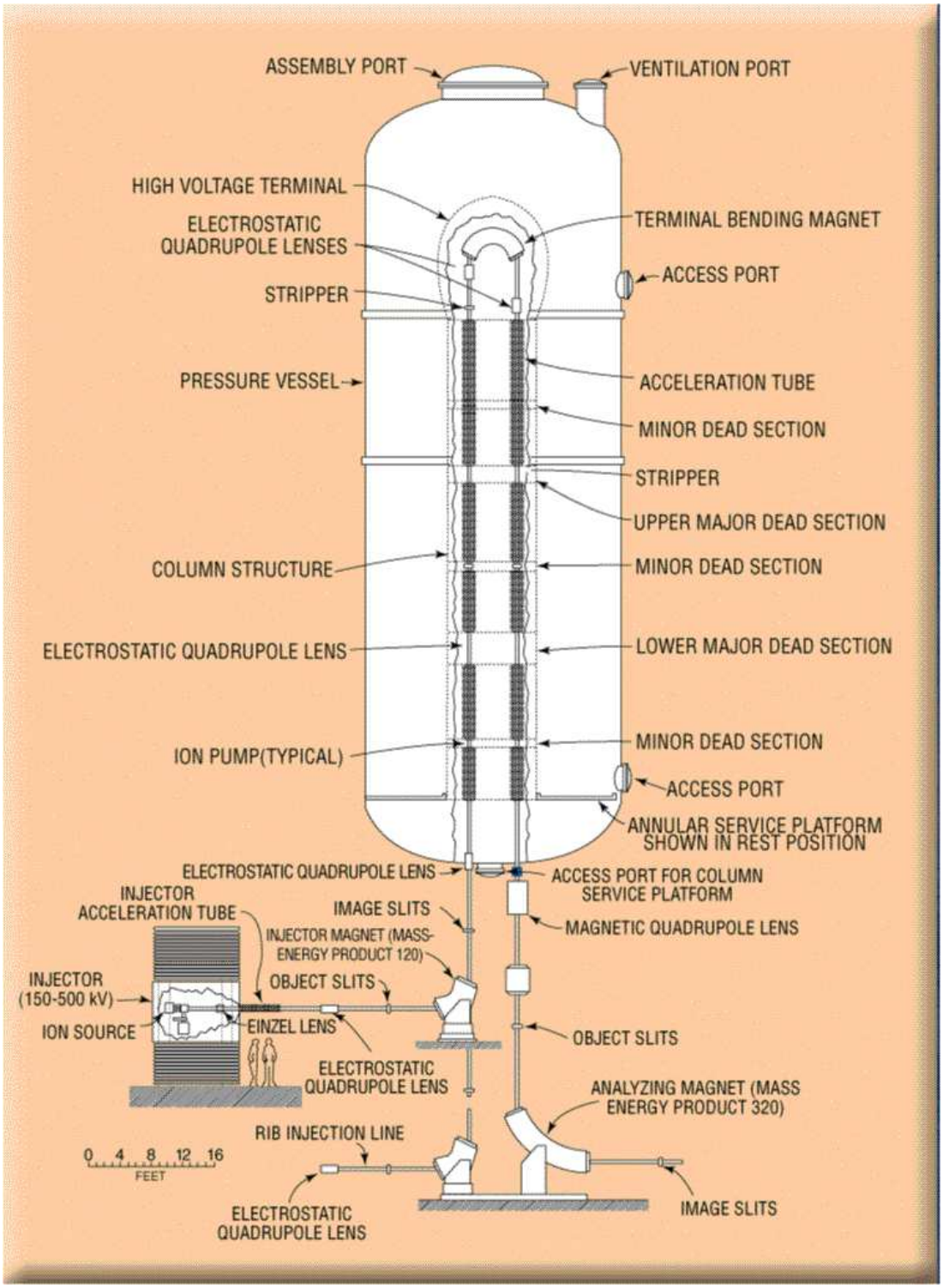

Figure 4.3: A Diagram of the 25 MV tandem electrostatic accelerator

4.2 Reaction Products Detection – The Silicon Detector Array

An array of silicon detectors was used to detect the deuterons from the ^{32}S(p,d)^{31}S reaction. The silicon detector array (SIDAR) [38, 39] is comprised of 8 individual sectors. Each sector is an independent detector which is segmented into 16 radial strips which allows for the extraction of angular distribution information. Pictures of the sidar are shown in figures 4.4 and 4.5 [29]. The SIDAR has the advantage of large solid angle coverage, excellent energy resolution and high segmentation which allows for higher counting rate without pileup than one could have with a single large area detector.

Each of the SIDAR strips is connected to an individual preamplifier chip in a larger preamplifier module (Fig. 4.6). The preamplifier module is a very compact design ideal for strip detector applications. The signals from the preamplifiers are fed into the shaping amplifiers. The amplifiers produce both linear and logic signals. The linear signals go directly to the ADCs while the logic signals are used to generate a common gate signal for the ADCs. The analog-to-digital conversion of the pulse heights was performed by LeCroy-3351 peak-sensing ADCs, the digital signals were then sent to computer for analysis. The logic diagram for the SIDAR electronics is shown in Fig. 4.7.

The strips of this detector system were gain matched with a ^{241}Am α-source [29]. The energies of the three α groups are 5.486 MeV (85.2 %), 5.443 MeV (12.8 %) and 5.388 MeV (1.4 %). A spectrum from one of the strips is shown in Figure 4.8 [29]. The three alpha groups were clearly resolved, and the full-width at half-maximum (FWHM) was 28 keV. This sets an upper limit on the SIDAR energy resolution of 28 keV.

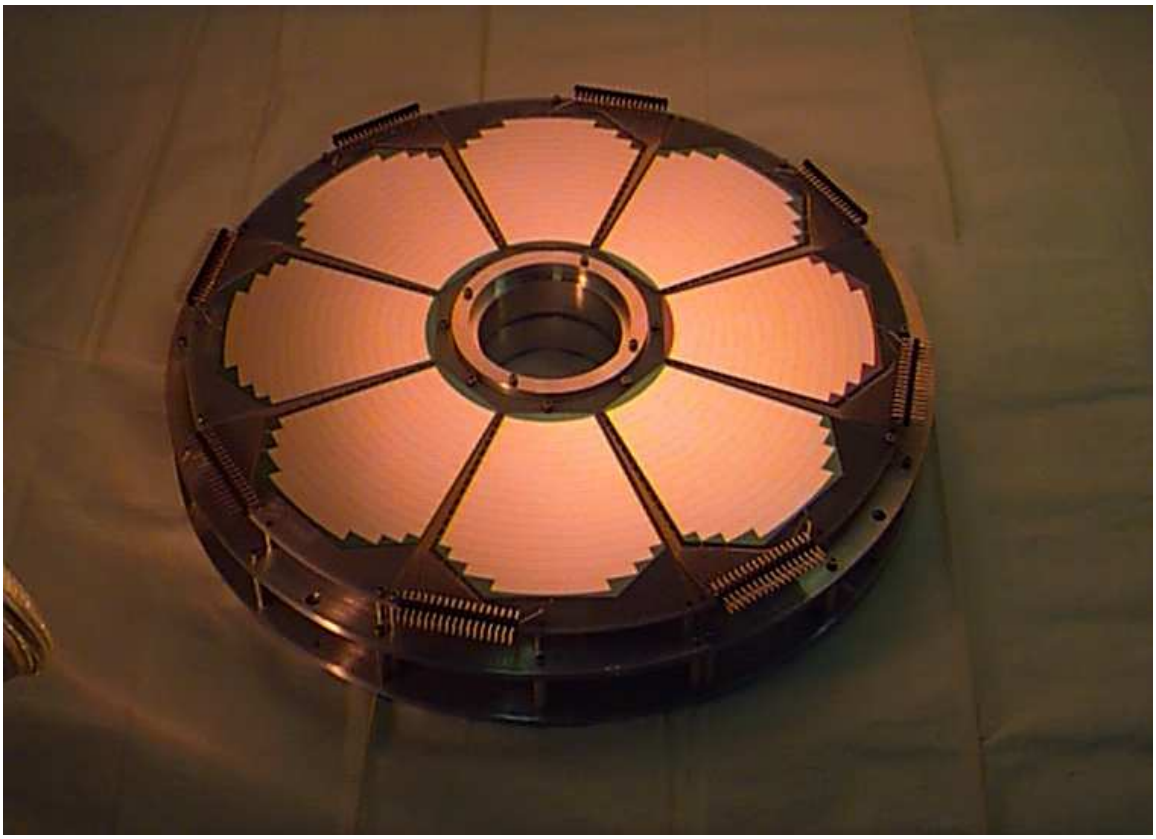

Figure 4.4: A picture of the SIDAR [29]. The SIDAR consists of 8 azimuthal sectors, each sector is segmented into 16 strips.

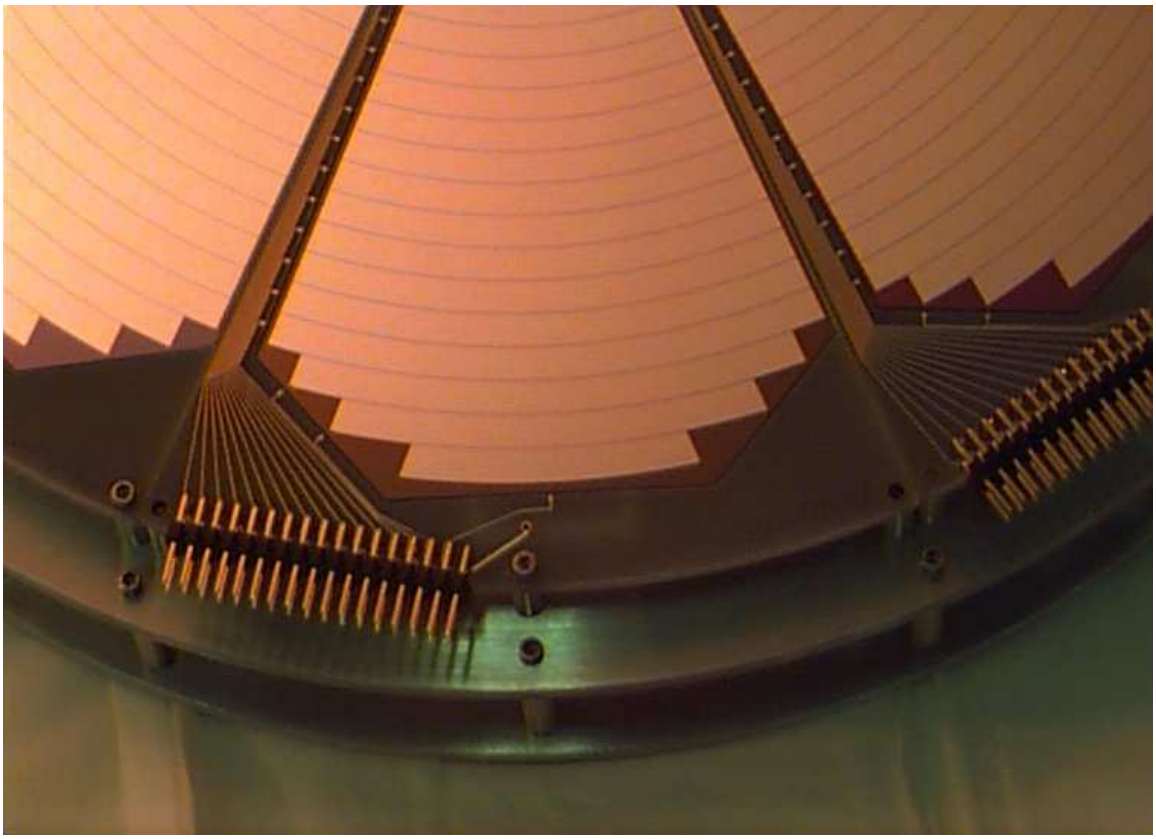

Figure 4.5: A close-up of the SIDAR strips [29].

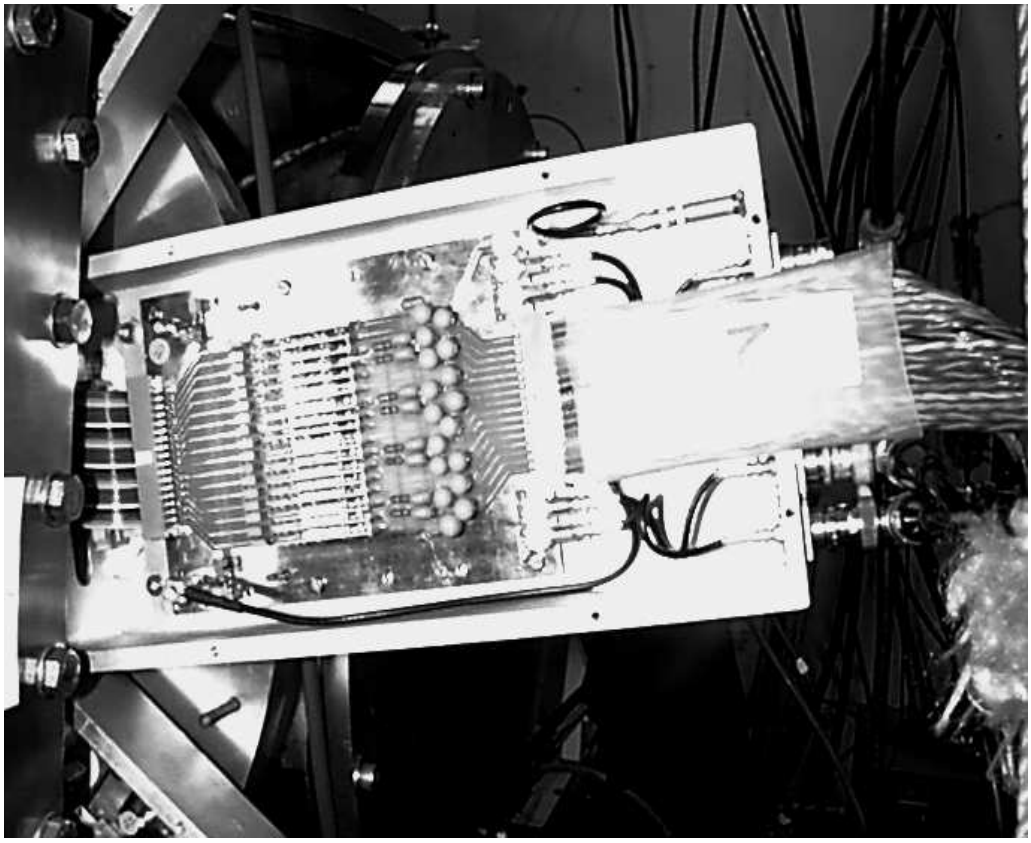

Figure 4.6: A preamplifier unit used in the experiment. Each preamplifier unit holds up to 16 individual channels.

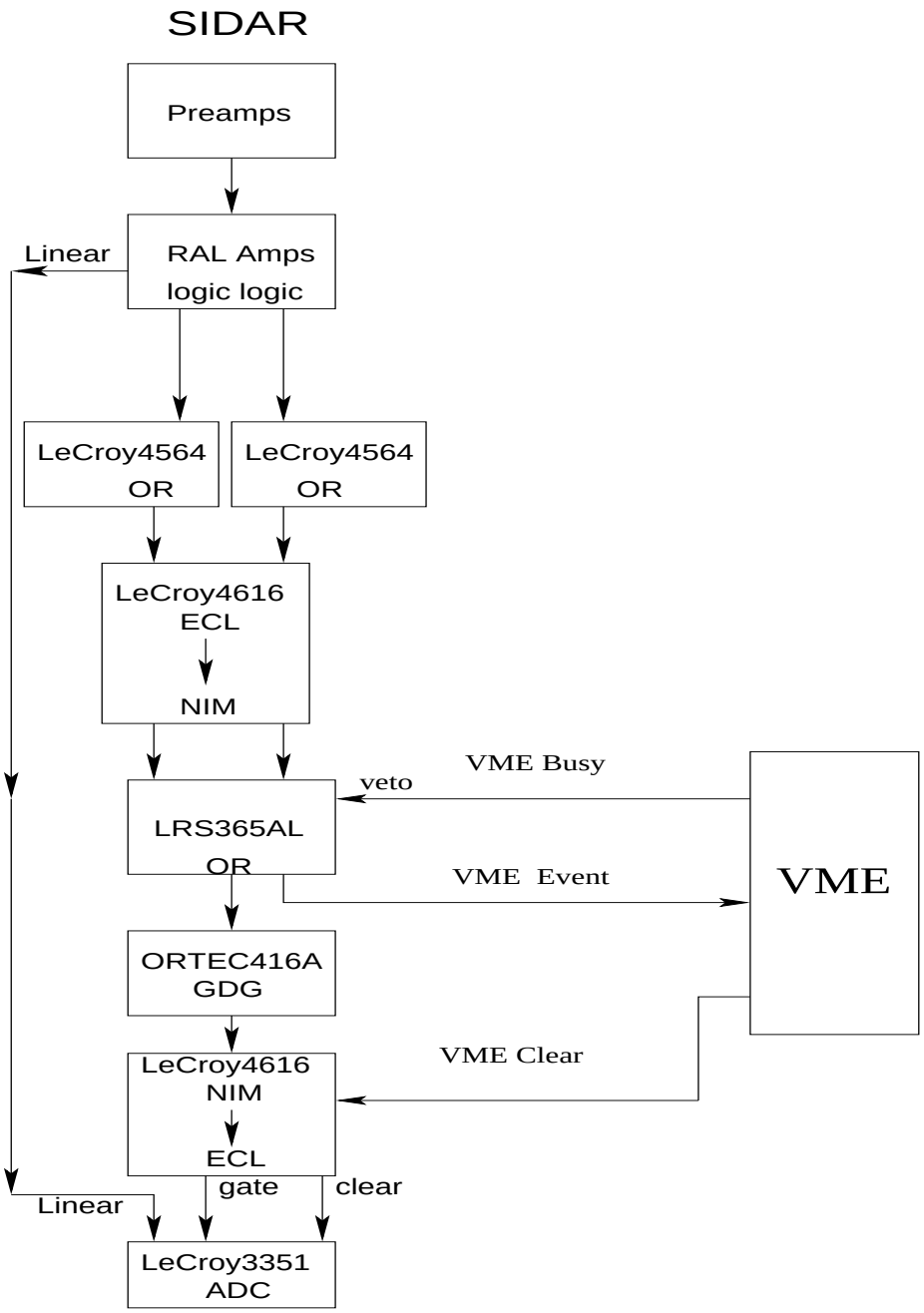

Figure 4.7: The logic diagram for the SIDAR electronics is shown. The amplifiers produce both linear and logic signals. The linear outputs are sent to the ADCs while the logic outputs are used to generate gate signals for the ADCs.

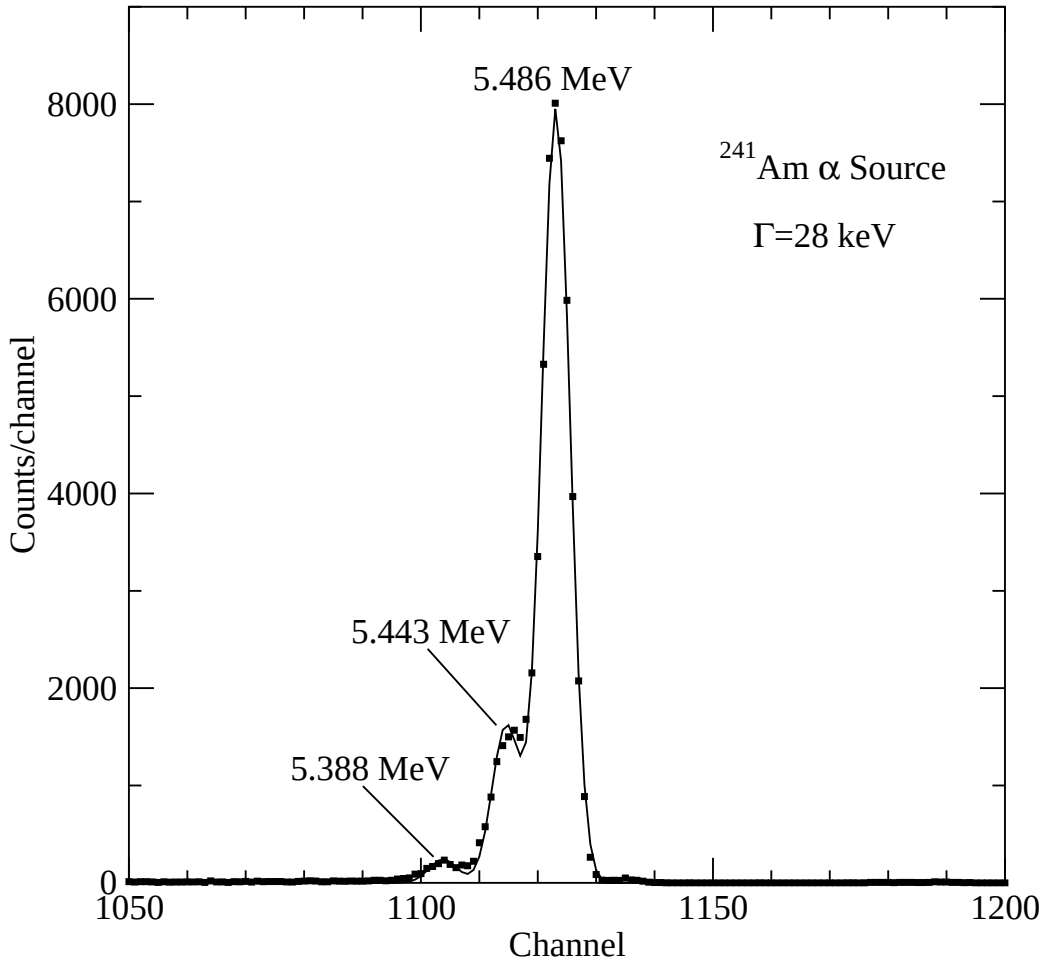

Figure 4.8: ^{241}Am α-source spectrum measured by SIDAR [29]. The three α lines were at 5.486 MeV, 5.443 MeV, and 5.388 MeV. The energy resolution (FWHM) of the SIDAR was determined to be 28 keV.

4.3 Experimental Procedure

A schematic drawing of the experimental configuration is shown in Fig. 4.9. A 32 MeV proton beam from the 25-MV tandem accelerator was used to bombard a ZnS target. Deuterons from the ^{32}S(p,d)^{31}S reaction were detected at forward angles in the Silicon Detector Array (SIDAR) [38, 39]. The deuterons were distinguished from the other reaction products observed (protons, tritons) by running the SIDAR in "telescope" mode with 300-μm-thick ΔE detectors backed by 500-μm-thick E detectors and using the standard ΔE-E techniques. In one set of runs, the SIDAR was arranged to cover laboratory angles 17°– 48°, and a ZnS target with a thickness of 285 μg/cm^2 deposited on 1 μg/cm^2 carbon backing was used. This arrangement ensures a coverage of the ^{31}S excitation energies ranging from 4 – 11 MeV. In a second set of runs, the SIDAR was arranged to cover 31°– 75°, and a 280 μg/cm^2 ZnS target with 5 μg/cm^2 carbon backing was used. The 5 times increase in the backing brought substantially more background in this set of runs, however. The energy resolution obtained for the first set of runs was $\Delta E_{c.m.} \sim$ 80 keV and $\Delta E_{c.m.} \sim$ 130 keV for the second set of runs where the loss of resolution in the second set was due to the greater kinematic broadening at the larger angles covered by the SIDAR. Because of the considerably better energy resolution and much less background contamination in the first set, excitation energies were extracted from these data whenever possible. For the purposes of energy calibration and background identification, another set of runs was taken with a 250 μg/cm^2 Zn target on a 11 μg/cm^2 parylene (C_8H_8) backing over the same angles as the first set of runs. However we did not observe noticeable groups from zinc isotopes. The five deuteron groups observed in the background run were identified with the four lowest levels in ^{11}C from the ^{12}C(p,d)^{11}C reaction and the 6176 keV level in ^{15}O from the ^{16}O(p,d)^{15}O reaction. The beam current was

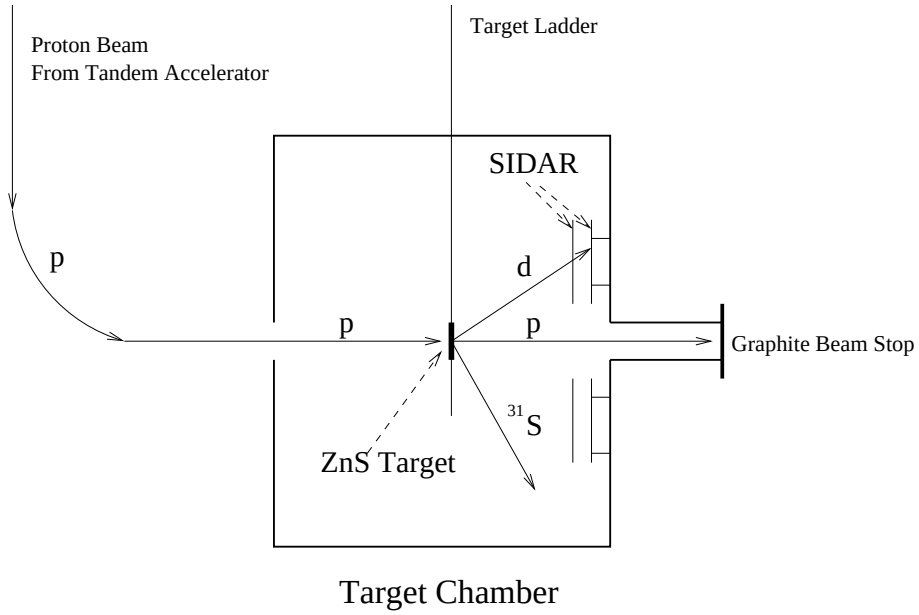

Figure 4.9: A schematic drawing of the experimental configuration.

integrated downstream from the target chamber using a thick graphite beam stop.

Chapter 5

Experimental Results and Discussion

5.1 Energy Calibration

Representative energy spectra for the deuterons gated on the ΔE-E spectrum (see Fig. 5.1), are plotted in Fig. 5.2 for both the data runs and the background runs. The energy calibration was obtained for each of the 16 observed laboratory angles using the data from the background runs, where the deuteron spectra were taken under identical experimental conditions as in the data runs, only changing the target by moving the target ladder. As stated in previous chapter, the five deuteron groups observed in the background run were identified with the four lowest levels in ^{11}C from the ^{12}C(p,d)^{11}C reaction and the 6176 keV level in ^{15}O from the ^{16}O(p,d)^{15}O reaction. We have used the 4 deuteron groups from the ^{12}C(p,d)^{11}C reaction in the background spectra to establish a correlation between measured channels and deuteron energies. The excitation energies of these four levels are well known, and the values span almost the total interesting range of deuteron energies for the ^{32}S(p,d)^{31}S measurement. At each

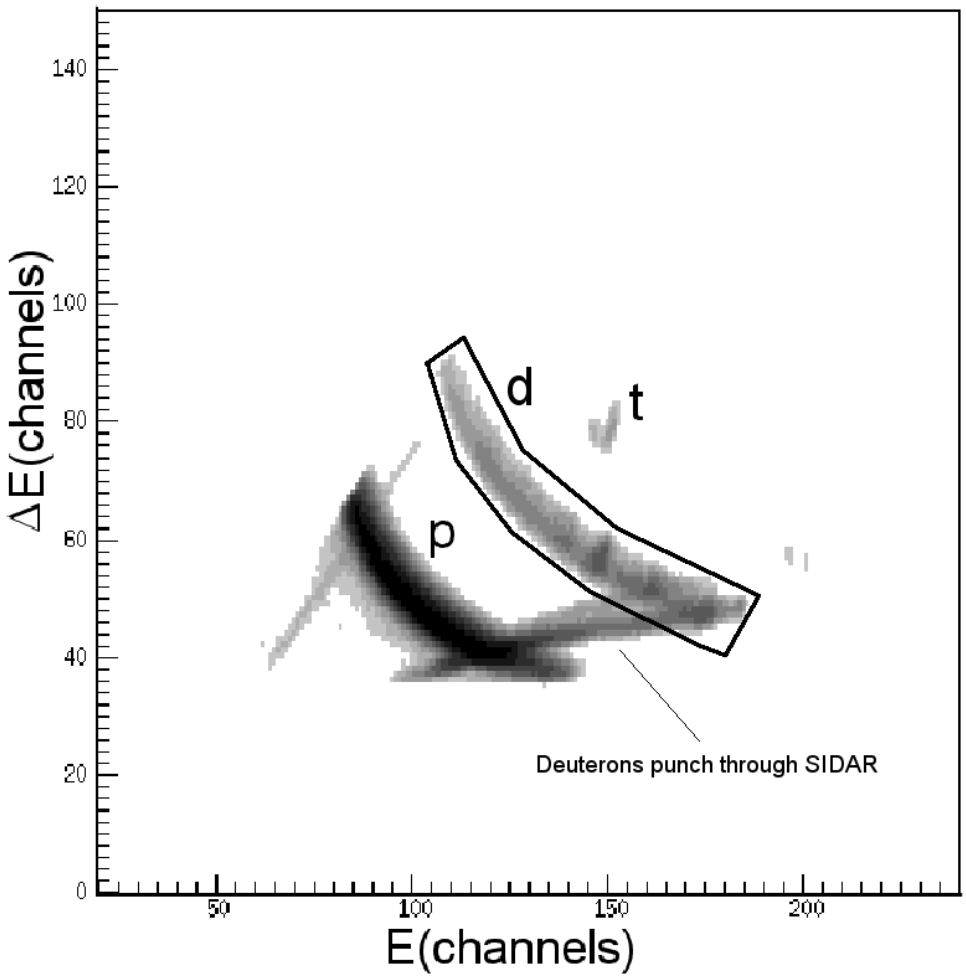

Figure 5.1: Energy loss ΔE vs. total energy E spectrum for all angles covered by the SIDAR.

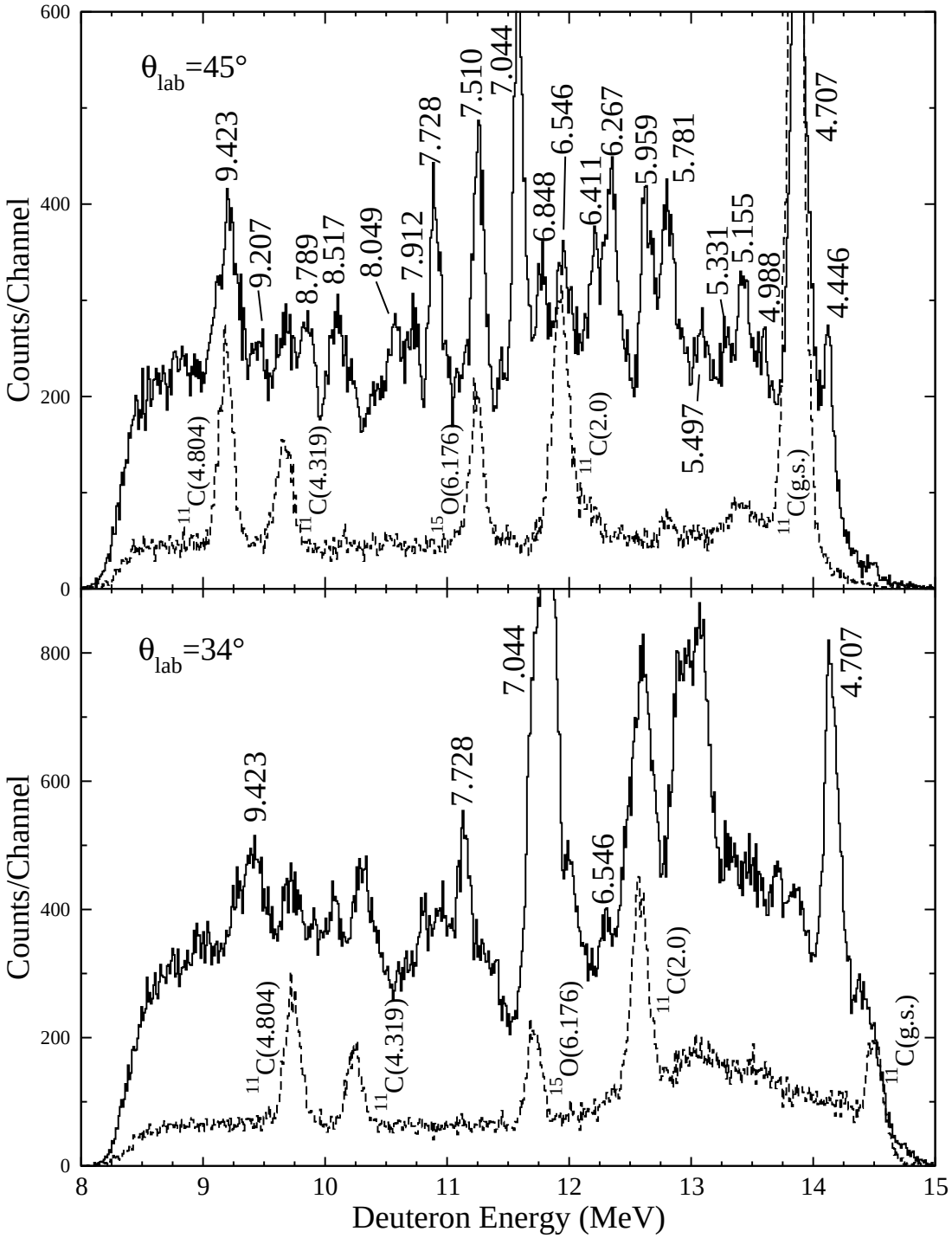

Figure 5.2: Representative deuteron energy spectra from reactions on the ZnS target are shown as solid lines and those from Zn+C_8H_8 target as dashed lines. The peaks from ^{32}S(p,d)^{31}S are labeled by their excitation energies extracted in this measurement.

angle, the centroids of these peaks were extracted and fitted to the expected deuteron energies from kinematics : E_d(MeV) = slope $\times$ centroid(channel) + intercept. For most cases the fits reproduced the expected deuteron energies to within $\pm$ 8 keV. Fig. 5.3 shows background peaks identification. The good agreement between kinematics and from fitting verifies our identification of the groups in the background spectra. Table 5.1 lists the resulted fitting coefficients for energy calibration (the slopes and intercepts).

5.2 Excitation Energies

The calibrations obtained in the previous section were used to deduce the deuteron energies from the ^{32}S(p,d)^{31}S reaction. The deuteron energies were then converted to excitation energies and adopted values were obtained by averaging the excitation energies extracted for the 16 angles.

The excitation energies that we extracted for the states in ^{31}S are labeled in Fig. 5.2 and listed in Table 5.2. A total of 26 energy levels have been observed, of which five states at 8789 keV, 9207 keV, 9606 keV, 9853 keV and 10577 keV have not been previously reported. Our excitation energies agree well with previous measurements [42, 44–47].

The uncertainty for each of the averaged excitation energies was calculated using the standard formalism [40]. Additional sources of uncertainty listed below were considered but found to be negligible [38]. The beam energy has been calibrated to 1/10,000 [41] and was checked at a later time [39]. For deuterons detected in our experiment with energies around 8 – 15 MeV, the energy losses in targets were only a few keV and uncertainties resulting from these small corrections between the two targets were negligible.

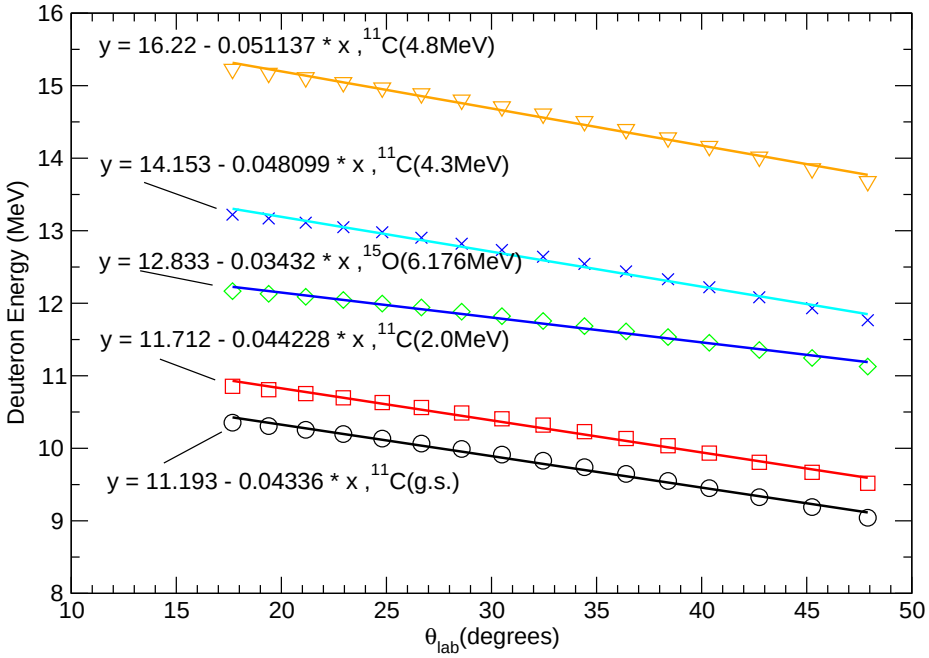

(a)

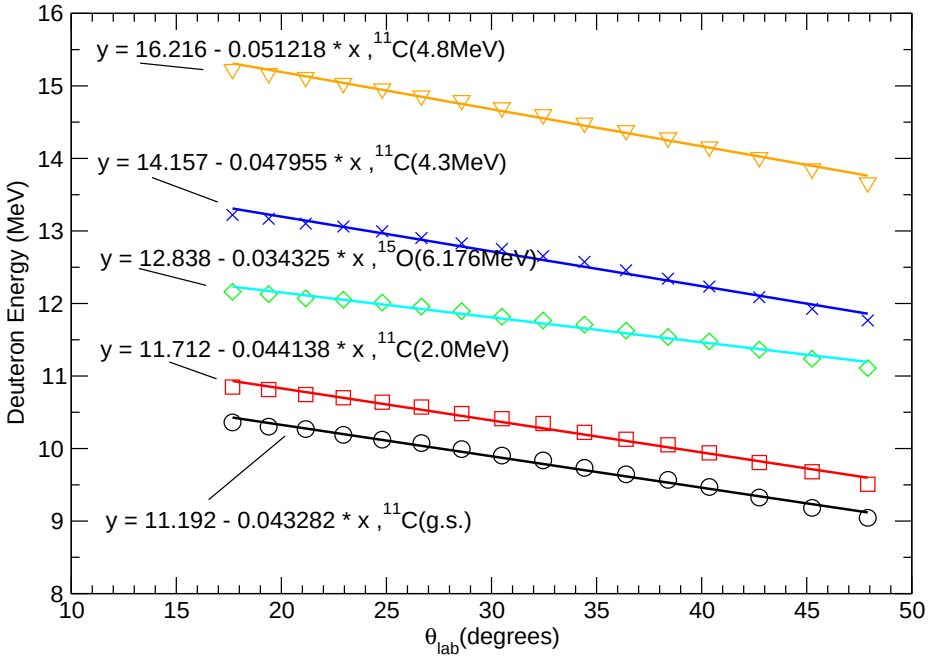

(b)

Figure 5.3: Comparison between kinematics and fitting. Fig. (a) is from kinematics. Fig. (b) is from fitting.

Table 5.1: Fitting results for deuteron energy calibration.

SIDAR strip	θ_{lab}(deg.)	slope	intercept	θ_{lab}(deg.)	slope	intercept
1	18	0.0108	-0.948	31	0.0106	-0.771
2	19	0.0106	-0.637	34	0.0106	-0.728
3	21	0.0107	-0.862	37	0.0109	-1.065
4	23	0.0111	-1.334	40	0.0109	-1.157
5	25	0.0108	-0.977	43	0.0109	-1.205
6	27	0.0104	-0.493	46	0.0103	-0.427
7	29	0.0109	-1.079	49	0.0108	-0.996
8	30	0.0109	-1.057	52	0.0109	-1.131
9	32	0.0107	-0.881	55	0.0105	-0.649
10	34	0.0110	-1.158	58	0.0115	-1.787
11	36	0.0110	-1.138	60	0.0108	-0.985
12	38	0.0108	-0.955	63	0.0106	-0.612
13	40	0.0109	-1.055	65	0.0108	-0.872
14	43	0.0112	-1.335	68	0.0108	-0.990
15	45	0.0112	-1.404	71	0.0114	-1.682
16	48	0.0109	-1.149	75	0.0116	-2.065

Table 5.2: The excitation energies (in keV) of ^{31}S states extracted from this measurement are compared to the previously reported values. Weighted averages of excitation energies from present and previous measurements (see [37, 46, 47]) are listed in the first column.

Weighted average	Ref. [37] Compilation	Ref. [44] ^{29}Si(^{3}He,$n\gamma$) (± 25 kev)	Ref. [45] ^{32}S(^{3}He,α)	Ref. [47] ^{12}C(^{20}Ne,$n\gamma$)	Ref. [46] ^{32}S(^{3}He,α) (± 5 kev)	This work ^{32}S(p,d)
4085 ± 2	4080 ± 8		4083 ± 12		4087	4085 ± 2
4204 ± 7	4204 ± 7		4209 ± 11			
4451 ± 0.4	4452 ± 6		4452 ± 9	4451 ± 0.4	4451	4446 ± 6
4525 ± 8	4525 ± 8		4522 ± 12			
4584 ± 0.3	4580 ± 6		4581 ± 9	4584 ± 0.3	4579	
4711 ± 2	4718 ± 6		4717 ± 9		4720	4707 ± 3
4866 ± 7	4866 ± 7		4866 ± 9			
4976 ± 4	4969 ± 7		4968 ± 10		4975	4988 ± 8
5027 ± 5	5022 ± 12		5026 ± 16		5028	
5156 ± 3	5151 ± 6		5154 ± 12		5161	5155 ± 5
5301 ± 0.3	5306 ± 9		5301 ± 11	5301 ± 0.3	5305	5331 ± 5
5408 ± 9	5408 ± 9		5407 ± 10			
5440 ± 11	5440 ± 11		5448 ± 11			
5515 ± 4	5515 ± 11		5517 ± 15		5519	5497 ± 10
5679 ± 4	5685 ± 8		5680 ± 10		5677	
5779 ± 3	5781 ± 8		5777 ± 11		5777	5781 ± 5
5826 ± 10	5826 ± 10		5824 ± 13			
5890 ± 4	5894 ± 9		5893 ± 10		5889	5959 ± 10 [a]
5978 ± 0.8	5985 ± 10		5983 ± 13	5978 ± 0.8	5975	5959 ± 10 [a]
6160.2 ± 0.7	6155 ± 10		6154 ± 12	6160.2 ± 0.7		
6263 ± 3	6267 ± 10		6268 ± 13		6257	6267 ± 5
6279.5 ± 10	6268 ± 10	6277				
6350 ± 11	6350 ± 11	6361	6348 ± 13			
6376.9 ± 0.5				6376.9 ± 0.5		
6393.8 ± 0.5	6396 ± 10		6395 ± 11	6393.7 ± 0.5	6393	6411 ± 9
6544 ± 9	6543 ± 11		6540 ± 12			6546 ± 15
6593 ± 15	6593 ± 15		6593 ± 15			
6636.2 ± 1.5	6628 ± 13		6628 ± 15	6636.3 ± 1.5		
6712 ± 11	6712 ± 11		6711 ± 13			
6748 ± 10	6748 ± 10		6743 ± 13			

Continued on Next Page...

Table 5.2 – Continued

Weighted average	Ref. [37] Compilation	Ref. [44] ^{29}Si(^{3}He,$n\gamma$) (± 25 kev)	Ref. [45] ^{32}S(^{3}He,α)	Ref. [47] ^{12}C(^{20}Ne,$n\gamma$)	Ref. [46] ^{32}S(^{3}He,α) (± 5 kev)	This work ^{32}S(p,d)
6796 ± 25	6796 ± 25	6796				
6833.4 ± 0.3	6835 ± 9		6834 ± 11	6833.4 ± 0.3		6848 ± 9 [b]
6870 ± 10	6870 ± 10		6862 ± 12			6848 ± 9 [b]
6921 ± 25	6921 ± 25	6921				
6969 ± 5	6996 ± 15				6966	
7006 ± 5		7006				
7038 ± 4	7039 ± 10		7036 ± 11		7033	7044 ± 6
7112 ± 25	7112 ± 25	7112				
7156 ± 4	7155 ± 9		7161 ± 11		7156	
7199 ± 13	7199 ± 13		7199 ± 13			
7303 ± 0.7	7310 ± 11		7310 ± 11	7303 ± 0.7		
7445 ± 25	7445 ± 25	7445				
7511 ± 5	7522 ± 20					7510 ± 6
7600 ± 30	7600 ± 30					
7660 ± 30	7660 ± 30					
7726 ± 3	7715 ± 15		7726 ± 15		7725	7728 ± 4
7768 ± 25	7768 ± 25	7768				
7850 ± 25	7850 ± 25	7850				
7911 ± 5	7888 ± 25	7888				7912 ± 5
7985 ± 25	7985 ± 25	7985				8049 ± 6 [c]
8082 ± 25	8082 ± 25	8082				8049 ± 6 [c]
8174 ± 11	8183 ± 25	8183				8171 ± 12
8362 ± 25	8362 ± 25	8362				
8461 ± 0.5	8453 ± 25	8453		8461 ± 0.5		
8517 ± 13						8517 ± 13
8789 ± 6						8789 ± 6
9154 ± 1.2				9154 ± 1.2		
9207 ± 5						9207 ± 5
9423 ± 7						9423 ± 7
9606 ± 14						9606 ± 14
9853 ± 12						9853 ± 12
10146 ± 1.0				10146 ± 1.0		
10577 ± 13						10577 ± 13

[a,b,c] unresolved doublets

The angles covered by the SIDAR were calculated from the known detector geometry and were cross-checked by noting the relative difference of the energy dependence on angle between deuterons from ^{32}S(p,d)^{31}S and ^{12}C(p,d)^{11}C reactions. All these uncertainties were found negligible compared to the statistical uncertainties.

5.3 Spin and Parity Attributions

Angular distributions were extracted for strongly populated states and are plotted in Fig. 5.4 – 5.11. Gaps appear in the angular distributions where the peak of interest was obscured by contaminant peaks from background reactions. The overall normalization of our cross section data was not well-determined because of uncertainties in target stoichiometry and beam current integration. This uncertainty has no effect on our conclusions concerning the excitation energies and spins of ^{31}S levels. The cross sections measured by Kozub [50] at 33.6 MeV proton energy should be $\sim 10\%$ higher than our 32-MeV measurements. Taking this small difference into account, we have normalized our angular distributions to the data in Ref. [50] and used this normalization to extract spectroscopic factors. To analyze the experimentally measured angular distributions, finite range distorted-wave Born approximation (DWBA) calculations were performed, using the computer code DWUCK5 [53]. We used optical model and bound state parameters from the previous ^{32}S(p,d)^{31}S study [50], which are given in Table 5.3.

These parameters have resulted in good fits to the observed angular distributions (see Fig. 5.4 – 5.11). The observed transitions exhibit angular distributions whose shapes strongly depend on ℓ_n-transfer values. An $\ell_n = 0$ transfer would lead to an unambiguous assignment of spin-parity $1/2^+$ to the final state in ^{31}S, since the target

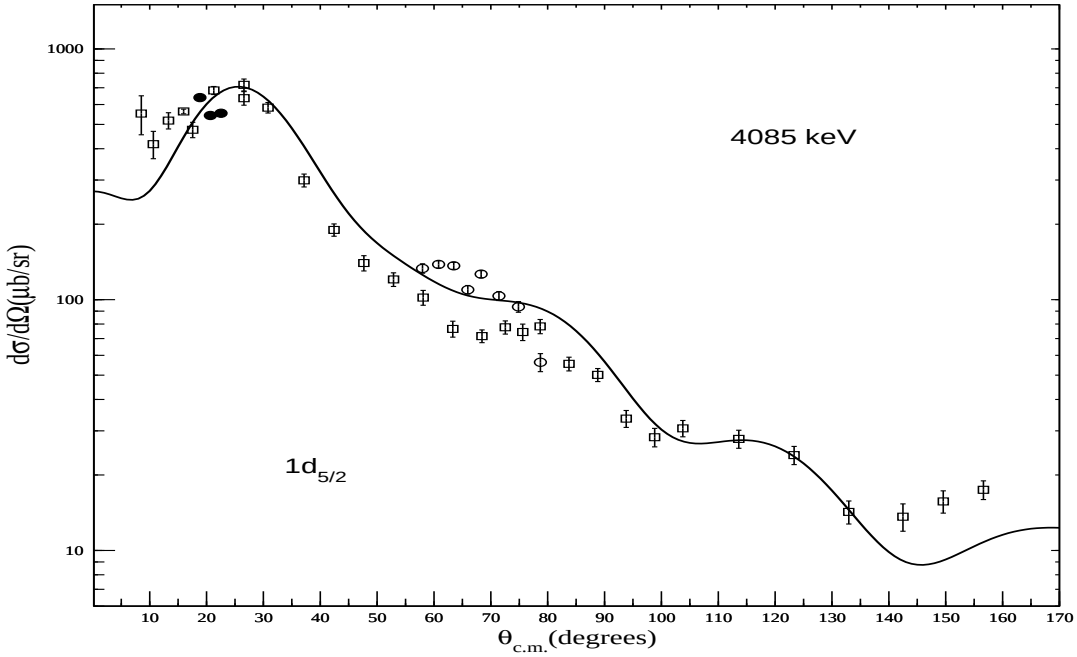

(a)

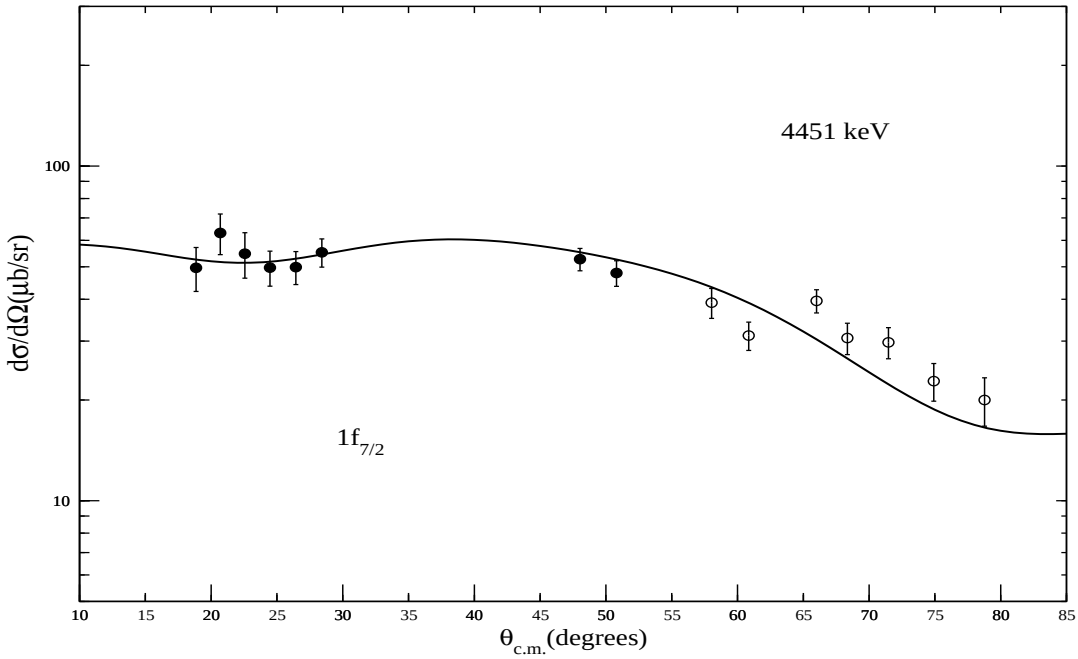

(b)

Figure 5.4: Angular distributions for the data from the first set of runs are plotted as filled circles and those for the data from the second set of runs as empty circles. Data from Kozub [50] are plotted as squares. If not shown, the error is smaller than the point size. Our DWBA calculations best fitting the observed angular distributions are also shown.

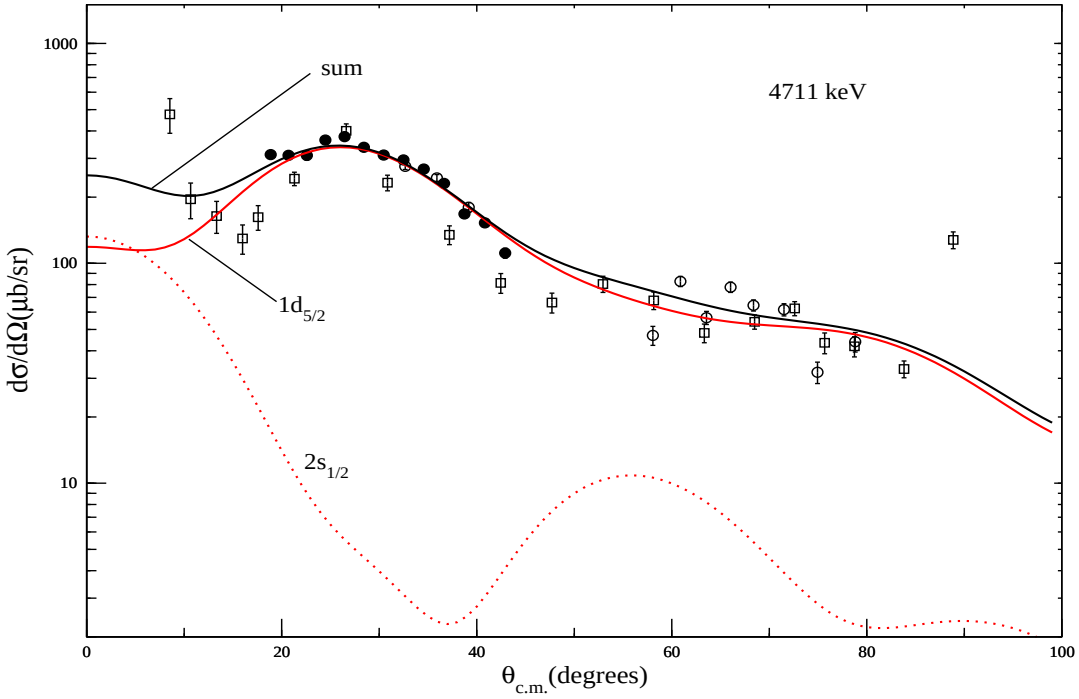

(a)

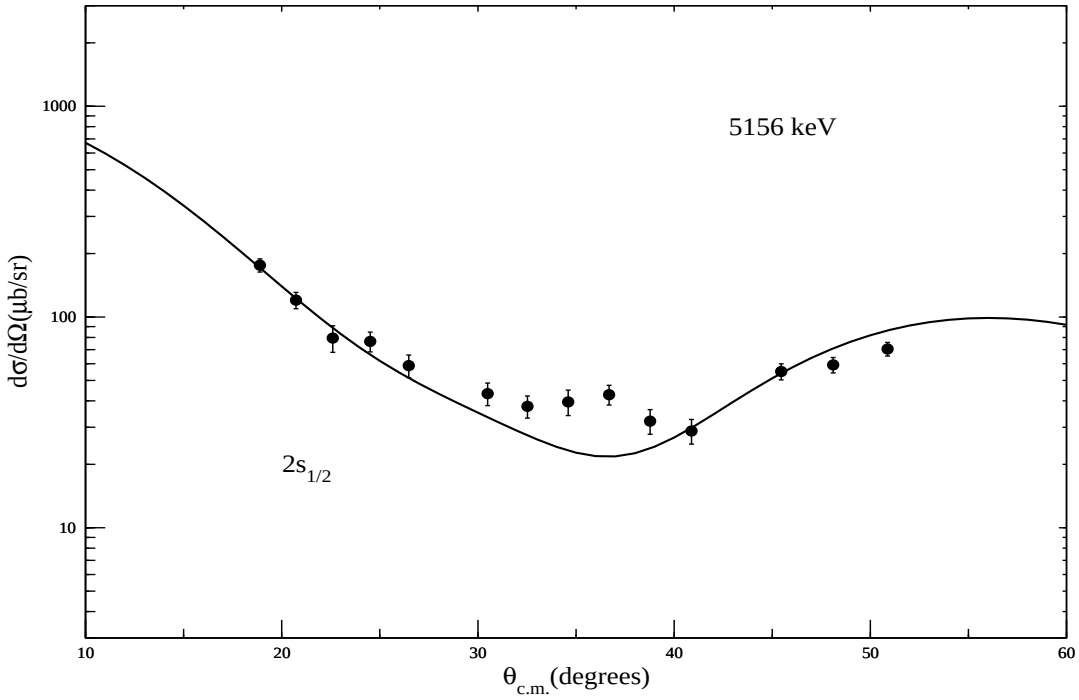

(b)

Figure 5.5: Same as Fig. 5.4, for levels at 4711 and 5156 keV.

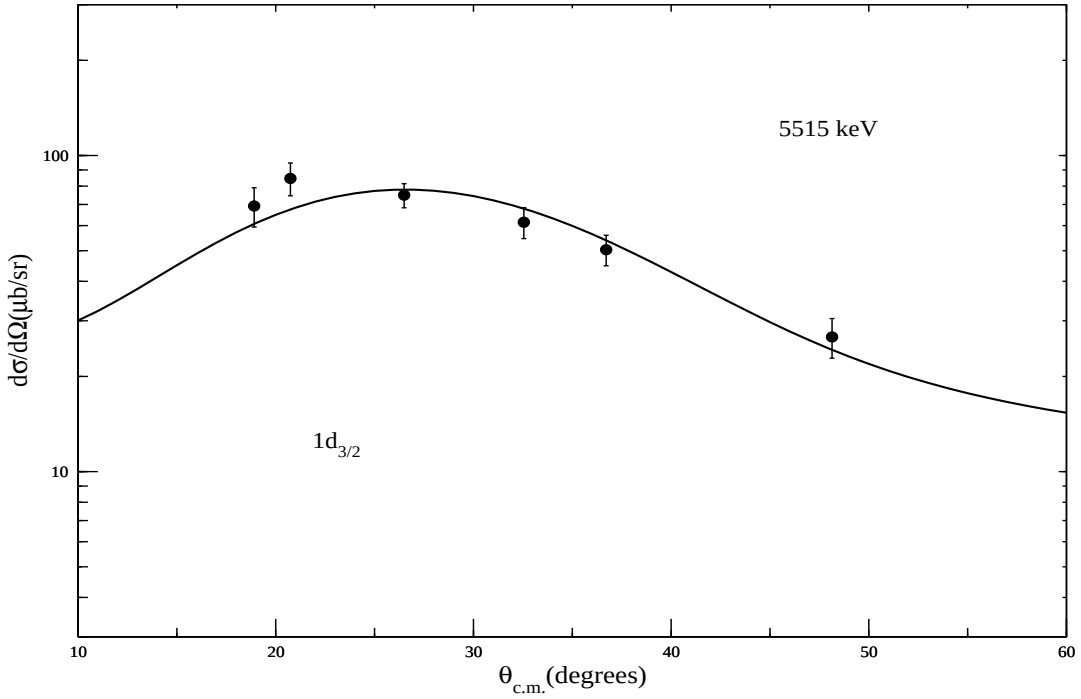

(a)

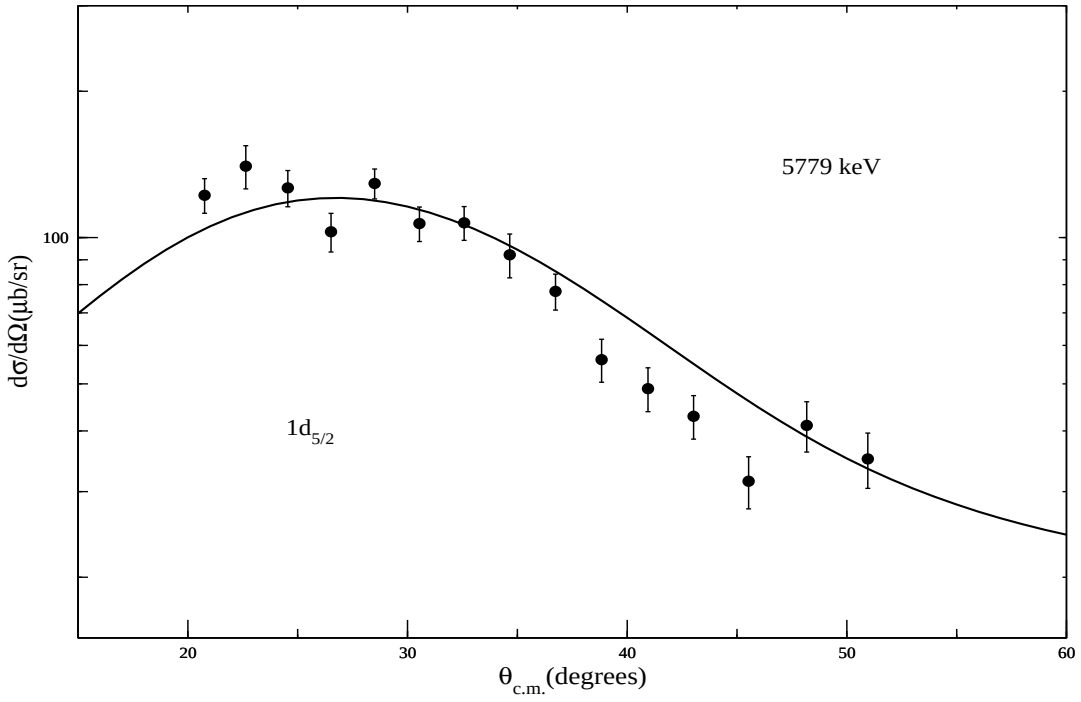

(b)

Figure 5.6: Same as Fig. 5.4, for levels at 5515 and 5779 keV.

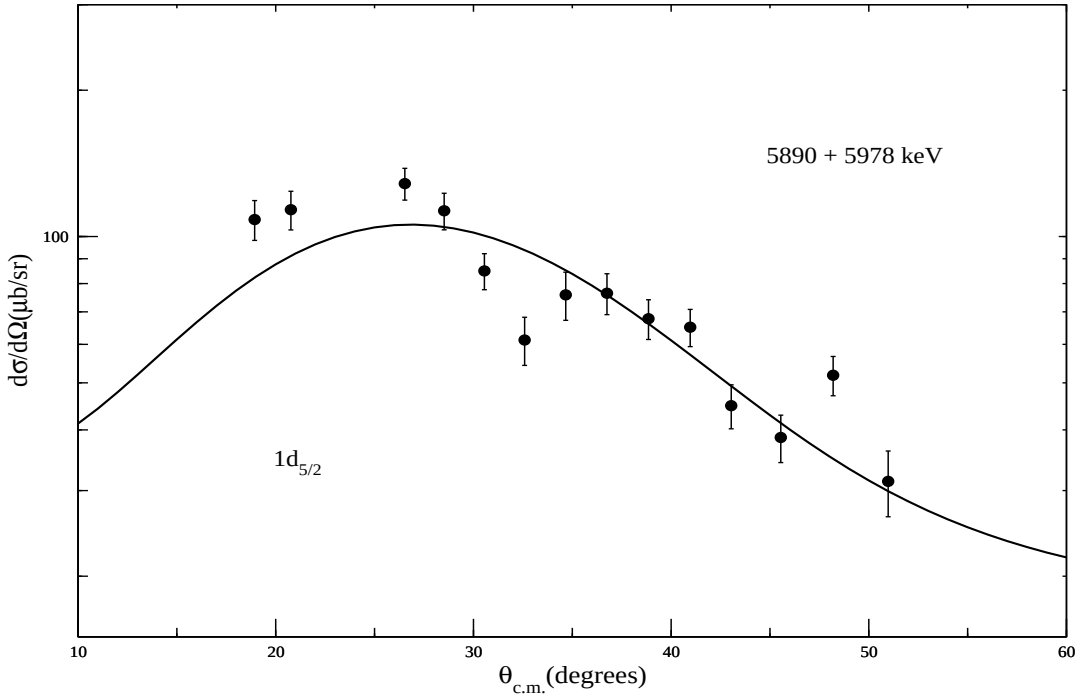

(a)

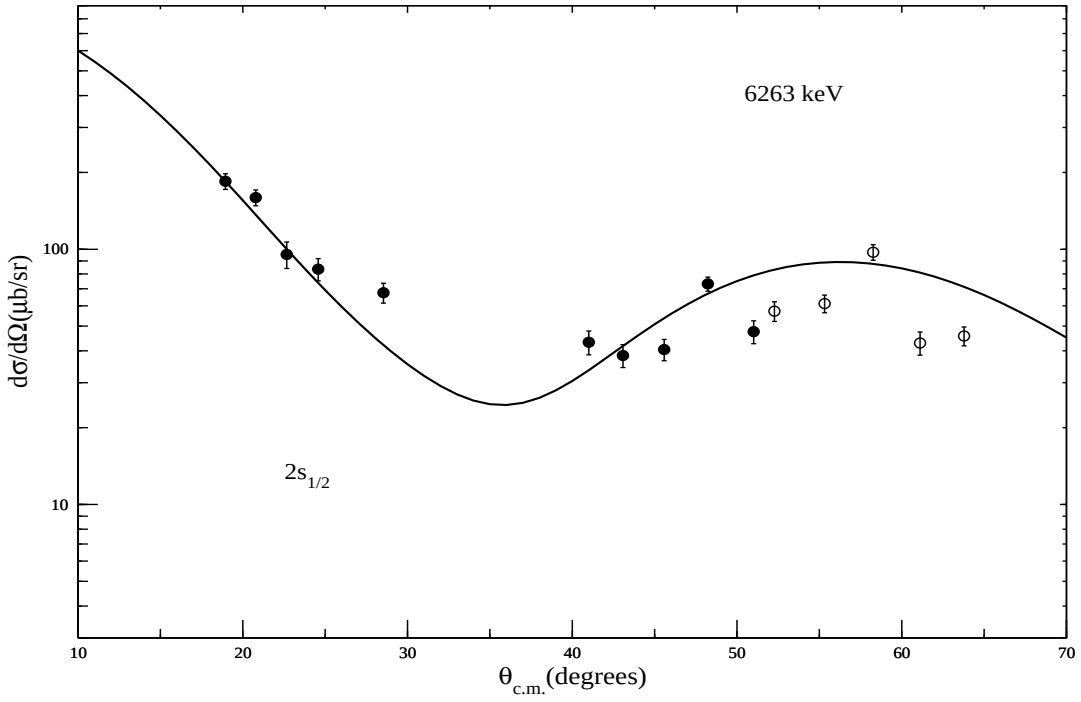

(b)

Figure 5.7: Same as Fig. 5.4, for levels at 5890 and 6263 keV.

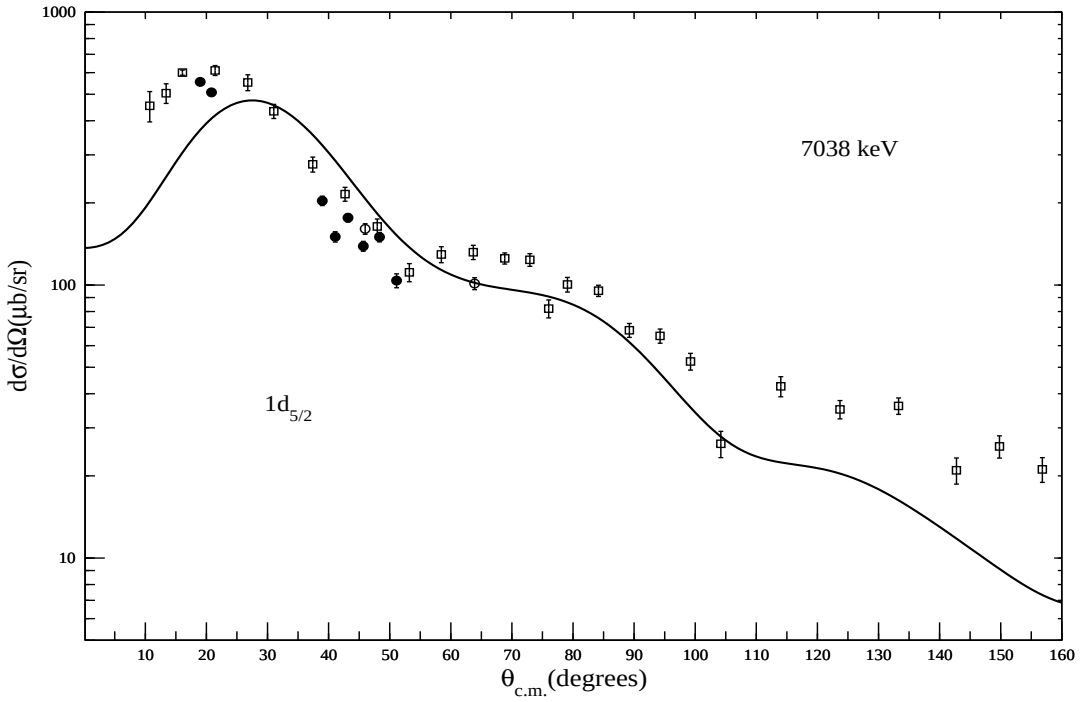

(a)

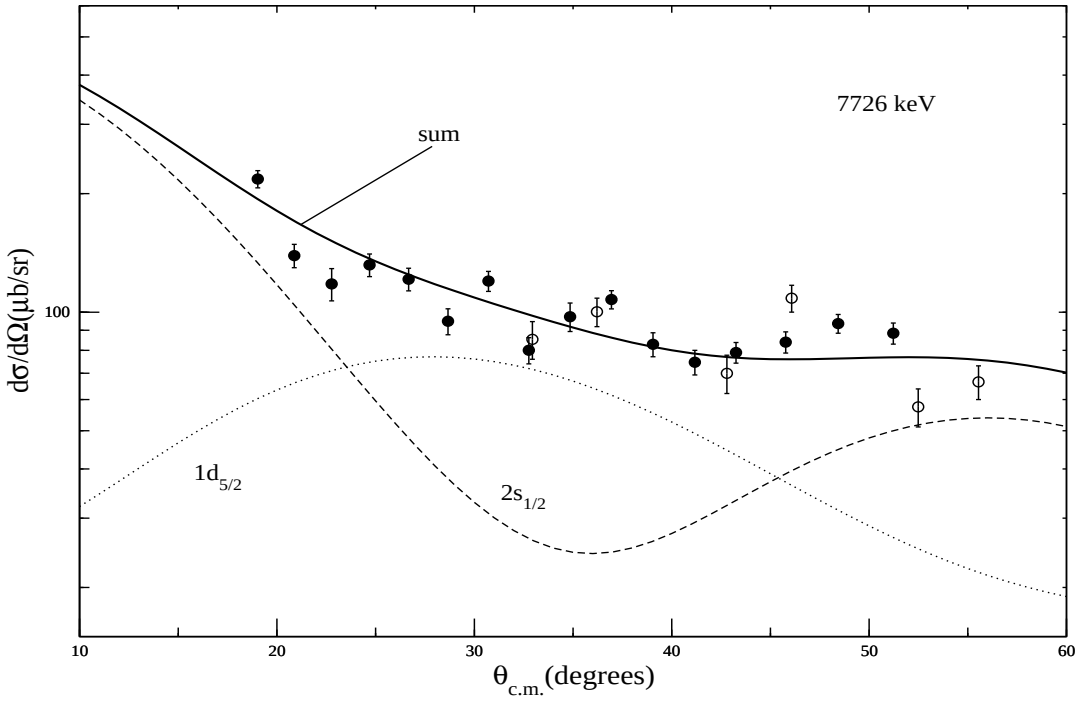

(b)

Figure 5.8: Same as Fig. 5.4, for levels at 7038 and 7726 keV.

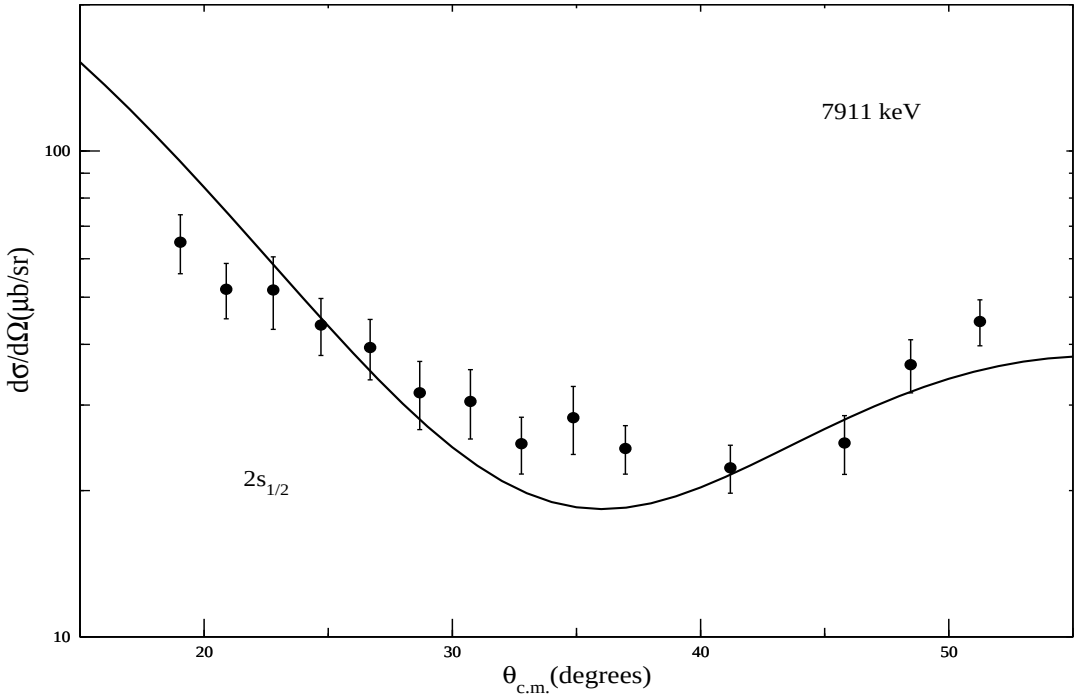

(a)

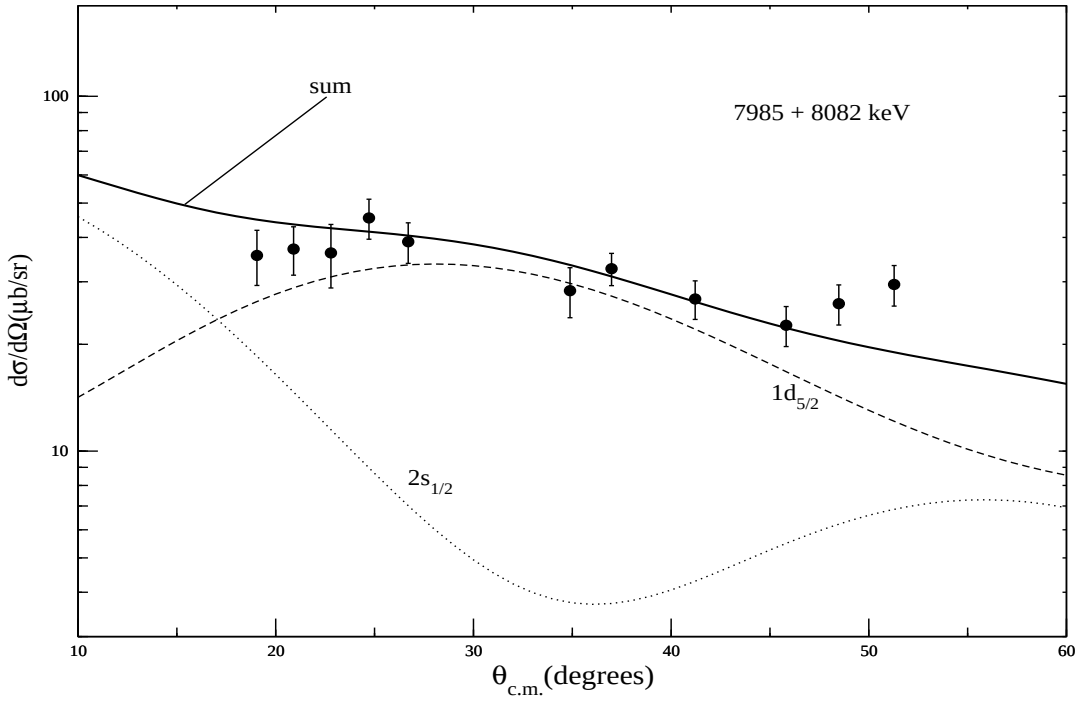

(b)

Figure 5.9: Same as Fig. 5.4, for levels at 7911 and 7985 keV.

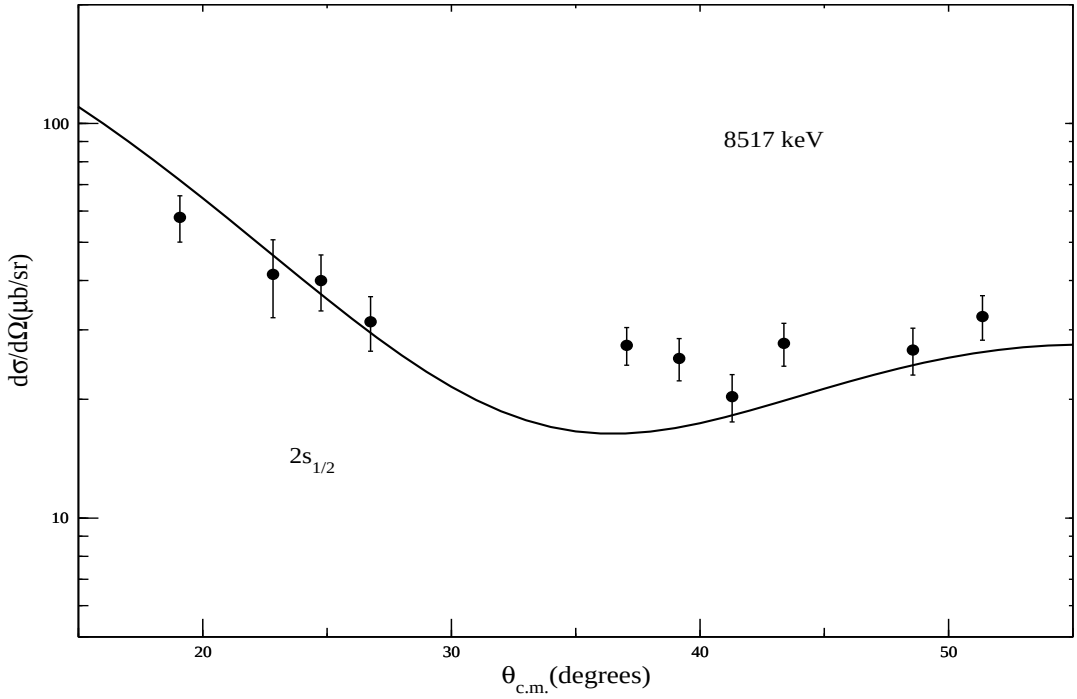

(a)

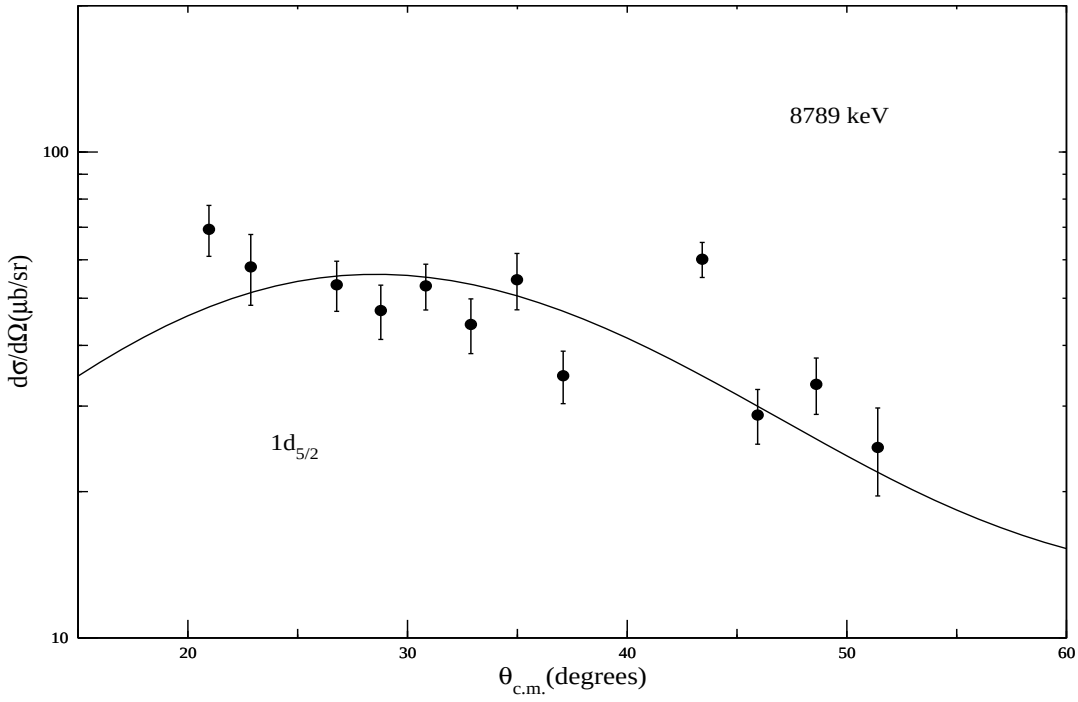

(b)

Figure 5.10: Same as Fig. 5.4, for levels at 8517 and 8789 keV.

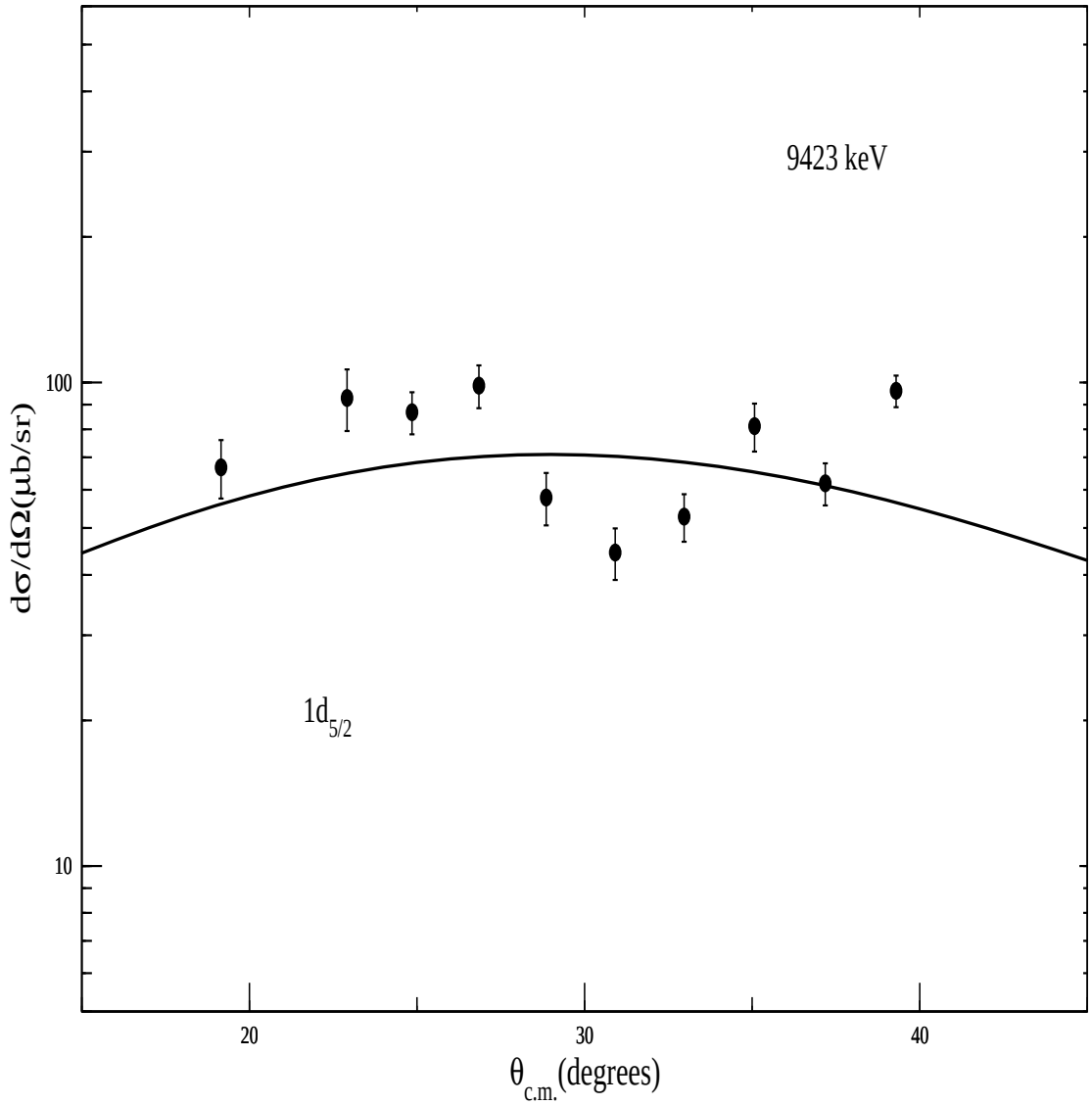

(a)

Figure 5.11: Same as Fig. 5.4, for the 9423-keV level.

Table 5.3: Potential parameters used in DWBA calculations for the ^{32}S(p,d)^{31}S reaction.

Particle	V_R (MeV)	r_R (fm)	a_R (fm)	V_I (MeV)	r_I (fm)	a_I (fm)	r_c (fm)	λ_{SO}
p	47.1	1.18	0.66	27.5	1.18	0.66	1.18	
d	90.0	1.25	0.62	100.0	1.30	0.58	1.18	
n	56.0	1.20	0.65					25

^{32}S is an even-even 0^+ nucleus. For $\ell_n = 1$ or $\ell_n = 2$ transfers, since the angular distributions depend very weakly on the total angular momentum, we could not differentiate between ℓ_n+1/2 and ℓ_n-1/2 transitions. The plotted transitions shown on Fig. 5.4 – 5.11 are for $1p_{1/2}$ and $1d_{5/2}$ transfers, respectively. The proposed spin and parity assignments for all the levels observed in the present measurement are listed in Table 5.4 and are discussed below. Levels not observed in our measurement but lie within 1 MeV above the proton threshold that may contribute to the ^{30}P(p,γ)^{31}S reaction rate are also discussed. Identification of mirror states in ^{31}P and ^{31}S are based on previous studies [37, 46, 47] and present experimental information. Identification of several other pairs of levels as mirror states was also attempted considering two criteria: similarity of the excitation energies and consistency of the J^π values [46]. The validity of these criteria has been demonstrated in previous works (e.g., [37,46,47]).

Neutron spectroscopic factors C^2S were extracted by comparison of our experimental angular distributions with the results of DWUCK5 calculations and are also listed in Table 5.4. By normalizing our cross sections to those of Ref. [50], as discussed above, we obtain spectroscopic factors in good agreement with values from previous neutron pickup studies (see Ref. [46] and references therein).

Table 5.4: J^π values are assigned based on the present measurement and previous studies. Neutron spectroscopic factors C^2S from present work and a previous neutron pickup study ^{32}S(^{3}He,α)^{31}S [46] are listed. ^{31}P mirror states energies and J^π are also listed.

$E_x(keV)$	This work	ℓ_n	J^π	C^2S		^{31}P mirror	
	^{32}S(p,d)			Ref. [46]	This work	$E_x(keV)$	J^π
4085 ± 2	4085 ± 2	2	$5/2^+$	0.77	0.91	4190	$5/2^+$
4204 ± 7			$(1/2-7/2)^+$				
4451 ± 0.4	4446 ± 6	3	$7/2^-$	0.15	0.22	4431	$7/2^-$
4525 ± 8			$3/2^+$				
4584 ± 0.3			$7/2^+$		0.10		
4711 ± 2	4707 ± 3	2	$5/2^+$	0.40	0.38	4783	$5/2^+$
4866 ± 7							
4976 ± 4	4988 ± 8		$3/2^-$		0.04	5015	3/2
5027 ± 5							
5156 ± 3	5155 ± 5	0	$1/2^+$	0.11	0.10	5256	$1/2^+$
5301 ± 0.3	5331 ± 5		$9/2^+$			5343	$9/2^+$
5408 ± 9							
5440 ± 11							
5515 ± 4	5497 ± 10	2	$3/2^+$	0.10		5559	$3/2^+$
5679 ± 4							
5779 ± 3	5781 ± 5	2	$5/2^+$	0.17	0.17	5892	$9/2^+$
5826 ± 10							
5890 ± 4	5959 ± 10 [a]	2	$(3/2,5/2)^+$	0.15	0.12		
5978 ± 0.8	5959 ± 10 [a]	2	$(9/2^+)$		0.20		
6160.2 ± 0.7			$5/2^-$			6399	

Continued on Next Page...

Table5.4 – Continued

$E_x(keV)$	This work	ℓ_n	J^π	C^2S		^{31}P mirror	
	^{32}S(p,d)			Ref. [46]	This work	$E_x(keV)$	J^π
6263 ± 3	6267 ± 5	0	$1/2^+$	0.12	0.17	6337	$1/2^+$
6279.5 ± 10			$3/2^+$			6381	
6350 ± 11			$5/2^+$			6461	
6376.9 ± 0.5			$9/2^-$			6501	
6393.8 ± 0.5	6411 ± 9		$11/2^+$			6454	$11/2^+$
6544 ± 9	6546 ± 15		$5/2^-$			6594	
6593 ± 15			$3/2^-$			6610	
6636.2 ± 1.5			$9/2^-$			6793	
6712 ± 11			$(3/2-7/2)$				
6748 ± 10			$(3/2-7/2)$				
6796 ± 25			$(3/2-7/2)$				
6833.4 ± 0.3	6848 ± 9 [b]		$11/2^-$			6825	
6870 ± 10	6848 ± 9 [b]		$(3/2^-, 5/2^+)$			7080	
6921 ± 25			$5/2^+$			6932	
6969 ± 5			$1/2^+$		0.02		
7006 ± 5			$1/2^+$				
7038 ± 4	7044 ± 6	2	$5/2^+$	0.79	0.76	7158 [d]	$5/2^+$
7112 ± 25			$(1/2, 3/2)^-$			7214	
7156 ± 4			$(3/2, 5/2)^+$		0.11		
7199 ± 13							
7303 ± 0.7			$11/2^+$				
7445 ± 25							
7511 ± 5	7510 ± 6						

Continued on Next Page...

Table5.4 – Continued

$E_x(keV)$	This work	ℓ_n	J^π	C^2S		^{31}P mirror	
	^{32}S(p,d)			Ref. [46]	This work	$E_x(keV)$	J^π
7600 ± 30							
7660 ± 30							
7726 ± 3	7728 ± 4	0+2					
7768 ± 25							
7850 ± 25							
7911 ± 5	7912 ± 5	0	$1/2^+$	0.06			
7985 ± 25	8049 ± 6 [c]	0+2	$(1/2, 3/2, 5/2)^+$				
8082 ± 25	8049 ± 6 [c]	0+2	$(1/2, 3/2, 5/2)^+$				
8174 ± 11	8171 ± 12						
8362 ± 25							
8461 ± 0.5			$(13/2^-)$				
8517 ± 13	8517 ± 13	0	$1/2^+$	0.05			
8789 ± 6	8789 ± 6	2	$(3/2, 5/2)^+$	0.13			
9154 ± 1.2			$13/2^+$				
9207 ± 5	9207 ± 5						
9423 ± 7	9423 ± 7	2	$(3/2, 5/2)^+$	0.19			
9606 ± 14	9606 ± 14						
9853 ± 12	9853 ± 12						
10146 ± 1.0			$(13/2^-)$				
10577 ± 13	10577 ± 13						

[a,b,c] unresolved doublets

[d] from Ref. [46]: ^{32}S(^{3}He,α)^{31}S at $E_{^3He}$ = 25 MeV

4085 keV level. This level has been reported to have J^π=(3/2, 5/2)$^+$ [37] deduced from various transfer reaction studies [44, 48, 50]. Vernotte *et al.* reported this level to have J^π=5/2$^+$ on the basis of a ^{32}S(^{3}He,α)^{31}S study [46]. The combined angular distribution from present work and Kozub's [50] previous measurement is well fit by an $\ell_n = 2$ transfer and thus supports this assignment. This level was identified as being the mirror of the ^{31}P state at 4190 keV with J^π=5/2$^+$ [37, 46].

4451 keV level. This level is given an assignment of (5/2,7/2)$^-$ in Ref. [37] obtained from a ^{32}S(^{3}He,α)^{31}S study [45]. Vernotte *et al.* [46] reported this level to have 7/2$^-$ assignment. A ^{12}C(^{20}Ne,$n\gamma$)^{31}S study by Jenkins *et al.* [47] yielded the same J^π of 7/2$^-$. In our measurement the angular distribution is reasonably well reproduced by an $\ell_n = 3$ transfer. The present assignment is J^π=7/2$^-$. It was identified with the 4431 keV 7/2$^-$ level in ^{31}P [37, 46].

4711 keV level. In the adopted level scheme [37] this level is assigned J^π=(3/2, 5/2)$^+$ [37] obtained from (^{3}He,α) [43] and (p,t) [48] studies. Vernotte *et al.* [46] assigned 5/2$^+$ to the level at 4720 keV. In our case this level is strongly populated. The combined angular distribution from our data and Kozub's previous measurement [50] is well reproduced by an $\ell_n = 2$ transfer with a small component of $\ell_n = 0$ admixture to account for the rise at small angles. Based on present work and previous measurements this level is assigned with J^π=5/2$^+$. It has been identified with the 4783 keV 5/2$^+$ mirror state in ^{31}P [37, 46].

4976 keV level. The level at 4969 keV in the adopted level scheme [37] was assigned a J^π=(1/2,3/2)$^-$ from a ^{32}S(^{3}He,α)^{31}S study [45]. This is supported by Vernotte *et al.* [46] in their (^{3}He,α) measurement with an $\ell_n = 1$ neutron pickup. In our experiment this level is only weakly populated, and we could not extract an angular distribution. In Ref. [46] it was identified as the mirror of the 3/2 state in ^{31}P at 5014.9 keV and assigned with 3/2$^-$.

5156 keV level. The 5156 keV state was reported to be a $1/2^+$ [37], and it was confirmed by Vernotte *et al.* [46]. In our measurement the extracted angular distribution was well reproduced by an $\ell_n = 0$ transfer leading to an unambiguous $1/2^+$ assignment. This level is the mirror state of the 5256 keV level in ^{31}P.

5301 keV level. We could not extract an angular distribution for this state because of its relatively weak population. It was reported to be a $9/2^+$ level in Ref. [47]. This large spin value explains the weak population in the present experiment, as the (p, d) reaction prefers a small angular momentum transfer. Based on the similarity of the excitation energies and consistency of the J^π values, this level could be identified as being the mirror of the 5343 keV level in ^{31}P with J^π=$9/2^+$ [47].

5515 keV level. This level had not previously been given an assignment. In our measurement this level is quite weakly populated and the extracted angular distribution is compatible with an $\ell_n = 2$ transition which leads to an assignment of J^π=$(3/2,\ 5/2)^+$. Moss [45] has found possible presence of $\ell_n = 3$ component but it appears unlikely in our case. We tentatively identified it as being the mirror of the 5559 keV level in ^{31}P with J^π=$3/2^+$ based on similar excitation energies and spins.

5779 keV level. This level was given an assignment of J^π=$(3/2,\ 5/2)^+$ [37] resulting from an $\ell_n = 2$ transfer in a ^{32}S(^{3}He,α)^{31}S study [43]. Vernotte *et al.* [46] identified this level with the 5892 keV in ^{31}P and assigned both levels with $5/2^+$. In our measurement this level is reasonably populated and the angular distribution was well fit by an $\ell_n = 2$ transfer and thus supports the $5/2^+$ assignment.

5890 and 5978 keV levels. The states at 5894 and 5985 keV in the adopted level scheme [37] were not separated in our study. It had been reported that the higher-energy level was a $9/2^+$ state [47]. The lower-energy level was assigned a J^π=$(3/2,\ 5/2)^+$ based on an $\ell_n = 2$ transfer in ^{32}S(^{3}He,α)^{31}S studies [43, 46]. Our

extracted angular distribution is well fit by an $\ell_n = 2$ transition and thus supports this assignment.

6160 keV level. This level was not observed in our measurement. Jenkins *et al.* [55] has reported this level at 6160 keV and identified this level the mirror of the J^π $5/2^-$ state in ^{31}P at 6399 keV on the basis of their very similar decay branches.

6263 keV level. The 6263 keV state has been assigned spin and parity quantum numbers of $1/2^+$ and identified as the mirror partner of the 6337 keV state in ^{31}P [37, 46]. In the present measurement this level was reasonably populated and the angular distribution was well fit by an $\ell_n = 0$ transfer, and thus confirmed the unambiguous J^π $1/2^+$ assignment.

6279 keV level. The level at 6268 keV in Ref. [37] is not expected to be populated in our ^{32}S(p,d)^{31}S measurement since it is known to have isospin T=3/2. Kankainen *et al.* [52] deduced a more precise excitation energy of 6280±2 keV in a ^{31}Cl β-decay study. It is the mirror state of the T=3/2 6381 keV level in ^{31}P (J^π=$3/2^+$). We do not expect a strong contribution to the ^{30}P(p,γ)^{31}S rate from this T=3/2 state by proton capture on a T=0 ground state of ^{30}P.

6350 keV level. The 6350 keV level was not observed in the present measurement. In their ^{29}Si(^{3}He,n)^{31}S study [44], Davidson *et al.* found this state well populated through L=2 transfer. This would allow J^π=$(3/2, 5/2)^+$ assignment for the 6350 keV level. We tentatively link it as the mirror of the $5/2^+$ state in ^{31}P at 6461 keV based on similarity in excitation energies and consistency in J^π values.

6377 keV level. This level was only observed in Ref. [47] and was assigned a J^π=$9/2^-$.

6394 keV level. This level was observed by Jenkins *et al.* [47] with an assignment of $J^\pi = 11/2^+$, and was identified with the $11/2^+$ level in ^{31}P at 6454 keV. We could not extract an angular distribution due to its weak population. We would expect the

contribution of this level to the ^{30}P(p,γ)^{31}S rate negligible for such an $\ell_p = 4$ proton capture.

6544 and 6593 keV levels. The 6544 keV level was only observed at two angles and the 6593 keV level was not observed in the present work. They were proposed by Jenkins *et al.* [55] to have J^π=5/2$^-$ and 3/2$^-$, respectively.

6636 keV level. This level was not observed in our study. It was observed by Jenkins *et al.* [55] and was proposed as the analogue of the 9/2$^-$ state in ^{31}P at 6793 keV on the basis of similar γ-decay schemes.

6712, 6748 and 6796 keV levels. We do not observe any of these states in the present work. Jenkins *et al.* [55] tentatively proposed these levels to have J^π=(3/2 - 7/2) assignments.

6833 and 6870 keV levels. The previously reported states at 6835 and 6870 keV [37] were not separated in our study. The centroid of the combined peak was found at 6848 keV. In their ^{12}C(^{20}Ne,$n\gamma$)^{31}S study, Jenkins *et al.* [47] observed a 6833 keV level with $J^\pi = 11/2^-$, and identified it as being the mirror of the 11/2$^-$ state in ^{31}P at 6825 keV. They assigned the 6870 keV level with J^π=(3/2$^-$, 5/2$^+$) [55].

6921 keV level. The 6921 keV level was only observed previously in a ^{29}Si(^{3}He,n)^{31}S study [44] without spin and parity assigned. We do not observe this level in the present work. Based on similarity of the excitation energies and consistency of the J^π values, this level is likely the analogue of the 6932 keV state in ^{31}P with J^π=5/2$^+$.

6969 and 7006 keV levels. In the adopted level scheme [37] they were considered as one level which is the mean value of three levels obtained from various sources. The level observed in the ^{29}Si(^{3}He,n)^{31}S reaction [44] (E$_x$=7006 keV, J^π=1/2$^+$) was identified as being the second T = 3/2 state of ^{31}S. Vernotte *et al.* [46] pointed out that since the population of a T=3/2 state through the ^{32}S(^{3}He,α)^{31}S reaction [42,43]

is isospin forbidden, the presence of two distinct levels at 6990 and 7006 keV, respectively was assumed. They also observed the lower level at 6966 keV and assigned it with J^π=$1/2^+$.

7038 keV level. This level has been reported previously to have J^π=(3/2, 5/2)$^+$ [37]. Vernotte *et al.* [46] assigned it with J^π=$5/2^+$ and identified it with a ^{31}P level at 7158 keV. The angular distribution extracted in our study combined with data from a previous (p, d) measurement [50] was well fit by an $\ell_n = 2$ transfer and thus supports the $5/2^+$ assignment.

7112 keV level. We do not observe this level in the present work. It was only previously reported in a ^{29}Si(^{3}He,n)^{31}S reaction [44] without spin and parity assignment. To calculate its possible contribution to the ^{30}P(p,γ)^{31}S rate we tentatively identify it as being the analogue of the J^π=(1/2, 3/2)$^-$ state in ^{31}P at 7214 keV based on similarity in excitation energies and consistency of the J^π values.

7156 keV level. The 7156 keV level was not observed in our measurement. It was previously given a $J^\pi = (3/2, 5/2)^+$ assignment on the basis of an $\ell_n = 2$ transition in a ^{32}S(^{3}He,α)^{31}S study [43]. Vernotte *et al.* [46] supported this assignment.

7303 keV level. This level was not observed in the present measurement. Jenkins *et al.* [47] observed it at 7303 keV with $J^\pi = 11/2^+$.

7511 keV level. This level was previously only observed by F. Ajzenberg-Selove *et al.* [42]. It was quite weakly populated in the present measurement, and a reasonable angular distribution could not be extracted.

7726 keV level. This level was previously reported by J. Aysto [49] *et al.* to have J^π= (1/2 to 5/2)$^+$ assignment. Vernotte *et al.* [46] observed a broad peak at 7725 keV, and they fitted the angular distribution by a superposition of $\ell_n = 1$ and 2 transitions, or $\ell_n = 1$ and 3 transitions. They thus considered this level a combination

of several levels. The angular distribution we extracted is best fit by a combination of $\ell_n = 0 + 2$ transfers.

7911 keV level. A level at 7888 keV was reported by Davidson *et al.* [44]. Källne and Fagerström reported a 7970±70 keV level in a ^{32}S(p,d)^{31}S study [51]. We extracted an angular distribution best reproduced by an $\ell_n = 0$ angular momentum transfer, and assigned spin and parity $1/2^+$.

7985 and 8082 keV levels. These two levels are not separated in our measurement. We observed a level at 8049 keV. The angular distribution we extracted is compatible with a combination of $\ell_n = 0 + 2$ transitions, indicating it might be the combined peak of the nearby 7985 and 8082 keV levels, respectively.

8174 keV level. This level was only weakly populated in our measurement and an angular distribution could not be extracted. It was only observed previously in a ^{29}Si(^{3}He,n)^{31}S study [44].

8517 keV level. The 8517 keV level has only been reported recently by Kankainen *et al.* [52] (E_x = 8509±30 keV) via a ^{31}Cl β-decay study . The angular distribution extracted in our measurement is compatible with an $\ell_n = 0$ transfer leading to an assignment of $J^\pi = 1/2^+$.

8789 keV level. This level has not been reported previously. Our extracted angular distribution was best fit by an $\ell_n = 2$ transfer which allows J^π=(3/2, 5/2)$^+$.

9423 keV level. Källne and Fagerström reported a level at 9430±100 keV in their ^{32}S(p,d)^{31}S study [51]. The angular distribution we extracted is compatible with an $\ell_n = 2$ transition which allows J^π=(3/2, 5/2)$^+$, however we could not rule out the possibility of an $\ell_n = 3$ transfer.

9207, 9606, 9853 and 10577 keV levels. These levels have not been previously reported. They were weakly populated in our measurement and angular distributions could not be extracted.

Chapter 6

Astrophysical Implications

6.1 A New ^{30}P(p,γ)^{31}S Reaction Rate

As stated previously, the ^{30}P(p ,γ)^{31}S reaction rate has been found to play a pivotal role in nova nucleosynthesis in the heavier Si-Ca mass region [26, 28, 35]. With improved information on the ^{31}S levels, we re-evaluate the ^{30}P(p,γ)^{31}S rate. We group together in Table 6.1 the properties of resonances in ^{31}S up to 1 MeV above the p+^{30}P threshold, which might contribute to the ^{30}P(p,γ)^{31}S rate at nova temperatures.

The dimensionless proton single-particle reduced widths θ^2_{sp} were calculated following the approach proposed by Iliadis [54]. In that study, dimensionless single-particle reduced widths θ^2_{sp} are calculated for target masses of A = 12-50 by comparing proton partial widths obtained from optical-model computations and from R-matrix expressions. The dependence of θ^2_{sp} on target mass, bombarding energy, interaction radii, etc., is investigated. Least-squares fits to the values of θ^2_{sp} calculated in the work were performed by using the expression:

$$\theta^2_{sp} = \sum_{i,j=0}^{2} c_{ij} A^i E^j \tag{6.1}$$

Table 6.1: A summary of the resonance properties within 1 MeV above the proton threshold used to calculate the ^{30}P(p,γ)^{31}S reaction rate. E_r is the resonance energy with respect to the p+^{30}P threshold at 6133 keV. ℓ_p is the orbital angular momentum transfer for proton capture. C^2S is the spectroscopic factor for the p+^{30}P system, τ is the life time in units of fs, and $\omega\gamma$ is the resonance strength (see Chapter 2).

E_x(keV)	E_r(keV)	ℓ_p	θ^2_{sp}	C^2S	Γ_p(keV)	τ(fs)	Γ_γ(keV)	$\omega\gamma$(keV)
6160.2	27.2	1	0.68	0.02	3.91E-34			3.91E-34
6263	130	0	0.56	0.003	2.23E-13			[a] 7.70E-14
		2	0.32	0.015	7.86E-15			
6350	217	2	0.33	0.044	2.36E-10			2.36E-10
6376.9	243.9	3	0.31	0.02	1.36E-11			2.27E-11
6393.8	260.8	4	1.00	0.02	1.27E-12			2.54E-12
6544	411	1	0.69	0.02	1.88E-05	3.9	1.69E-04	1.69E-05
6593	460	1	0.69	0.02	6.47E-05	3.9	1.69E-04	3.12E-05
6636.2	503.2	3	0.32	0.02	1.68E-07	202	3.26E-06	2.66E-07
6712	579	1	0.68	0.02	6.44E-04	3.9	1.69E-04	8.92E-05
6748	615	1	0.68	0.02	1.13E-03	3.9	1.69E-04	9.80E-05
6796	663	1	0.68	0.02	2.22E-03	3.9	1.69E-04	1.05E-04
6833.4	700.4	5	1.00	0.02	3.26E-09	123	5.37E-06	6.52E-09
6870	737	1	0.68	0.02	5.50E-03	3.9	1.69E-04	1.09E-04
6921	788	2	0.35	0.02	4.33E-04	3.9	1.69E-04	1.22E-04
6969	836	0	0.53	0.02	4.38E-02	3.9	1.69E-04	5.61E-05
7038	905	2	0.35	0.02	1.35E-03	3.9	1.69E-04	1.50E-04
7112	979	1	0.67	0.02	4.85E-02	3.9	1.69E-04	5.61E-05
7156	1023	2	0.36	0.02	3.59E-03	3.9	1.69E-04	1.61E-04

[a] Sum of contributions from ℓ_p=0 and ℓ_p=2.

where A is atomic mass in units of amu and E is energy in units of keV, respectively. The coefficients c_{ij} are listed in Table 6.2 for different single-particle orbits $n\ell$.

The θ^2_{sp} values are then converted into proton widths at corresponding energies using the formula [17]:

$$\Gamma_l(E) = \frac{2\hbar}{R_n}\left(\frac{2E}{\mu}\right)^{1/2} P_l(E, R_n) C^2S\theta^2_{sp} \tag{6.2}$$

where $P_l(E, R_n)$ is the penetration factor defined in Chapter 2, R_n the nuclear radius, μ the reduced mass and C^2S the spectroscopic factor. C^2S here refers to the ^{30}P+p system and should not be confused with the ^{31}S+n spectroscopic factors in Table 5.4.

We have followed the procedures of Jenkins *et al.* [55] in determination of the spectroscopic factors and γ widths for the resonances. For the 6263 and 6350-keV states, we use spectroscopic factors obtained by Jenkins *et al.* [55] from an *sd* shell model calculation. For states where the spectroscopic factor is unknown, a value of 0.02 was assumed based on an investigation of the typical proton spectroscopic factors for states at similar excitation energies in mirror nuclei ^{31}P [55, 56]. For the first 6 resonances above the proton threshold, the γ width can safely be ignored since $\Gamma_p \ll \Gamma_\gamma$. For the higher lying resonances, the γ widths are obtained from the lifetimes of the mirror ^{31}P states if known. For the higher lying low-spin, negative parity states, a typical γ width corresponding to the 4 fs lifetime of the $3/2^-$ state at 6909 keV in ^{31}P was adopted [55]. We neglect the states at 6279 and 7006 keV since we do not expect significant contribution to the ^{30}P$(p,\gamma)^{31}$S rate from these T = 3/2 states by proton captures on a T = 0 ground state of ^{30}P.

Using these resonance parameters in Table 6.1, we have calculated the reaction rate for contribution of each of the individual resonances and the total rate (see

Table 6.2: Parameters c_{ij} of least-squares fits to calculated θ^2_{sp} values for different orbits $n\ell$ (see Ref. [54])

	2s	2p	1d	1f
c_{00}	5.101E-01	8.535E-01	6.336E-01	6.795E-01
c_{10}	1.054E-02	-3.509E-03	-1.398E-02	-1.720E-02
c_{01}	-7.272E-04	-4.816E-04	-2.358E-05	-1.283E-05
c_{11}	2.553E-05	2.654E-05	3.767E-06	1.439E-06
c_{20}	-2.842E-04	-7.822E-05	1.177E-04	1.637E-04
c_{02}	2.882E-07	-6.158E-08	-6.147E-09	2.925E-08
c_{21}	-1.125E-07	-3.087E-07	-6.299E-08	-2.109E-08
c_{12}	-9.167E-09	6.296E-10	3.686E-10	-4.395E-10

Chapter 2 for reaction rate calculation), and plotted in Fig. 6.1. They are also listed in Table 6.3 and Table 6.4. We neglect interference of the resonances.

The reaction rate for temperatures typical of nova is clearly dominated by two resonances at 6263 keV($E_{c.m.}$= 130 keV) and 6544 keV ($E_{c.m.}$= 411 keV), respectively, the former at low temperatures and the latter at temperatures above 0.2 GK. For even lower temperatures below 0.03 GK, the rate is completely dominated by the 6160 keV ($E_{c.m.}$= 27 keV) resonance. The total rate is compared with the value from Hauser-Feschbach calculations [36] and is plotted in the bottom panel of Fig. 6.1.

For temperatures greater than 0.3 GK, the present rate agrees well with the Hauser-Feschbach rate, the difference is within a factor of 2. However at temperatures below 0.3 GK, including peak nova temperatures, our rate differs from the Hauser-Feschbach rate by a factor of up to 10. At temperatures even lower, the present rate differs from that calculated using Hauser-Feschbach formalism by orders of magnitude. This shows the statistical model is no longer valid at lower temperatures as the rate is completely dominated by the individual low-energy resonances.

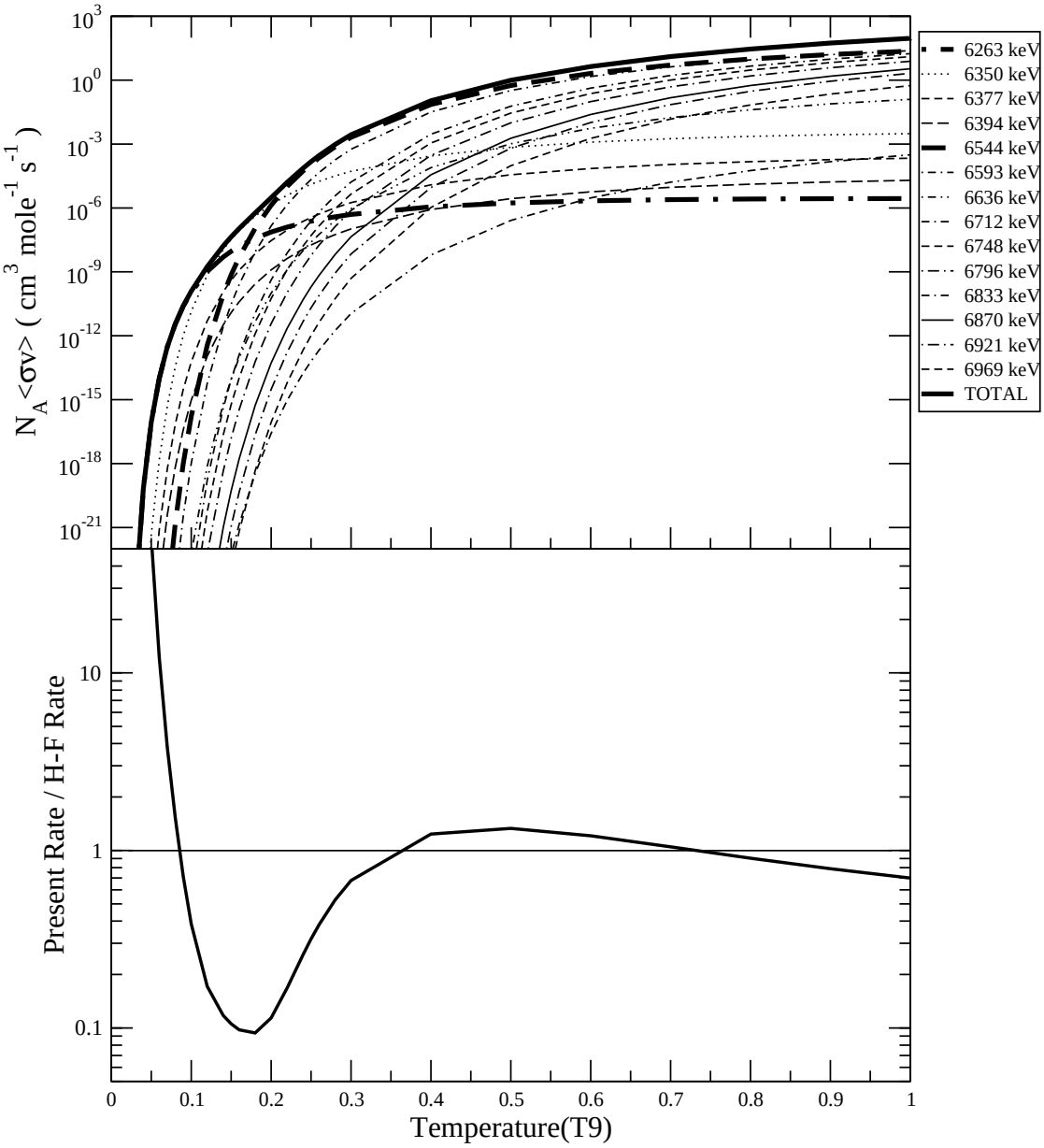

Figure 6.1: ^{30}P(p,γ)^{31}S reaction rate from present work(top panel). Contributions from individual resonances are also shown. The bottom panel shows the ratio of reaction rate from present work to that from Hauser-Feschbach calculation.

Table 6.3: Reaction rates vs. temperatures for contribution of each of the individual resonances. The first column is the temperature in units of GK. The last column is the total rate. Reaction rate is in units of (cm ^{3} mole^{-1} s^{-1})

T_9	6160(keV)	6263(keV)	6350(keV)	6377(keV)	6394(keV)	6544(keV)	6593(keV)
0.001	1.63E-158	0.00E+00	0.00E+00	0.00E+00	0.00E+00	0.00E+00	0.00E+00
0.002	2.02E-90	0.00E+00	0.00E+00	0.00E+00	0.00E+00	0.00E+00	0.00E+00
0.003	7.75E-68	3.02E-220	0.00E+00	0.00E+00	0.00E+00	0.00E+00	0.00E+00
0.004	1.34E-56	7.81E-166	5.74E-272	7.04E-307	0.00E+00	0.00E+00	0.00E+00
0.005	6.84E-50	3.21E-133	1.98E-217	1.46E-245	1.91E-263	0.00E+00	0.00E+00
0.006	1.93E-45	1.69E-111	4.31E-181	1.05E-204	9.10E-220	0.00E+00	0.00E+00
0.007	2.81E-42	5.34E-96	3.75E-155	1.54E-175	1.39E-188	5.63E-290	0.00E+00
0.008	6.46E-40	2.19E-84	1.04E-135	1.13E-153	3.30E-165	4.50E-253	1.12E-283
0.009	4.34E-38	2.31E-75	1.35E-120	1.12E-136	4.90E-147	2.22E-224	1.49E-251
0.01	1.24E-36	3.76E-68	1.64E-108	4.35E-123	1.66E-132	1.97E-201	7.30E-226
0.02	3.13E-30	7.65E-36	2.79E-54	4.47E-62	2.92E-67	2.59E-98	2.15E-110
0.03	3.28E-28	3.46E-25	2.57E-36	7.47E-42	1.26E-45	4.72E-64	5.10E-72
0.04	2.96E-27	6.49E-20	2.17E-27	8.51E-32	7.28E-35	5.60E-47	6.91E-53
0.05	1.02E-26	8.77E-17	4.57E-22	8.52E-26	1.93E-28	9.12E-37	1.93E-41
0.06	2.23E-26	1.02E-14	1.54E-18	8.12E-22	3.53E-24	5.57E-30	7.86E-34
0.07	3.76E-26	2.93E-13	4.90E-16	5.44E-19	3.76E-21	3.78E-25	2.07E-28
0.08	5.40E-26	3.55E-12	3.60E-14	6.98E-17	6.84E-19	1.55E-21	2.33E-24
0.09	7.02E-26	2.42E-11	9.96E-13	2.98E-15	3.83E-17	9.77E-19	3.25E-21
0.1	8.51E-26	1.10E-10	1.40E-11	5.91E-14	9.43E-16	1.67E-16	1.04E-18
0.12	1.10E-25	1.04E-09	7.06E-10	5.03E-12	1.11E-13	3.60E-13	5.81E-15
0.14	1.27E-25	4.97E-09	1.12E-08	1.16E-10	3.23E-12	8.35E-11	2.65E-12
0.15	1.33E-25	9.18E-09	3.36E-08	4.03E-10	1.23E-11	7.30E-10	3.04E-11
0.16	1.37E-25	1.56E-08	8.71E-08	1.19E-09	3.94E-11	4.84E-09	2.55E-10

Continued on Next Page...

Table6.3 – Continued

T_9	6160(keV)	6263(keV)	6350(keV)	6377(keV)	6394(keV)	6544(keV)	6593(keV)
0.18	1.43E-25	3.74E-08	4.19E-07	7.11E-09	2.70E-10	1.11E-07	8.71E-09
0.2	1.46E-25	7.37E-08	1.45E-06	2.93E-08	1.24E-09	1.34E-06	1.44E-07
0.22	1.46E-25	1.27E-07	3.95E-06	9.18E-08	4.24E-09	1.02E-05	1.42E-06
0.24	1.44E-25	1.97E-07	9.00E-06	2.35E-07	1.17E-08	5.44E-05	9.38E-06
0.25	1.43E-25	2.39E-07	1.29E-05	3.55E-07	1.82E-08	1.13E-04	2.15E-05
0.26	1.42E-25	2.84E-07	1.79E-05	5.17E-07	2.74E-08	2.23E-04	4.61E-05
0.28	1.38E-25	3.84E-07	3.20E-05	1.01E-06	5.63E-08	7.38E-04	1.79E-04
0.3	1.34E-25	4.96E-07	5.25E-05	1.78E-06	1.04E-07	2.07E-03	5.74E-04
0.4	1.14E-25	1.13E-06	2.78E-04	1.22E-05	8.43E-07	7.17E-02	3.19E-02
0.5	9.51E-26	1.72E-06	7.01E-04	3.61E-05	2.74E-06	5.57E-01	3.29E-01
0.6	8.04E-26	2.17E-06	1.23E-03	7.05E-05	5.71E-06	2.08E+00	1.48E+00
0.7	6.88E-26	2.46E-06	1.78E-03	1.10E-04	9.31E-06	5.13E+00	4.20E+00
0.8	5.96E-26	2.64E-06	2.29E-03	1.49E-04	1.31E-05	9.84E+00	8.91E+00
0.9	5.21E-26	2.73E-06	2.72E-03	1.85E-04	1.67E-05	1.60E+01	1.57E+01
1	4.61E-26	2.75E-06	3.08E-03	2.16E-04	1.99E-05	2.32E+01	2.42E+01
2	1.91E-26	2.07E-06	3.83E-03	3.15E-04	3.20E-05	8.91E+01	1.24E+02
3	1.10E-26	1.45E-06	3.17E-03	2.75E-04	2.88E-05	1.07E+02	1.64E+02
4	7.30E-27	1.07E-06	2.54E-03	2.26E-04	2.41E-05	1.04E+02	1.66E+02
5	5.31E-27	8.24E-07	2.06E-03	1.86E-04	2.01E-05	9.43E+01	1.55E+02
6	4.08E-27	6.59E-07	1.71E-03	1.56E-04	1.69E-05	8.41E+01	1.41E+02
7	3.26E-27	5.42E-07	1.44E-03	1.32E-04	1.44E-05	7.47E+01	1.27E+02
8	2.69E-27	4.56E-07	1.23E-03	1.14E-04	1.24E-05	6.66E+01	1.14E+02
9	2.26E-27	3.90E-07	1.07E-03	9.91E-05	1.09E-05	5.96E+01	1.03E+02
10	1.94E-27	3.39E-07	9.38E-04	8.73E-05	9.60E-06	5.37E+01	9.35E+01

Table 6.4: Same as Table 6.3, for other levels.

T_9	6636(keV)	6712(keV)	6748(keV)	6796(keV)	6833(keV)	6870(keV)	Total
0.001	0.00E+00	0.00E+00	0.00E+00	0.00E+00	0.00E+00	0.00E+00	1.63E-158
0.002	0.00E+00	0.00E+00	0.00E+00	0.00E+00	0.00E+00	0.00E+00	2.02E-90
0.003	0.00E+00	0.00E+00	0.00E+00	0.00E+00	0.00E+00	0.00E+00	7.75E-68
0.004	0.00E+00	0.00E+00	0.00E+00	0.00E+00	0.00E+00	0.00E+00	1.34E-56
0.005	0.00E+00	0.00E+00	0.00E+00	0.00E+00	0.00E+00	0.00E+00	6.84E-50
0.006	0.00E+00	0.00E+00	0.00E+00	0.00E+00	0.00E+00	0.00E+00	1.93E-45
0.007	0.00E+00	0.00E+00	0.00E+00	0.00E+00	0.00E+00	0.00E+00	2.81E-42
0.008	0.00E+00	0.00E+00	0.00E+00	0.00E+00	0.00E+00	0.00E+00	6.46E-40
0.009	8.15E-278	0.00E+00	0.00E+00	0.00E+00	0.00E+00	0.00E+00	4.34E-38
0.01	1.05E-249	2.21E-285	1.74E-303	0.00E+00	0.00E+00	0.00E+00	1.24E-36
0.02	2.38E-123	6.31E-140	5.87E-149	5.03E-161	1.18E-174	1.18E-179	3.13E-30
0.03	2.40E-81	1.49E-91	1.46E-97	1.35E-105	4.37E-116	5.20E-118	3.47E-25
0.04	2.13E-60	2.01E-67	6.41E-72	6.13E-78	7.40E-87	3.04E-87	6.49E-20
0.05	7.30E-48	5.59E-53	1.44E-56	2.24E-61	2.37E-69	8.12E-69	8.77E-17
0.06	1.58E-39	2.27E-43	2.36E-46	2.34E-50	1.05E-57	1.49E-56	1.02E-14
0.07	1.37E-33	1.60E-36	4.49E-39	1.68E-42	2.12E-49	8.24E-48	2.94E-13
0.08	3.78E-29	2.13E-31	1.26E-33	1.27E-36	3.49E-43	2.90E-41	3.59E-12
0.09	1.06E-25	2.01E-27	2.13E-29	4.67E-32	2.34E-38	3.50E-36	2.52E-11
0.1	5.93E-23	3.00E-24	5.06E-26	2.06E-28	1.67E-34	4.00E-32	1.24E-10
0.12	7.60E-19	1.67E-19	5.64E-21	5.80E-23	9.71E-29	4.73E-26	1.75E-09
0.14	6.31E-16	3.94E-16	2.19E-17	4.38E-19	1.23E-24	9.91E-22	1.64E-08
0.15	9.17E-15	8.72E-15	5.91E-16	1.54E-17	5.31E-23	5.25E-20	4.40E-08
0.16	9.49E-14	1.30E-13	1.05E-14	3.45E-16	1.43E-21	1.68E-18	1.09E-07
0.18	4.59E-12	1.16E-11	1.25E-12	6.05E-14	3.38E-19	5.35E-16	5.84E-07

Continued on Next Page...

Table6.4 – Continued

T_9	6636(keV)	6712(keV)	6748(keV)	6796(keV)	6833(keV)	6870(keV)	Total
0.2	1.00E-10	4.14E-10	5.63E-11	3.71E-12	2.64E-17	5.29E-14	3.04E-06
0.22	1.24E-09	7.61E-09	1.25E-09	1.06E-10	9.20E-16	2.24E-12	1.58E-05
0.24	9.92E-09	8.51E-08	1.64E-08	1.72E-09	1.75E-14	5.01E-11	7.34E-05
0.25	2.47E-08	2.45E-07	5.06E-08	5.83E-09	6.39E-14	1.96E-10	1.49E-04
0.26	5.72E-08	6.50E-07	1.43E-07	1.80E-08	2.11E-13	6.89E-10	2.88E-04
0.28	2.55E-07	3.69E-06	9.10E-07	1.33E-07	1.76E-12	6.46E-09	9.56E-04
0.3	9.22E-07	1.65E-05	4.49E-06	7.49E-07	1.10E-11	4.47E-08	2.72E-03
0.4	7.77E-05	2.89E-03	1.12E-03	2.96E-04	6.23E-09	3.61E-05	1.08E-01
0.5	1.03E-03	5.95E-02	2.83E-02	9.93E-03	2.60E-07	1.86E-03	9.88E-01
0.6	5.49E-03	4.25E-01	2.33E-01	9.82E-02	2.97E-06	2.45E-02	4.36E+00
0.7	1.75E-02	1.67E+00	1.01E+00	4.87E-01	1.63E-05	1.49E-01	1.28E+01
0.8	4.07E-02	4.54E+00	2.96E+00	1.57E+00	5.70E-05	5.62E-01	2.89E+01
0.9	7.67E-02	9.67E+00	6.68E+00	3.84E+00	1.48E-04	1.54E+00	5.49E+01
1	1.25E-01	1.74E+01	1.26E+01	7.71E+00	3.11E-04	3.41E+00	9.23E+01
2	8.21E-01	1.77E+02	1.58E+02	1.28E+02	6.40E-03	8.68E+01	9.40E+02
3	1.18E+00	2.96E+02	2.82E+02	2.51E+02	1.35E-02	1.97E+02	1.82E+03
4	1.25E+00	3.36E+02	3.33E+02	3.09E+02	1.73E-02	2.60E+02	2.31E+03
5	1.20E+00	3.37E+02	3.40E+02	3.25E+02	1.85E-02	2.86E+02	2.50E+03
6	1.11E+00	3.20E+02	3.28E+02	3.19E+02	1.85E-02	2.89E+02	2.52E+03
7	1.01E+00	2.98E+02	3.09E+02	3.04E+02	1.78E-02	2.81E+02	2.45E+03
8	9.17E-01	2.75E+02	2.87E+02	2.86E+02	1.69E-02	2.68E+02	2.34E+03
9	8.33E-01	2.53E+02	2.66E+02	2.67E+02	1.58E-02	2.53E+02	2.21E+03
10	7.59E-01	2.33E+02	2.45E+02	2.48E+02	1.48E-02	2.38E+02	2.08E+03

Uncertainty in the new ^{30}P(p,γ)^{31}S reaction rate is calculated based on an evaluation of the ^{31}S level structure information from present measurement and previous work. Due to the reduction of the uncertainties in the excitation energies, the uncertainty in the reaction rate is significantly narrowed down to within a factor of 2 at nova temperatures (see Fig. 6.2).

The present reaction rate is derived employing experimental information whenever available. Therefore it is obtained using a completely different technique as compared to that from theoretical Hauser-Feschbach calculations. We are able to significantly reduce the uncertainties of the excitation energies of the resonances that contribute to the ^{30}P(p,γ)^{31}S reaction rate based on a compilation of values from present measurement and previous measurements. We use the spectroscopic factors from Jenkins et al. [55] but we calculate the proton widths using a different technique. Thus the present rate and that from a previous work [55] and that from the Hauser-Feschbach calculations obtained using complementary techniques constitute a starting point for understanding the ^{30}P(p,γ)^{31}S reaction rate before a completely experiment based rate becomes available. This is only possible after a radioactive ^{30}P beam is available. Furthermore, the identification of resonances that dominate the ^{30}P(p,γ)^{31}S reaction rate would help future studies using radioactive ^{30}P beams with, for instance, which resonances to measure.

Expressions for the relevant nuclear reaction rates as analytic functions of the stellar temperature are crucial input for modeling complex astrophysical events such as novae. We have parameterized our new ^{30}P(p,γ)^{31}S reaction rate using the online Computational Infrastructure for Nuclear Astrophysics [57]. The total reaction rate was fitted over temperature range 0.03 GK $\leqslant$ T $\leqslant$ 10.0 GK. The residuals of the fit are less than 1% for most of the temperatures. A set of parameters of the REACLIB

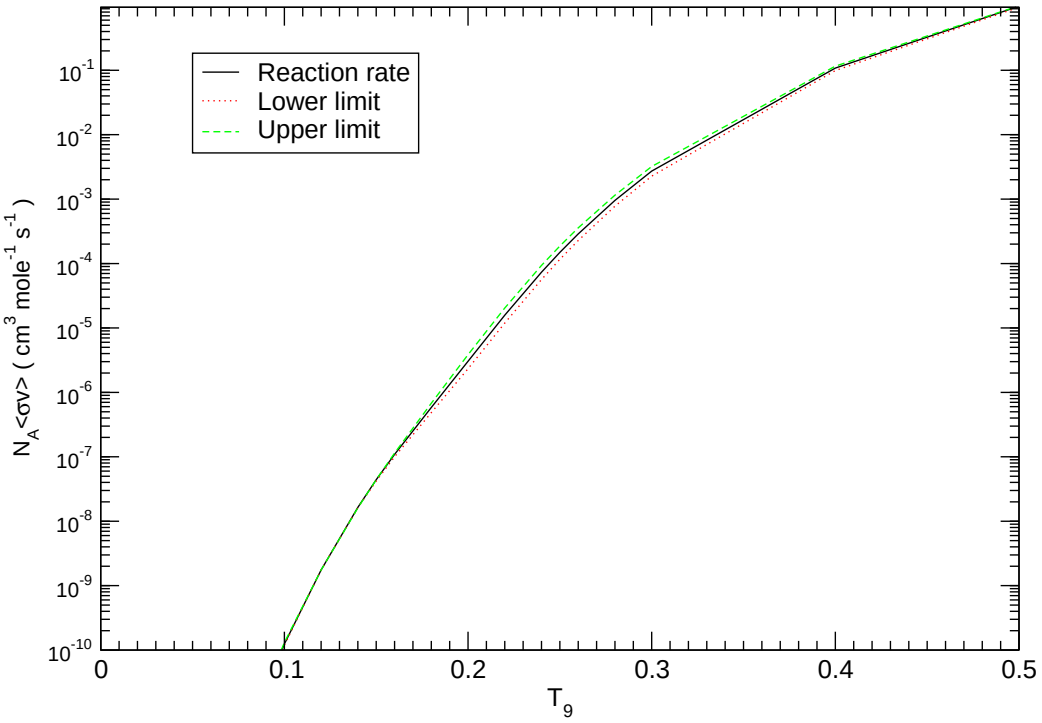

Figure 6.2: Uncertainty in the new ^{30}P(p,γ)^{31}S reaction rate at nova temperatures.

format [21] were obtained. The rate expression using these parameters is given in Table 6.5.

6.2 Implications on Nova Nucleosynthesis

6.2.1 Abundance Patterns

To investigate the influence of the new ^{30}P(p,γ)^{31}S reaction rate on nova nucleosynthesis, we have performed multi-zone network calculations in nova outbursts on 1.25 and 1.35 solar mass ONe white dwarfs and a 1.00 solar mass CO white dwarf (see Chapter 3 for details about the network calculations). New abundance patterns are obtained and are compared to those obtained using ^{30}P(p,γ)^{31}S reaction rate based on statistical Hauser-Feshbach calculations [36]. The results for 1.25 and 1.35 solar mass ONe white dwarf novae are shown in Fig. 6.3 and Fig. 6.4, and are also listed in Table 6.6 and Table 6.7. For the 1.00 solar mass CO white dwarf nova, the effect resulted from the new ^{30}P(p,γ)^{31}S rate is negligible as expected due to the lack of seed nuclei in the Si-Ca mass region.

The peak temperatures achieved in 1.25 and 1.35 solar mass ONe white dwarfs novae are $\sim$0.35 and $\sim$0.45 GK, respectively (see Fig. 3.4a on page 36 and Fig. 3.5a on page 37). At these peak temperatures the new ^{30}P(p,γ)^{31}S reaction rate agrees well with that from Hauser-Feshbach calculations. At lower temperatures around 0.2 GK, our new rate is $\sim$ 10 times lower than the Hauser-Feshbach rate. The results of our network calculations using the new ^{30}P(p,γ)^{31}S reaction rate shows that the overall effect of the new rate is same as that of a slight decrease of the Hauser-Feshbach rate, as can be seen in Fig. 6.3, 6.4 and Table 6.6, 6.7.

Table 6.5: Fit results and reaction rate expression for the ^{30}P(p,γ)^{31}S rate. The reaction rate $N_A\langle\sigma v\rangle$ is in units of (cm ^{3} mole^{-1} s^{-1}) and temperature T_9 in units of GK.

$$
\begin{aligned}
N_A\langle\sigma v\rangle &= exp(a1 + a2/T_9 + a3/T_9^{1/3} + a4 * T_9^{1/3} \\
&\quad + a5 * T_9 + a6 * T_9^{5/3} + a7 * ln(T_9)) \\
&\quad + exp(a8 + a9/T_9 + a10/T_9^{1/3} + a11 * T_9^{1/3} \\
&\quad + a12 * T_9 + a13 * T_9^{5/3} + a14 * ln(T_9))
\end{aligned}
$$

where

a1	=	6.50497E+00
a2	=	-1.32427E+01
a3	=	2.46306E+02
a4	=	-2.44639E+02
a5	=	1.00391E+01
a6	=	-4.51484E -01
a7	=	1.45797E+02
a8	=	-4.13623E+03
a9	=	5.43886E+00
a10	=	-1.12155E+03
a11	=	6.32703E+03
a12	=	-1.29338E+03
a13	=	1.64339E+02
a14	=	-1.59144E+03

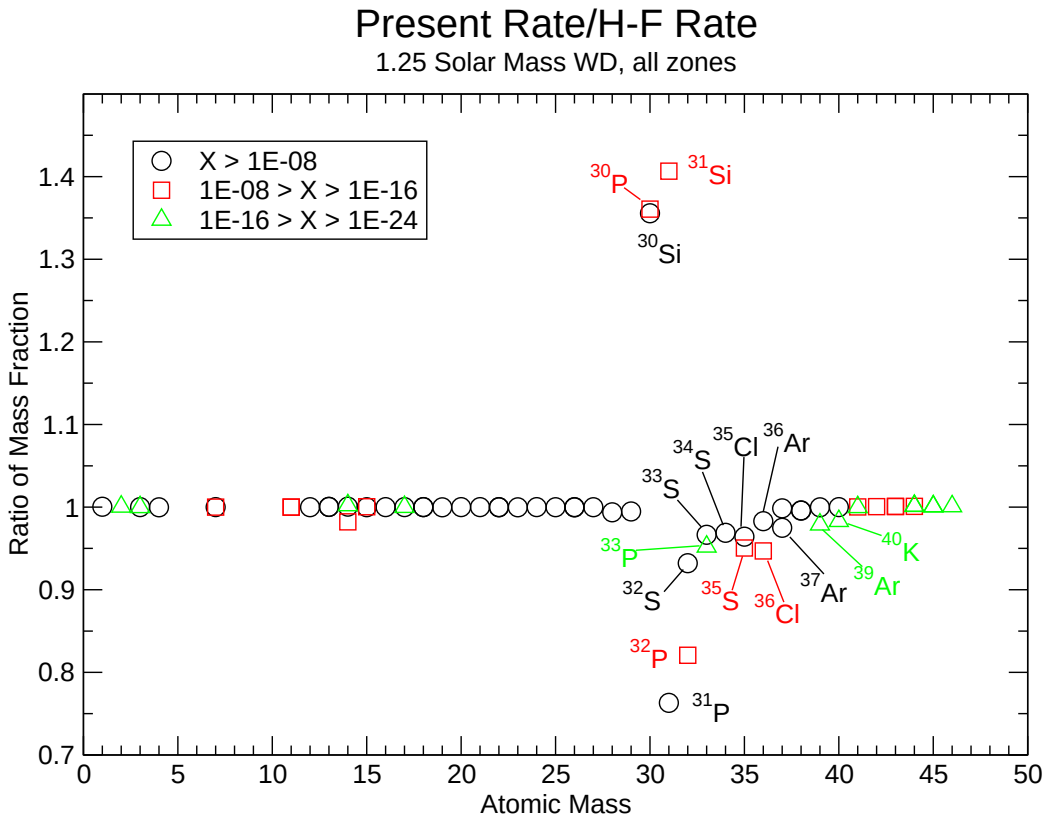

Figure 6.3: Ratio of abundances (mass fractions) obtained using new ^{30}P(p,γ)^{31}S reaction rate to those obtained using Hauser-Feshbach rate, for a 1.25 $M_{\odot}$ ONe White Dwarf nova.

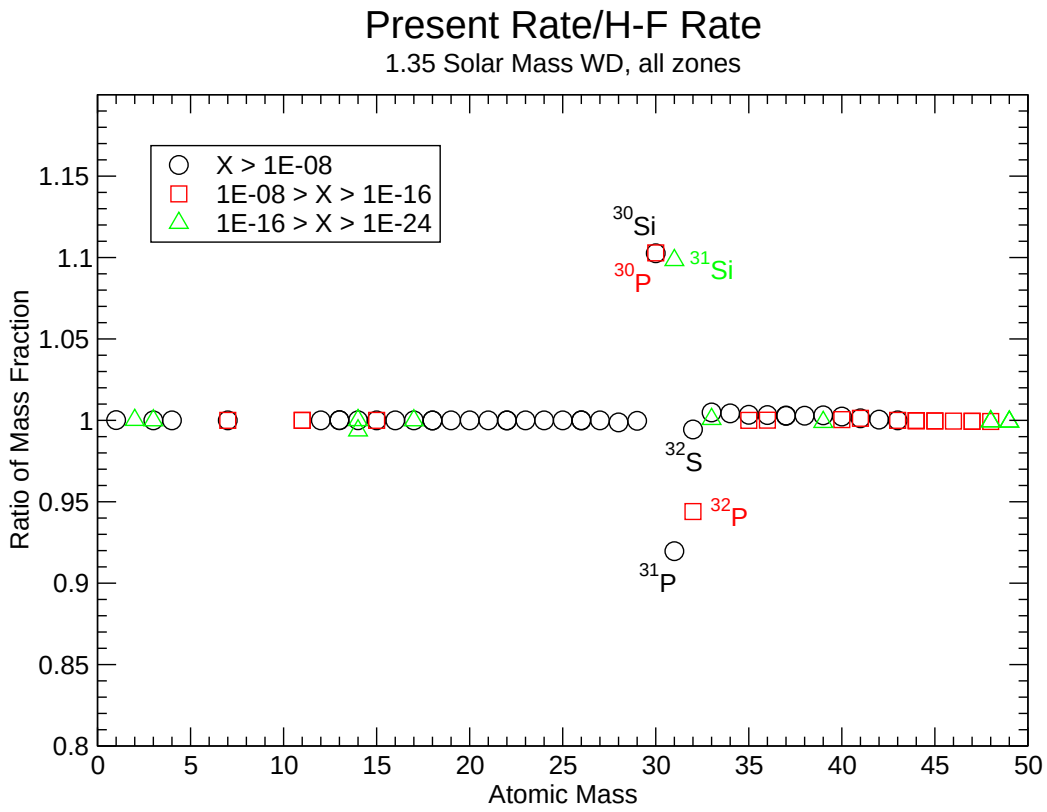

Figure 6.4: Same as Fig. 6.3, for a 1.35 $M_{\odot}$ ONe White Dwarf nova.

Table 6.6: Abundances (mass fractions) for some of the elements in the ejecta of a 1.25 $M_\odot$ ONe White Dwarf nova. Abundances using the $^{30}P(p,\gamma)^{31}S$ reaction rate obtained in the present work are listed in the column labeled by X_1, and those using the $^{30}P(p,\gamma)^{31}S$ reaction rate obtained from Hauser-Feshbach calculations listed in column X_2.

Isotope	X_1	X_2	ratio(X_1/X_2)
C12	1.72539E-02	1.72561E-02	9.999E-01
C13	6.74682E-03	6.74525E-03	1.000E+00
N14	5.48392E-03	5.48107E-03	1.001E+00
N15	1.77623E-02	1.77637E-02	9.999E-01
Al26	3.27655E-03	3.27759E-03	9.997E-01
Al27	2.29015E-02	2.29051E-02	9.998E-01
Si28	3.10740E-02	3.12703E-02	9.937E-01
Si29	1.64875E-03	1.65748E-03	9.947E-01
Si30	1.29206E-02	9.53089E-03	1.356E+00
Si31	5.93480E-15	4.21920E-15	1.407E+00
P30	1.21041E-09	8.89517E-10	1.361E+00
P31	8.20576E-03	1.07531E-02	7.631E-01
P32	1.09340E-14	1.33237E-14	8.206E-01
P33	8.04541E-17	8.44938E-17	9.522E-01
S32	9.91507E-03	1.06377E-02	9.321E-01
S33	1.96158E-04	2.02953E-04	9.665E-01
S34	8.84429E-05	9.12816E-05	9.689E-01
S35	5.25356E-16	5.52696E-16	9.505E-01
Cl35	6.79848E-05	7.05033E-05	9.643E-01
Cl36	8.24366E-16	8.70484E-16	9.470E-01
Cl37	2.36388E-07	2.36750E-07	9.985E-01
Ar36	1.79656E-05	1.82776E-05	9.829E-01
Ar37	1.69683E-05	1.74032E-05	9.750E-01
Ar38	5.39866E-06	5.42169E-06	9.958E-01
Ar39	2.16548E-18	2.21207E-18	9.789E-01
K38	2.24697E-08	2.25600E-08	9.960E-01
K39	1.81585E-06	1.81622E-06	9.998E-01
K40	1.17222E-17	1.19225E-17	9.832E-01
K41	6.43606E-19	6.43609E-19	1.000E+00
Ca40	1.68105E-05	1.68105E-05	1.000E+00

Table 6.7: Same as Table 6.6, for a 1.35 $M_{\odot}$ ONe White Dwarf nova.

Isotope	X_1	X_2	ratio(X_1/X_2)
C12	6.28011E-03	6.27999E-03	1.000E+00
C13	1.41445E-03	1.41430E-03	1.000E+00
N14	3.34294E-03	3.34277E-03	1.000E+00
N15	7.38068E-02	7.38065E-02	1.000E+00
Al26	1.05000E-03	1.04996E-03	1.000E+00
Al27	3.59561E-02	3.59568E-02	1.000E+00
Si28	2.36915E-02	2.37218E-02	9.987E-01
Si29	4.86877E-03	4.87010E-03	9.997E-01
Si30	2.02069E-02	1.83263E-02	1.103E+00
Si31	6.58201E-17	5.99238E-17	1.098E+00
P30	1.87476E-09	1.69993E-09	1.103E+00
P31	2.15780E-02	2.34636E-02	9.196E-01
P32	1.22804E-15	1.30086E-15	9.440E-01
P33	2.78569E-17	2.78358E-17	1.001E+00
S32	9.18472E-03	9.23662E-03	9.944E-01
S33	1.41490E-03	1.40808E-03	1.005E+00
S34	1.38765E-03	1.38171E-03	1.004E+00
S35	7.94908E-16	7.94930E-16	1.000E+00
Cl35	3.63599E-03	3.62349E-03	1.003E+00
Cl36	3.10750E-15	3.10712E-15	1.000E+00
Cl37	1.57418E-06	1.56984E-06	1.003E+00
Ar36	4.92645E-04	4.91041E-04	1.003E+00
Ar37	1.77516E-03	1.76989E-03	1.003E+00
Ar38	5.38965E-04	5.37442E-04	1.003E+00
Ar39	4.30797E-18	4.31248E-18	9.990E-01
K39	1.94501E-04	1.93900E-04	1.003E+00
K40	2.43284E-16	2.43174E-16	1.000E+00
K41	1.57754E-16	1.57556E-16	1.001E+00
Ca40	5.78814E-05	5.77445E-05	1.002E+00

For the 1.35 solar mass white dwarf nova case, the effect of the new rate is much smaller than that in the 1.25 solar mass case, as a consequence of compensation effect of the higher rate around peak temperatures and lower rate at lower temperatures (see Fig. 6.1 on page 92).

We have determined how the uncertainty in the new ^{30}P(p,γ)^{31}S reaction rate would translate into the uncertainty in the abundance predictions. Results are shown in Fig. 6.5 and Fig. 6.6. The effect of the ^{30}P(p,γ)^{31}S reaction rate uncertainty on nova nucleosynthesis is consistent with network calculation results discussed in Chapter 3.

6.2.2 Production of Heavier Elements

As stated previously, spectroscopic abundance determinations have shown evidence for some overproduction of nuclei in the Si-Ca mass region in a number of classical novae [9, 32, 58]. Our results confirmed these abundance determinations (Table 6.8) with overproduction factors up to 3000.

6.2.3 Presolar Grains

Amari et al. [34] reported the discovery of five SiC grains and one graphite grain isolated from the Murchison carbonaceous meteorite whose major-element isotopic compositions indicate an origin in nova explosions. The grains are characterized by low ^{12}C/^{13}C and ^{14}N/^{15}N, high ^{26}Al/^{27}Al ratio, close-to-solar ^{29}Si/^{28}Si and large excesses in ^{30}Si/^{28}Si. Our calculations listed in Table 6.9 agree with these observations.

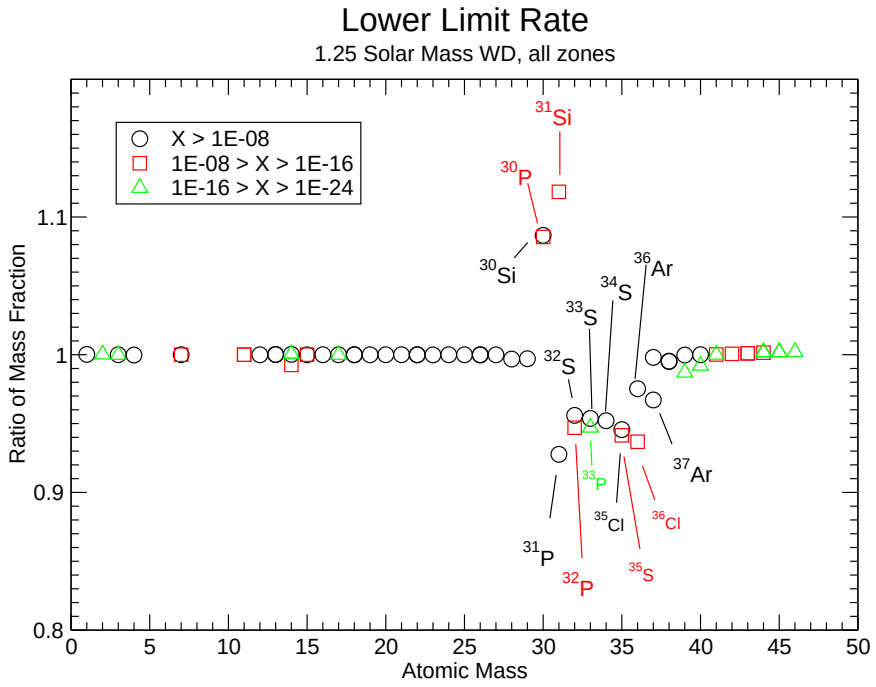

(a)

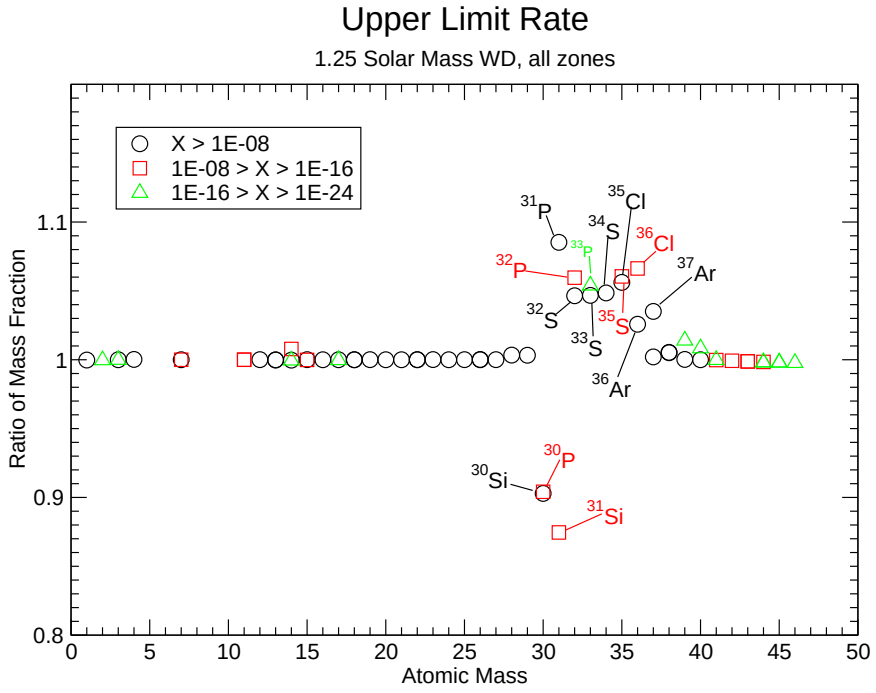

(b)

Figure 6.5: Effect of the rate uncertainty on abundance predictions for a 1.25 $M_{\odot}$ WD nova. The upper figure shows the ratio of abundances (mass fraction) obtained using the lower limit of the ^{30}P(p,γ)^{31}S rate to that using the central ^{30}P(p,γ)^{31}S rate. The lower figure is for the upper limit of the reaction rate case.

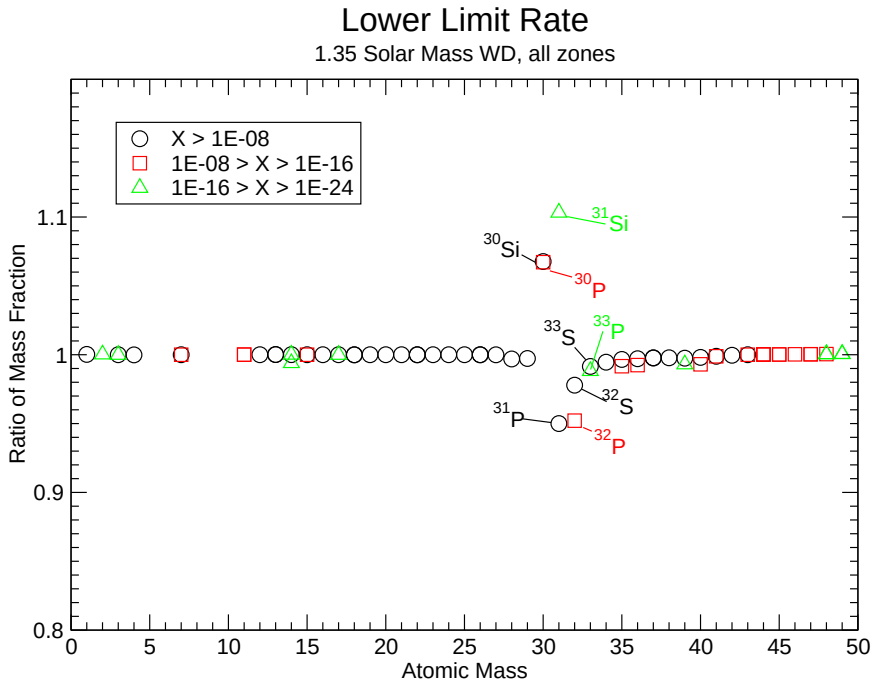

(a)

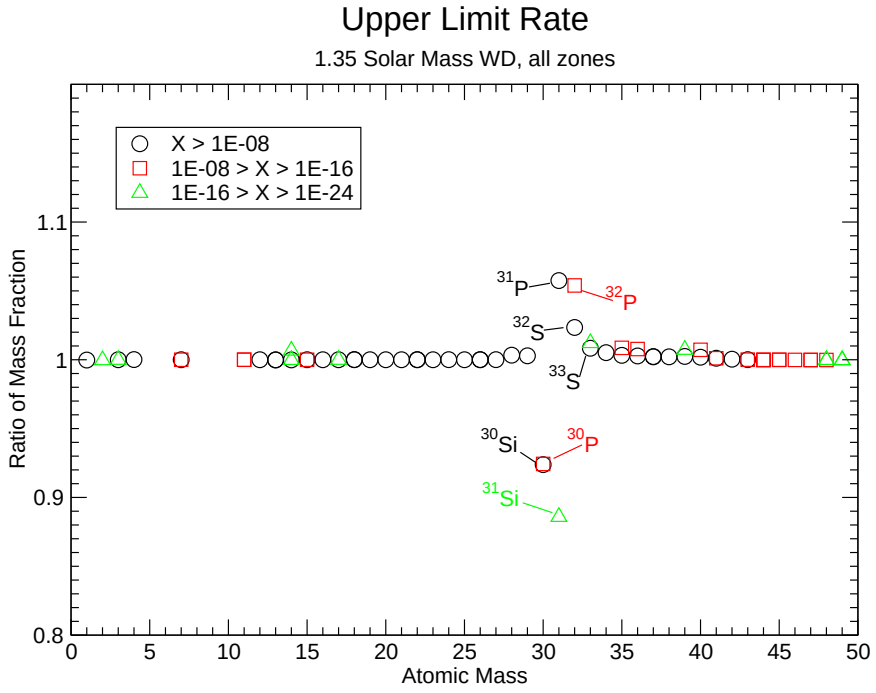

(b)

Figure 6.6: Effect of the rate uncertainty on abundance predictions for a 1.35 $M_{\odot}$ WD nova. The upper figure shows the ratio of abundances (mass fraction) obtained using the lower limit of the ^{30}P(p,γ)^{31}S rate to that using the central ^{30}P(p,γ)^{31}S rate. The lower figure is for the upper limit of the reaction rate case.

Table 6.8: Enhancement of heavier elements in Si-Ca mass region. The second column lists the abundances (mass fraction) of isotopes for a 1.25 $M_\odot$ white dwarf nova. The third column lists the ratios of abundances from the present work to solar values. The third and fourth columns are for a 1.35 $M_\odot$ white dwarf nova.

isotope	solar	1.25 $M_\odot$	ratio	1.35 $M_\odot$	ratio
Si28	6.530E-04	3.11E-02	4.8E+01	2.37E-02	3.6E+01
Si29	3.448E-05	1.65E-03	4.8E+01	4.87E-03	1.4E+02
Si30	2.345E-05	1.29E-02	5.5E+02	2.02E-02	8.6E+02
P31	8.155E-06	8.21E-03	1.0E+03	2.16E-02	2.6E+03
S32	3.958E-04	9.92E-03	2.5E+01	9.18E-03	2.3E+01
S33	3.264E-06	1.96E-04	6.0E+01	1.41E-03	4.3E+02
S34	1.866E-05	8.84E-05	4.7E+00	1.39E-03	7.4E+01
Cl35	3.506E-06	6.80E-05	1.9E+01	3.64E-03	1.0E+03
Cl37	1.198E-06	2.36E-07	2.0E-01	1.57E-06	1.3E+00
Ar36	7.740E-05	1.80E-05	2.3E-01	4.93E-04	6.4E+00
Ar38	1.538E-05	5.40E-06	3.5E-01	5.39E-04	3.5E+01
K39	3.463E-06	1.82E-06	5.2E-01	1.95E-04	5.6E+01
K40	5.221E-09	1.17E-17	2.2E-09	2.43E-16	4.7E-08
K41	2.686E-07	6.44E-19	2.4E-12	1.58E-16	5.9E-10
Ca40	5.990E-05	1.68E-05	2.8E-01	5.79E-05	9.7E-01

Table 6.9: Abundance (by number) ratios for candidates of presolar grains with nova origin.

Grain	$^{12}C/^{13}C$	$^{14}N/^{15}N$	$\delta^{29}Si/^{28}Si$ [d]	$\delta^{30}Si/^{28}Si$ [d]	$^{26}Al/^{27}Al$
AF15bB-429-3 [a]	9.4 ± 0.2	28 ± 30	1118 ± 44		
AF15bC-126-3 [a]	6.8 ± 0.2	5.22 ± 0.11	-105 ± 17	237 ± 20	
KJGM4C-100-3 [a]	5.1 ± 0.1	19.7 ± 0.3	55 ± 5	119 ± 6	0.0114
KJGM4C-311-6 [a]	8.4 ± 0.1	13.7 ± 0.1	-4 ± 5	149 ± 6	>0.08
KJC11 [a]	4.0 ± 0.2	6.7 ± 0.3			
KFC1a-551 [a]	8.5 ± 0.1	273 ± 8	84 ± 54	761 ± 72	
Solar Abundance [b]	89.9	270			∼ 0
1.25 $M_\odot$ ONe Nova calculations [c]	2.8	0.33	12	10595	0.15
1.35 $M_\odot$ ONe Nova calculations [c]	4.8	0.05	2919	22783	0.03
Other ONe nova calculations [a]	0.3 ∼ 3	0.1 ∼ 10	-800 ∼ 1800	-800 ∼ 15,000	0.07 ∼ 0.7

[a] S. Amari et al, ApJ., 551, 1065 (2001).

[b] E. Anders & N. Grevesse, Geochim. Cosmochim. Acta, 53,197 (1989).

[c] From this study.

[d] $\delta Si^{29,30}/^{28}Si \equiv [(Si^{29,30}/^{28}Si)/(Si^{29,30}/^{28}Si)_{solar} - 1]\times 1000$.

6.3 Conclusions

The ^{30}P(p,γ)^{31}S reaction rate is crucial for understanding the synthesis of heavier nuclear species, from Si to Ca, in nova outbursts on ONe White Dwarfs. The previous adopted rate, based on statistical model calculations [36], has a large uncertainty and could be as much as a factor of 100 too high or too low [26]. Accurate calculation of the ^{30}P(p,γ)^{31}S rate requires knowledge of the spectroscopic information on ^{31}S levels above the proton threshold. We have measured differential cross sections for the ^{32}S(p,d)^{31}S reaction and determined excitation energies for states in ^{31}S. A total of 26 states in ^{31}S were observed. Spins and parities were determined or constrained for 15 of the strongly populated levels through a distorted wave Born approximation (DWBA) analysis of the angular distributions. A new ^{30}P(p,γ)^{31}S reaction rate was calculated. The states at 6267 and 6546 keV are found to dominate the ^{30}P(p,γ)^{31}S reaction rate below and above 0.2 GK, respectively. Our results indicate that the ^{30}P(p,γ)^{31}S rate is reduced by up to a factor of 10 at nova temperatures compared to the previous value from statistical calculations. Production of elements in the Si-Ca mass region is found to be altered by as much as 40% in our network calculations using the new rate. Important isotopic ratios, for instance, the close-to-solar ^{29}Si/^{28}Si ratio and large excess in ^{30}Si/^{28}Si, the most important features pointing to a nova origin of such grains, are obtained, in agreement with observations [34].

Although we have considerably improved our understanding of the ^{31}S level scheme and the ^{30}P(p,γ)^{31}S reaction rate, there are still significant uncertainties affecting an accurate determination of the ^{30}P(p,γ)^{31}S rate, as some parameters used in the present work have come from theoretical determinations, estimations or information from the mirror ^{31}P levels. These uncertainties could only be resolved with a direct measurement of the ^{30}P(p,γ)^{31}S reaction. Therefore a ^{30}P radioactive beam is very

desirable. This would be a challenging measurement due to difficulties in producing ^{30}P radioactive beam with sufficient intensity for direct proton capture reaction, but may be possible in the not-too-distant future.

Bibliography

Bibliography

[1] A. S. Eddington, Rept. Brit. Assoc. Adv. Sci. (Cardiff) p.34 (1920).

[2] C. F. von Weizsäcker, PHys. Z. 38, 176 (1937).

[3] C. F. von Weizsäcker, PHys. Z. 39, 633 (1938).

[4] H. A. Bethe and C. L. Critchfield, Phys. Rev. 54, 248 and 862 (1938).

[5] H. A. Bethe, Phys. Rev. 55, 103 and 434 (1939).

[6] E. M. Burbidge et al., Rev. Mod. Phys., 29, 547 (1957).

[7] A. E. Champagne M. Wiescher, Annu. Rev. Nucl. Part. Sci, 42, 39 (1992).

[8] J. W. Truran and M. Livio, Astrophys. J. **308**, 721 (1986).

[9] C. Morisset and D. Pequignot, Astronomy and Astrophys., 312, 135 (1996).

[10] S. Starrfield et al., MNRAS, 296, 502 (1998).

[11] J. José et al., ApJ, 520, 347, (1999).

[12] http://integral.esac.esa.int/integral.html.

[13] http://glast.gsfc.nasa.gov/.

[14] M. D. Leising and D. D. Clayton, Astrophys. J. **323**, 159 (1987).

[15] A. Coc *et al.*, Phys. Rev. C **61**, 015801 (2000).

[16] http://www.onlineastronomy.com

[17] C. E. Rolfs and W. S. Rodney, Cauldrons in the Cosmos (The University of Chicago Press, 1988).

[18] J.M. Blatt and V.F. Weiskopf, Theoretical Nuclear Physics, John Wiley and Sons, 1962.

[19] D. Arnett, Supernovae and Nucleosynthesis, Princeton University Press, Princeton N.J.(1996).

[20] W.R. Hix and F.K. Thielemann, Journal of Computational and Applied Mathematics, 109, 321-351, (1999).

[21] http://ie.lbl.gov/astro/astrorate.html

[22] M. Politano et al., Astrophys. J. **448**, 807 (1995).

[23] E. Anders and N. Grevesse, Geochim. Cosmochim. Acta, **53**, 197 (1989).

[24] S. Starrfield, private communication.

[25] C. Iliadis et al., Astrophys. J. Suppl. Ser., **134**, 151 (2001).

[26] C. Iliadis et al., Astrophys. J. Suppl. Ser., **142**, 105 (2002).

[27] Wanajo, S., Hashimoto, M., and Nomoto, K., Astrophys. J., **523**, 409 (1999).

[28] J. Jose et al., Astrophys. J., **560**, 897 (2001).

[29] D. W. Bardayan, PhD thesis, Yale University, (1999)

[30] http://www.phy.ornl.gov/hribf

[31] J. José, M. Hernanz, Astrophys. J. **494**, 680 (1998).

[32] J. Andrea, H. Drechsel and S. Starrfield, Astron. Astrophys. **291**, 869 (1994).

[33] K. M. Vanlandingham, S. Starrfield, S. N. Shore, MNRAS **290**, 87 (1997).

[34] S. Amari *et al.*, Astrophys. J. **551**, 1065 (2001).

[35] Z. Ma *et al.*, American Astronomical Society Meeting 202, Abstract #30.02, (2003).

[36] T. Rauscher, F.-K. Thielemann, At. Data Nucl. Data Tables, **75**, 1 (2000).

[37] P. M. Endt, Nucl. Phys. **A633**, 1 (1998), and references therein.

[38] D. W. Bardayan *et al.*, Phys. Rev. C **65**, 032801(R) (2002).

[39] D. W. Bardayan *et al.*, Phys. Rev. C **62**, 055804 (2000).

[40] P. R. Bevington, Data Reduction and Error Analysis for the physical Sciences (McGraw-Hill, New York, 1969).

[41] D. K. Olsen *et al.*, Nucl. Instrum. Methods Phys. Res. **A254**, 1 (1987).

[42] F. Ajzenberg-Selove and J. L. Wiza, Phys. Rev. **143**, 853 (1966).

[43] T. S. Bhatia and W. W. Daehnick and G. J. Wagner, Phys. Rev. C **5**, 111 (1972).

[44] J. M. Davidson *et al.*, Nucl. Phys. **A240**, 253 (1975).

[45] C. E. Moss, Nucl. Phys. **A145**, 423 (1970).

[46] J. Vernotte *et al.*, Nucl. Phys. **A655**, 415 (1999).

[47] D. G. Jenkins *et al.*, Phys. Rev. C **72**, 031303(R) (2005).

[48] H. Nann and B. H. Wildenthal, Phys. Rev. C **19**, 2146 (1979).

[49] J. Aysto *et al.*, Phys. Rev. C **32**, 1700 (1985).

[50] R. L. Kozub, Phys. Rev. **172**, 1078 (1968).

[51] J. Källne, B. Fagerström, Physica Scripta, **11**, 79 (1975).

[52] Kankainen *et al.*, Eur. Phys. J. A **27**, 67 (2006).

[53] P. D. Kunz, http://spot.colorado.edu/kunz/

[54] C.Iliadis, Nucl. Phys. **A618**, 166 (1997).

[55] D. G. Jenkins *et al.*, Phys. Rev. C **73**, 065802 (2006).

[56] J. Vernotte *et al.*, Phys. Rev. C **41**, 1956 (1990).

[57] M. S. Smith *et al.*, http://www.nucastrodata.org/index.html

[58] M. Snijders et al., MNRAS, 228, 329 (1987).

Vita

Zhanwen Ma received his Bachelor of Science degree in China. After Graduation he worked as a research assistant in China Institute of Atomic Energy, China, and Oak Ridge National Laboratory, USA. He received his Doctor of Philosophy degree majoring in Physics in 2006 from the University of Tennessee, Knoxville. He has been conducting research in the field of experimental Nuclear Astrophysics.